Institute of Experimental and Clinical Pharmacology,

Toxicology and Pharmacology of Natural Products

Ulm University, Medical Center

Head: Prof. Dr. Holger Barth

Clostridium botulinum C3 Toxin as Inhibitor of Breast Cancer-Induced Osteolysis and Cell Type-Selective Transporter for Targeted Gene Editing in Monocytic Cells

---

DISSERTATION

submitted in partial fulfillment of the requirements for the degree

“Doctor rerum naturalium” (Dr. rer. nat.)

of the International Graduate School in Molecular Medicine Ulm

submitted by

Nicole Stadler

Born in Aalen, Germany

Ulm, 2026

Current dean of the Medical Faculty	Prof. Dr. Thomas Wirth
Current chairman of the Graduate School	Prof. Dr. Bernd Knöll
Thesis advisory committee	First supervisor: Prof. Dr. Holger Barth Institute of Experimental and Clinical Pharmacology, Toxicology and Pharmacology of Natural Products Ulm University, Medical Center Second supervisor: Prof. Dr. Manfred Frick Institute of General Physiology, Ulm University Third supervisor: Prof. Dr. Tanja Weil Max-Planck Institute for Polymer Research, Mainz
Day doctorate awarded	19.05.2026

Results gained in my thesis have previously been published in the following publication:

Stadler, N., Gao, B., Silva, M. J., Borho, J., Haunschild, E., Koynov, K., Haffner-Luntzer, M., Ignatius, A., Weidinger, G., Kuan, S. L., Weil, T. and Barth, H. (2025). Multifunctional Peptide-Based Biohybrid for Targeted Reduction of Metastatic Breast Carcinoma-Associated Osteolysis. *Journal of Functional Biomaterials*, 16(11), 399. DOI: https://doi.org/10.3390/jfb16110399.

Further publications with my contribution that are not directly associated with this thesis:

Hirschenberger, M., **Stadler, N.**, Fellermann, M., Sparrer, K. M., Kirchhoff, F., Barth, H., and Papatheodorou, P. (2021). CRISPA: a non-viral, transient Cas9 delivery system based on reengineered anthrax toxin. *Frontiers in Pharmacology*, *12*, 770283. DOI: 10.3389/fphar.2021.770283

Heber, S., Borho, J., **Stadler, N.**, Wondany, F., König, I., Michaelis, J., Papatheodorou, P., Barth, H. and Fellermann, M. (2023). The Clostridium botulinum C2 toxin Subunit C2IIa delivers enzymes with positively charged N-termini into the cytosol of target cells. *Toxins*, *15*(6), 390. DOI: 10.3390/toxins15060390

Wolfschmitt, E. M., Vogt, J. A., Hogg, M., Wachter, U., **Stadler, N.**, Kapapa, T., Datzmann, T., Messerer, D. A. C., Hoffmann, A., Gröger, M., Münz, F., Mathieu, R., Mayer, S., Merz, T., Asfar, P., Calzia, E., Radermacher, P. and Zink, F. (2024). 13C-Metabolic flux analysis detected a hyperoxemia-induced reduction of tricarboxylic acid cycle metabolism in granulocytes during two models of porcine acute subdural hematoma and hemorrhagic shock. *Frontiers in Immunology*, *14*, 1319986. DOI: https://doi.org/10.3389/fimmu.2023.1319986

Xu, L., Silva, M. J., Coelho, J. A., Borho, J., **Stadler, N.**, Barth, H., Kuan, S. L. and Weil, T. (2025). Chemoselective dual functionalization of proteins via 1, 6-addition of thiols to trifunctional N-alkylpyridinium. *Nature Communications*, *16*(1), 5278. DOI: 10.1038/s41467-025-60237-y

All listed articles were published in open-access journals with CC BY 4.0 license: https://creativecommons.org/licenses/by/4.0/

1 Table of Contents

1 Table of Contents III
2 List of Figures VI
3 List of Tables VII
4 List of Abbreviations VIII
1 Introduction 1
1.1 Bacterial Toxins 1
1.2 Bacterial ADP-Ribosylating C3 Toxins 2
1.3 C3-like Toxins as Pharmacological Tools 5
1.3.1 C3bot1 Against Breast Cancer Metastasis-Related Osteolysis in the Bone 8
1.3.2 $C3_{E174Q}$: Cell Type-Selective Delivery System for Targeted Gene Modulation . 18
1.4 Aim of the Thesis 27
2 Material and Methods 28
2.1 Material 28
2.1.1 Chemicals 28
2.1.2 Consumables and Kits 31
2.1.3 Devices 32
2.1.4 Buffers and Solutions 34
2.1.5 Proteins, Enzymes, Toxins and Antibodies 36
2.1.6 Plasmids, Primer and Enzymes for PCR 38
2.1.7 DNA Oligos for sgRNA Synthesis 40
2.1.8 Eukaryotic and Procaryotic Cell Lines and Corresponding Culture Media 40
2.1.9 Software and Online Tools 42
2.2 Methods 43
2.2.1 Cell Culture 43
2.2.2 Phase-Contrast Microscopy 44
2.2.3 SDS-PAGE and Western Blot 44
2.2.4 Cloning of $C3bot1_{(E174Q)}$_$Cas9^{NLS-His}$ 45
2.2.5 Expression of Recombinant Proteins in *E. coli* BL21 48
2.2.6 Purification of Recombinant $C3bot1_{(E174Q)}$_$Cas9^{NLS-His}$ 48
2.2.7 Purification of Recombinant $^{GST-Cys}$C3bot1 49
2.2.8 Single Guide RNA Synthesis 49
2.2.9 *In vitro* Cleavage Assay with $C3bot1_{(E174Q)}$_$Cas9^{NLS-His}$ 50
2.2.10 Isolation of Cytosolic and Nuclear Cellular Fractions 52

2.2.11 Fluorescence Labelling of C3bot1$_{(E174Q)}$_Cas9$^{NLS-His}$ 53
2.2.12 Assembly of the Nanocarrier $(JM173)_3$-^{BDP}Avi-C3 53
2.2.13 Determination of CXCR4 Expression Levels in Different Cell Lines 54
2.2.14 Binding- and Competition Assay 55
2.2.15 Fluorescence Microscopy 55
2.2.16 Sequential ADP-Ribosylation Assay 55
2.2.17 Cell Proliferation Assay – Colorimetric Readout 56
2.2.18 Cell Proliferation Assay – Live Cell Imaging 56
2.2.19 Effect of $(JM173)_3$-Avi-C3 on Osteoclast Formation and Resorption Activity .. 57
2.2.20 Effect of $(JM173)_3$-^{BDP}Avi-C3-treatment on Osteoblast Differentiation 57
3 Results 59
3.1 *Clostridium botulinum* C3 toxin: A Rho-Inhibitor for Down-Modulation of Breast Cancer Cell Proliferation 59
3.1.1 Assembly and Characterization of $(JM173)_3$-Avi-C3 59
3.1.2 $(JM173)_3$-Avi-C3 Selectively Binds to CXCR4 Expressing Cell Lines 64
3.1.3 JM173 Enhances the Uptake of C3 Toxin into CXCR4 Expressing Cell Lines 67
3.1.4 $(JM173)_3$-Avi-C3 Inhibits Osteoclast Differentiation and Resorption Activity . 71
3.1.5 C3 toxin Promotes Osteoblastogenesis 73
3.2 *Clostridium botulinum* C3 Toxin as Transport System for Cell Type-Selective Delivery of Cas9 74
3.2.1 Cloning and Expression of C3_Cas9 and $C3_{E174Q}$_Cas9 74
3.2.2 C3 Does Not Influence Cas9 Functionality in the Fusion Protein $C3_{E174Q}$_Cas9 75
3.2.3 Cas9 Does Not Influence C3 Functionality in the Fusion Protein $C3_{E174Q}$_Cas9 77
3.2.4 $C3_{E174Q}$_Cas9 Reaches the Nucleus of Monocytic Cells 80
4 Discussion 82
4.1 The Potential of *Clostridium botulinum* C3 Toxin as a Biologic in Cancer Treatment 82
4.1.1 Specific Binding of $(JM173)_3$-Avi-C3 to CXCR4 Expressing Cell Lines 83
4.1.2 Retargeting C3 Toxin into Metastatic Breast Cancer Cells by $(JM173)_3$-Avi-C3 84
4.1.3 $(JM173)_3$-Avi-C3 Influences Osteoclastogenesis, Osteoclast Resorption Activity and Osteoblastogenesis 86
4.1.4 Conclusion and Outlook 87
4.2 $C3_{E174Q}$ as Cell Type-Selective Transport System for Targeted Gene Modulation 88
4.2.1 The Genetic Fusion of Cas9 and $C3_{E174Q}$ Does Not Disturb the Individual Protein Functionalities 90
4.2.2 Optimization of $C3_{E174Q}$_Cas9 Formulation 92

4.2.3 $C3_{E174Q}$_Cas9 Delivers Cas9 into the Nucleus of Monocyte-Derived Cells 93
4.2.4 Conclusion and Outlook 94
5 Summary 96
6 List of References 98
7 Appendix 124
7.1 Sequence of $C3_{E174Q}$_$Cas9^{NLS-His}$ 124
7.2 Labelling of Proteins with $DyLight^{488}$ NHS Ester 124
7.3 Gene Fragments Amplified for Cleavage Assays 125
7.4 Endotoxin Measurement in C3_Cas9 and $C3_{E174Q}$_Cas9 126
8 Acknowledgements 127
9 Statutory Declaration 128

2 List of Figures

Figure 1: Structure and cytosolic catalytic activity of *Clostridium botulinum* C3 toxin. 4
Figure 2: Schematic illustration of bone remodeling phases. 11
Figure 3: Factors in osteolytic modulation of bone-resident cells by breast cancer metastases. 14
Figure 4: Schematic illustration of BC bone metastasis and the structure of the $(JM173)_3$-Avi-C3 16
Figure 5: Biotinylation of ^{Cys}C3bot1 and JM173 and assembly on the avidin platform. 18
Figure 6: Schematic illustration of the CRISPR/Cas9 system 21
Figure 7: Schematic illustration of $C3_{E174Q}$_Cas9 structure and uptake route. 25
Figure 8: Optimization of ^{Cys}C3 purification. 60
Figure 9: Purity and enzyme activity tests of ^{Cys}C3 and B-C3. 61
Figure 10: Optimizing the assembly of B-JM173 and B-C3 on different biotin-binding platforms. 62
Figure 11: Toxicity studies on different breast cancer cell lines and zebrafish embryos. .. 63
Figure 12: Flow cytometric analysis of CXCR4 expression level in different cell lines. 65
Figure 13: Flow cytometric analysis of the binding of $(JM173)_3$-^{BDP}Avi-C3 to CXCR4. 66
Figure 14: Binding and uptake of $(JM173)_3$-Avi-C3 in CXCR4 expressing cells verified by fluorescence microscopy. 69
Figure 15: Influence of $(JM173)_3$-^{BDP}Avi-C3 on the intracellular ADP-ribosylation status of Rho and breast cancer cell proliferation. 70
Figure 16: $(JM173)_3$-^{BDP}Avi-C3 decreases osteoclast differentiation and resorption activity. 72
Figure 17: C3 toxin increases the gene expression of differentiation and proliferation markers in MC3T3 cells during osteoblastogenesis. 73
Figure 18: Cloning and expression of C3_Cas9 and $C3_{E174Q}$_Cas9. 75
Figure 19: Cleavage assay with gene fragments of eGFP, LSR and CD33 treated with Cas9, C3_Cas9 and $C3_{E174Q}$_Cas9 and the respective targeting or non-targeting sgRNA. 76
Figure 20: C3_Cas9- or $C3_{E174Q}$_Cas9-treated J774A.1 macrophages analyzed by light- and fluorescence microscopy. 78

Figure 21: Analysis of the ADP-ribosylation status of Rho in various macrophage-like cells 80
Figure 22: $C3_{E174Q}$_Cas9 enters cytosol and nucleus of monocytes and macrophages. 81
Figure 23: Amino acid sequence of $C3_{E174Q}$_$Cas9^{NLs\text{-}His}$ in single letter code. 124
Figure 24: SDS-PAGE gel of $DyLight^{488}$ labelled proteins detected at 480 nm. 124
Figure 25: Gene fragments used in this thesis 125

3 List of Tables

Table 1: List of used chemicals and corresponding manufacturers 28
Table 2: List of used consumables and kits 31
Table 3: List of used devices 32
Table 4: List of used aqueous buffers and solutions and their composition 34
Table 5: List of used proteins, enzymes and toxins 36
Table 6: Antibodies and binding proteins used for Western Blot or flow cytometry 37
Table 7: List of used plasmids for cloning or gene amplification approaches 38
Table 8: Primer for cloning and sequencing approaches 38
Table 9: List of enzymes used for cloning or PCR approaches 39
Table 10: DNA oligos for single guide RNA (sgRNA) synthesis 40
Table 11: Composition of media used for cultivation of prokaryotic cells 40
Table 12: Prokaryotic cell types with corresponding culture media 40
Table 13: Eukaryotic cell lines with corresponding culture media. 41
Table 14: List of used software and online tools 42
Table 15: Thermocycler program for amplification of BamHI_$Cas9^{NLS\text{-}His}$_NcoI 45
Table 16: Thermocycler program for colony PCR 47
Table 17: Thermocycler program for amplification of an eGFP gene fragment 50
Table 18: Thermocycler program for genomic PCR to amplify an LSR gene fragment 51
Table 19: Raw data of the endotoxin measurements in C3_Cas9 and $C3_{E174Q}$_Cas9 126

4 List of Abbreviations

Abbreviation	**Full designation**
4T1	Murine adenocarcinoma cell line
A431	Human epidermoid carcinoma cell line
A549	Human lung carcinoma cell line
AAV	Adeno-associated viruses
ADP	Adenosine diphosphate
AP	Alkaline Phosphatase
AP-1	Activator protein-1
ARTT	ADP-ribosylation toxin-turn-turn
Avi	Avidin
B2M	β2-Microglobulin
BC	Breast carcinoma
B-C3	Biotinylated C3bot1
BDP	Bodipy
^{BDP}Avi	Bodipy labelled Avidin
BGLAP	Osteocalcin, bone gamma-carboxyglutamate protein
B-JM173	Biotinylated JM173
C2	*Clostridium botulinum* C2 toxin
C2I	A-component of the C2 toxin
C2IIa	proteolytically activated B-component of the C2 toxin
C2IN	non-toxic N-terminal part of C2I
C3bot1/2	*Clostridium botulinum* C3 toxin isoforms 1 and 2
C3cer	Bacillus cereus C3 toxin
$C3_{E174Q}$	*Clostridium botulinum* C3 toxin isoform 1 with E174Q mutation
$C3_{E174Q}$_Cas9:sgRNA	RNP complex of $C3_{E174Q}$_Cas9 and sgRNA
C3larvin	*Paenibacillus larvae* C3 toxin isoform
C3lim	*Clostridium limosum* C3 toxin
C3stau1/2/3	*Staphylococcus aureus* C3 toxin isoforms 1, 2 and 3
Cas	CRISPR associated protein
CD33	Cell surface protein of monocytic cells

Abbreviation	Full designation
CRISPR	Clustered regulatory-interspaced short palindromic repeat
CRM197	*Corynebacterium diphtheriae* diphtheria toxin with G52E mutation
crRNA	Precursor CRISPR RNA
CSF-1	Colony-stimulating factor 1
Ct	Cycle threshold
CXCL12	C-X-C motif chemokine ligand 12, stromal cell-derived factor 1
CXCR4	C-X-C chemokine receptor 4
CXCR7	Atypical chemokine receptor 3
^{Cys}C3	C3bot1 with N-terminal cysteine residue
Cyt	Cytosol
DTA	A-component of *Corynebacterium diphtheriae* diphtheria toxin
E. coli	*Escherichia coli*
eGFP	enhanced green fluorescent protein
EphB4	Osteoblastic ephrin type-B receptor 4
EPI-X4	Endogenous peptide inhibitor of CXCR4
ER	Estrogen receptor
Fc	Crystallizable human immunoglobulin G antibody fragment
FDA	Food and Drug Administration
FI	Fluorescence intensity
FP	Forward primer
G-/F-actin	Globular/filamentous actin
GAP	GTPase-activating proteins
GDI	Guanine nucleotide dissociation inhibitor
GDP	Guanosine diphosphate
GEF	Guanine nucleotide exchange factors
GST	Glutathione-S-transferase
GTP	Guanosine triphosphate
HCT-116	Human colon cancer cell line
HDR	Homology-directed repair
HER2	Human epidermal growth factor receptor 2
HIV	human immunodeficiency virus

Abbreviation	Full designation
Hsp90	Heat shock protein 90
IL	Interleukin
J774A.1	Murine macrophage cell line
JM173	Peptide acting as CXCR4 antagonist. Amino acid sequence in one letter code: (d-I)LRWSRK-NH_2
KI67	Antigen used as late differentiation marker in osteoblastogenesis
LSR	Lipolysis-stimulated lipoprotein receptor
MALDI-ToF	Matrix-assisted laser desorption/ionization time-of-flight
MAPK	Mitogen-activated protein kinase
MC3T3	Murine preosteoblastic fibroblast-like bone cell line
MCF7	Human adenocarcinoma cell line
MDA-MB231	Human adenocarcinoma cell line
miRNA	Micro ribonucleic acid
mRNA	Messenger ribonucleic acid
NAD^+	Nicotinamide adenine dinucleotide
NF-κB	Nuclear Factor kappa-light-chain-enhancer of activated B cells
NHEJ	Non-homologous end joining
NHS	N-hydroxysuccinimide
NLS	Nuclear localization sequence
ns	Non-significant
Nuc	Nucleus
OPG	Osteoprotegerin
PAM	Protospacer adjacent motifs
PI3K	Phosphatidylinositol-3-kinase
Pix2	*Paenibacillus larvae* C3 toxin isoform
PN	Phosphate-nicotinamide
PR	Progesterone receptor
PTH	Parathyroid hormone
RANK	Receptor activator of nuclear factor kappa-light-chain-enhancer of activated B-cells

Abbreviation	Full designation
RANKL	Receptor activator of nuclear factor kappa-light-chain-enhancer of activated B-cells ligand
RAW 264.7	Murine monocytic cell line
RGD	Arginine-glycine-aspartic acid structure motif
Rho	Ras homologue GTPases (A, B and C when not indicated otherwise)
$Rho_{non\text{-}ADP\text{-}rib.}$	Rho protein not modified by ADP-ribosylation
RNP	Ribonucleoprotein
RP	Reverse primer
RUNX2	Runt-related transcription factor 2
sgRNA	Single guide ribonucleic acid
$sgRNA^{CD33}$	sgRNA targeting the CD33 gene
$sgRNA^{eGFP}$	sgRNA targeting the eGFP gene
$sgRNA^{LSR}$	sgRNA targeting the LSR gene
siRNA	Small interfering ribonucleic acid
SpCas9	CRISPR associated protein 9 isolated from *Streptococcus pyogenes*
STS	Serine-threonine-serin structure motif
SupT1	Human T-cell lymphoma cell line
SupT1ΔCXCR4	SupT1 cells with a CXCR4 knockout
TGF-β	Transforming growth factor beta
THP-1	Human monocyte cell line
THP-1 M0	THP-1 cells differentiated into macrophages by PMA
TNF-α	Tumor necrosis factor alpha
tracrRNA	Small trans-acting CRISPR RNA
TRAP	Tartrate-resistant acid phosphatase
VCAM-1	Vascular adhesion molecule 1

1 Introduction

1.1 Bacterial Toxins

Bacterial toxins are potent biomolecules and the main virulence factors in various infectious diseases. According to the mode of action and chemical composition of the bacterial toxins they are subdivided into endo- and exotoxins. Endotoxins are heat-stable lipopolysaccharides located in the outer membrane of Gram-negative bacteria. They are released upon bacterial lysis and trigger non-specific immune responses, such as fever and inflammation. In contrast, exotoxins are proteins actively secreted by both Gram-positive and Gram-negative bacteria. They are highly potent, target specific cellular pathways, and are strongly immunogenic [1,2]. Exotoxins are classified according to their mode of action, cellular target or structure. The structure of exotoxins can usually be divided into an enzymatically active "A" subunit and a binding- and translocation "B" subunit, which are expressed as a single protein (e.g. diphtheria toxin) or as individual proteins (e.g. *Clostridium botulinum* C2 toxin) [3–5]. However, since not all exotoxins exhibit the AB-type structure, they can also be classified via their mode of action. While some exotoxins lead to membrane-disruption (e.g. hemolysins), enzymatically active toxins target intracellular substrates of hosts leading to blockage of neurotransmitter signaling (neurotoxins), cytokine release and systemic inflammation (superantigens), breakdown of the intestinal barrier (enterotoxins) or apoptosis of cells (cytotoxins) [1,2,6,7]. Minimal doses in the low nanogram per kilogram body weight range released in human or animals can cause severe progression of the associated disease, potentially leading to death [1]. Both most potent bacterial toxins, namely botulinum neurotoxin and tetanus toxin, originate from Clostridia and have LD_{50} values below three nanograms per kilogram body weight in human [8], emphasizing their potency.

Despite the high toxicity of exotoxins they have also emerged as valuable tools in biomedical research and therapeutic development [9]. They are in clinical use for the treatment of neurological disorders like spasms and immune-related diseases like chronic inflammatory pain (e.g. Botox®) [10,11]. In addition, toxin variants like the non-toxic diphtheria toxin mutant CRM197 shows inhibition of invasion, migration and angiogenesis of cancer cells and can be used as a cargo delivery system over the blood brain barrier as

well as a carrier protein for a variety of conjugate vaccines [12–15]. Further, a modified version of *Clostridium botulinum* C3 cytotoxin has already reached phase I/IIa clinical trials in form of Cethrin^{TM}, a cell permeable C3-variant used for the treatment of spinal cord injury. This thesis focuses on the pharmacological potential of C3 toxin as drug and transport system due to its unique cell type-selective targeting properties.

1.2 Bacterial ADP-Ribosylating C3 Toxins

C3-like exoenzymes are secreted by several pathogenic bacteria including *Clostridium botulinum* (C3bot1 and C3bot2), *Clostridium limosum* (C3lim), *Bacillus cereus* (C3cer) and *Staphylococcus aureus* (C3stau1, C3stau2 and C3stau3) [16–19]. Since the C3bot1 toxin was initially discovered in *Clostridium botulinum* strains C and D as a phage-encoded transferase, it represents the prototype of this toxin family [16,20]. It is expressed as a 25 kDa single polypeptide chain and shares sequence identities of around 65% to the isoform C3bot2 and around 35% among the other named C3-like exoenzymes [19,21–25].

Despite the modest sequence identity across the family of C3 toxins, they share a conserved enzymatic core with preserved structural motifs for specific transfer of an ADP-ribose moiety from NAD^+ to the asparagine of small Rho GTPases at position 41 (N_{41}) [26–29]. The catalytic center of C3bot1 is organized in antiparallel β-sheets surrounded by several loops for substrate recognition, substrate binding and alignment with the co-substrate (Figure 1a) [30]. Recognition and binding of the substrates RhoA, RhoB or RhoC (in the following summarized as Rho) are facilitated by the flexible ADP-ribosylation toxin-turn-turn (ARTT, I_{166}-E_{174}, highlighted pink in Figure 1a) loop [27,31]. It has also been shown that the amino acid E_{174} plays an essential role for NAD binding and the catalytic and biological activity of C3bot1, since an exchange to glutamine ($E_{174}Q$) leads to a lack in enzyme activity. The serine-threonine-serin (STS, S_{134}-S_{136}, highlighted in green in Figure 1a) motif is responsible for maintaining the reaction cavity of C3bot1, while the directly linked phosphate-nicotinamide (PN, L_{137}-R_{146}, highlighted in blue in Figure 1a) loop is essential for positioning of the co-substrate NAD^+ and stabilization of the transition state during ADP-ribose transfer to Rho [30,32] (Figure 1a).

Rho GTPases represent a subfamily of the Ras superfamily majorly regulating the assembly and organization of the actin cytoskeleton, affecting related cellular processes like cytokinesis, phagocytosis or migration [33–36]. In addition, Rho regulates several

transcription factors including the nuclear factor kappa-light-chain-enhancer (NF-κB), G_1 cell cycle progression, vesicle trafficking and cell polarity [37–39]. Therefore, Rho GTPases cycle between an inactive GDP-bound and an active GTP-bound state for control of downstream signaling pathways [40]. While the activation is catalyzed by guanine nucleotide exchange factors (GEFs) by replacing GDP with GTP, the transition of Rho to the inactive state is catalyzed by GTPase-activating proteins (GAPs) via increasing the intrinsic rate of GTP hydrolysis of Rho [41–44]. To maintain the inactive state, guanine nucleotide dissociation inhibitors (GDIs) are bound, leading to a separation of the GTPase from the cell membrane and therefore to an inhibition of spontaneous GDP-GTP exchange [45]. Mono-ADP-ribosylation of Rho by C3-like toxins leads to an accumulation of GDI-bound Rho in the cytosol and therefore to an inhibition of the translocation into its membrane-bound active state [46–48] (Figure 1b). This results in a redistribution of the actin cytoskeleton, altering numerous actin-dependent processes like epithelial and endothelial barrier functions, phagocytosis in immune cells, cytokine production, cell adhesion and migration [35,49–52].

The C3 toxins C3bot, C3lim, C3cer and C3stau lack the canonical cell-binding and translocation domain found in many bacterial AB-type toxins [20]. However, there have been identified further C3-like toxins secreted by *Paenibacillus larvae* (C3larvin and Plx2) that are expressed as binary toxins with separated A and B subunits, comparable to the pore forming *Clostridium botulinum* C2 toxin [53,54]. Besides these AB-type toxins, it is only poorly understood how C3-like exotoxins bind and enter cells. It has been shown that vimentin contributes to the binding of C3bot1 to cells but is not solely responsible for it, as a knockout only diminishes but does not inhibit C3 intoxication [55]. In addition, C3 exotoxins harbor a conserved arginine-glycine-aspartic acid (RGD, R_{88}-D_{90} for C3bot1, highlighted in purple in Figure 1a) motif known as major integrin binding site that is proposed to be involved in host cell binding of C3 [56–58].

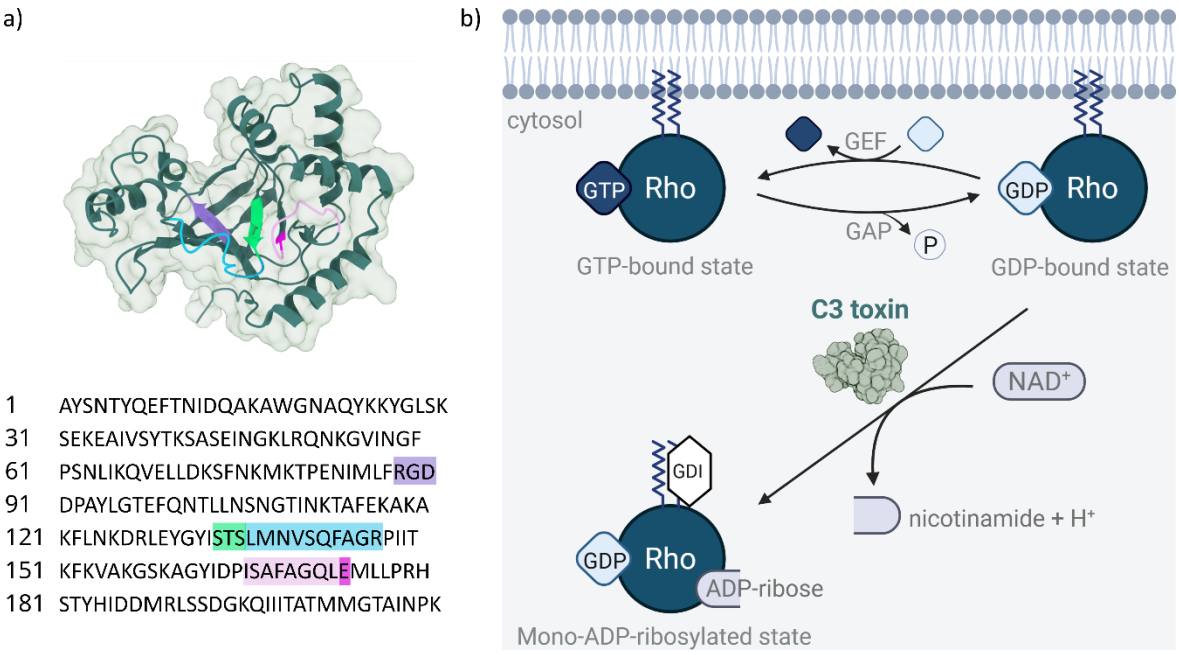


Figure 1: Structure and cytosolic catalytic activity of Clostridium botulinum C3 toxin. a) Ribbon and surface diagram of Clostridium botulinum C3bot1 at 1.7 Å resolution (protein databank entry 1G24, [30]). The integrin binding motif Arg-Gly-Asp (RGD, purple), the STS-motif for maintaining the reaction cavity (green), the phosphate-nicotinamide (PN) loop for NAD^+ binding (blue), the ADP-ribosylation toxin turn-turn (ARTT) loop for recognition of Rho (pink) and conserved residues essential for enzymatic activity (magenta) are highlighted in the diagram and the amino acid sequence [20,30]. b) Schematic reaction scheme of C3 toxins catalyzing the mono-ADP ribosylation of Rho by covalently transferring an ADP-ribose moiety from NAD^+ to the cytosolic Rho. This enzymatic reaction leads to an accumulation of inactive, GDP-bound Rho preventing its cycling to an active GTP-bound state by the guanine nucleotide exchange factor (GEF) [41,43]. Since the reverse reaction of Rho cycling catalyzed by the GTPase-activating protein (GAP) persists, an increasing amount of Rho is transferred to the inactive, GDP-and GDI-bound state [29,45,48,56,59]. Illustration design inspired by [20,29] and created with ChimeraX 1.10.1 and BioRender (Stadler, N. (2026) https://BioRender.com/g2np2vg)

Although the mechanism of cellular binding of C3 toxins are unknown, cell type dependent differences in the intoxication are observed. While most cell types need C3 concentrations in the micromolar range and extended incubation times for intoxication, monocytic cells including macrophages, dendrites and osteoclasts are intoxicated by nanomolar C3 concentrations within several hours [60–64]. After binding of C3 to the cell surface, it needs to be internalized to modify the cytosolic Rho proteins. So far, several hypotheses have been postulated to describe the membrane translocation route of C3 but no distinct endocytotic mechanism has been identified yet. Studies showed that the uptake is independent of caveolae, clathrin and the disruption of cytoskeletal structures like actin and microtubule filaments, while inhibiting dynamin-dependent endocytosis reduced the cytosolic C3 uptake [65]. Furthermore, the N-terminal α_1-helix of clostridial C3 toxins could be involved in their binding and uptake since C3larvin lacking this helix can only enter

murine J774A.1 cells after rescue by fusion with the missing helical structure [66,67]. Even though C3 toxins could be detected in early endosomes of macrophages, the mechanism for the cytosolic release of C3 has not been fully elucidated [66]. There are contrary findings of the involvement of the vacuolar proton ATPase for the acidification of C3-loaded endosomes since the ATPase inhibitor bafilomycin A1 alters the uptake of C3 only at low toxin concentrations [65,66]. However, in addition to the co-localization of C3bot1 with early endosomes recent data show, that the α_1-helix of C3larvin triggers massive swelling of lysosomes leading to a disruption of the lysosomal membrane and therefore to a release of active C3 toxin into the cytosol [68,69].

Even though the binding and uptake mechanism of C3 toxins is not fully understood, the high substrate specificity and the tendency towards cell type-selective intoxication lead to various concepts for the application of C3 toxins as tools for cell type-selective drug delivery or down-modulation of Rho-signaling.

1.3 C3-like Toxins as Pharmacological Tools

Bacterial toxins harbor distinct properties making them ideal pharmacological tools, including cell entry without damaging the cell integrity, immense potency as well as high cell type and substrate specificity [70]. C3bot1 acts, depending on the intoxicated cell type, in a nanomolar to micromolar range specifically inactivating the small GTPases RhoA, RhoB and RhoC [27,28,61]. Based on this high substrate specificity of C3bot1 it has been widely used to investigate the role of Rho, unraveling its involvement in stress fiber formation, induction of cell adhesions, integrin signaling, control of several kinases, cell cycle progression and various more cellular processes [38,71–73].

To study these effects, active C3 toxin needs to be introduced into the cytosol. While monocytic cells efficiently take up C3 in low concentrations and after a short period of time, other cell lines were treated with osmotic shocks or microinjection in order to deliver C3 into the cytosol [72,74]. Later, C3 was brought into non-monocytic cells in combination with pore-forming toxins, transport peptides, or as fusion toxins to enable efficient cytosolic uptake. One example is a fusion toxin consisting of C3bot1 N-terminally coupled to the binding and translocation domain of diphtheria toxin [75]. However, this limits the transport of C3 into cells expressing the diphtheria toxin receptor heparin-binding epidermal growth factor-like growth factor [76]. In comparison, the *Clostridium botulinum*

C2 toxin binds to asparagine-linked carbohydrate structures present on the cell surface of various cells, making it a promising transport tool for C3 [77]. The non-toxic N-terminal end of the C2 active component C2I (C2IN) was fused genetically to C3lim, resulting in the fusion toxin C2IN-C3lim. In combination with the pore-forming C2 toxin binding and translocation moiety C2IIa, C2IN-C3lim enters multiple cell types specifically leading to mono ADP-ribosylation by C3lim without showing effects of C2 intoxication [78]. In addition to hijacking mechanisms of other bacterial toxins for delivery of C3-like toxins, several transport peptides have been established. One approach has been the combination of C3bot1 with the human immunodeficiency virus (HIV) Tat peptide permitting transduction of the fusion protein across the plasma membrane by triggering macropinocytosis [79,80]. Another strategy for C3bot1 delivery into non-monocytic cells was the dual chemoselective functionalization of C3bot1 via 1,6-addition on N-alkylpyridinium reagents. As a proof-of-concept, C3bot1 was functionalized with an RGD motif and an fluorophore leading to an increased cytosolic uptake of enzymatically active C3bot1 into the cytosol of integrin overexpressing A549 lung cells [81,82].

However, studying the role of Rho signaling pathways and the interplay between RhoA and RhoB with the help of C3-like toxins also revealed their therapeutic features. Rho proteins are major negative regulators in axonal growth and repair after neuronal injury [83]. A targeted inhibition of Rho by C3bot1 toxin has been shown to facilitate nerve growth and regeneration after spinal cord injury and led to increased branching of hippocampal neurons, making C3bot1 a potential drug for treatment of nerve damage [84,85]. In addition to these neurotrophic properties, C3lim decreased the resorption activity and the osteoclastogenesis of osteoclast-like cells differentiated from RAW 264.7 cells [64]. This targeted pharmacological manipulation of osteoclast-like cells by C3lim could lead to development of therapeutic strategies against osteoclast hyperactivity-associated diseases like osteoporosis or rheumatoid arthritis [86].

C3-like toxins can not only be exploited as enzymatically active components to inhibit intracellular Rho signaling pathways but have also beneficial properties in their enzyme-deficient form. Therefore, a C3 toxin mutant was designed, where the glutamic acid (E) at position 174 (highlighted magenta amino acid in Figure 1a) was replaced by glutamine (Q). Since this amino acid is part of the ARTT loop involved in substrate and co-substrate recognition and binding, this exchange results in the enzymatically inactive $C3_{E174Q}$.

However, this mutant retains its ability of entering cells, making it a promising cell type-selective transport system for monocyte-derived cells [87–89]. Even though the exact uptake mechanism of C3 toxins is yet unknown, several cargo molecules were successfully attached to $C3_{E174Q}$ for cytosolic transport. In first attempts, a genetically fused chimera of $C3_{E174Q}$ with the reporter enzyme C2I (~50 kDa) was generated. The fusion toxin $C3bot1_{E174Q}$_C2I led to cell-type selective ADP-ribosylation of G-actin by C2I in the cytosol of macrophages including murine J774A.1 and RAW 264.7 cells as well as human primary macrophages but not epidermal cell lines [4,62]. A more recent publication examined a construct consisting of enhanced green fluorescent protein (eGFP) genetically fused to $C3_{E174Q}$. Consistent with $C3bot1_{E174Q}$_C2I, eGFP_$C3bot_{E174Q}$ treatment resulted in cytosolic release of eGFP specifically in macrophages and human dendritic cells [68].

Another approach to utilize $C3_{E174Q}$ as a cytosolic delivery tool is its coupling to streptavidin creating a modular transport platform to bind biotinylated cargos. This could be achieved by genetic fusion of $C3_{E174Q}$ with streptavidin, as shown for the transport of biotinylated enzymatically active *Corynebacterium diphtheriae* diphtheria toxin (DTA) or by chemical coupling of $C3_{E174Q}$ with streptavidin via thioether linkage as demonstrated for the transport of biotinylated RNase A. However, using the streptavidin-biotin technology also led to an increased uptake of DTA or RNase A into the cytosol of epithelial cells or fibroblasts [90,91]. This change in cell type-selectivity was most likely attributed to the streptavidin moiety influencing the interaction of the bioconjugated constructs with cell surface proteins, as streptavidin has been reported to harbor an RYD-motif involved in cell adhesion processes [92]. Since the coupling strategy of $C3_{E174Q}$ to cargo molecules via streptavidin/biotin-systems results in reduced cell type-selectivity, direct coupling of $C3_{E174Q}$ and cargo via thiol-maleimide click chemistry was tested. Therefore, a single cysteine residue was introduced at the N-terminus of $C3_{E174Q}$ to enable the binding to a maleimide-labelled cargo molecule. Via this method, the small fluorophore DyLight™ 488 (in the following $Dylight^{488}$, 0.8 kDa), the larger fluorescein-isothiocyanate labelled polyethylene glycol (5 kDa) and C2I (50 kDa) were successfully transported into macrophages and dendritic cells [68]. Although it has been shown that the transport of these cargos depends on $C3_{E174Q}$, they have not been tested on non-monocytic cells to prove cell type-selectivity of the transport, especially compared to the streptavidin/biotin-system.

The following sections describe the application of *Clostridium botulinum* C3bot1 toxin either as a pharmacological active component or as a cell type-selective cargo transport tool in the context of this thesis.

1.3.1 C3bot1 Against Breast Cancer Metastasis-Related Osteolysis in the Bone

Breast Cancer Types and Treatment Options

The leading cause of death worldwide is cancer. In 2020, nearly 10 million deaths were recorded related to different types of cancer, especially lung, colon, rectum, liver and breast cancers [93]. In 2022, the latter was the most common cancer occurring in women in 157 out of 185 countries with 2.3 million cases and 670,000 deaths globally [94]. It is estimated that by 2025 over 30% of new cancer diagnoses in women will be breast cancer cases [95]. The major risk factor for developing breast carcinoma (BC) is the female gender, since only 0.5-1% of men are affected, while other factors like increasing age, obesity, exposure to harmful substances (e.g. alcohol, tobacco, radiation) and genetic family history increase the risk of suffering from BC. Preventive medical screenings by mammography to detect pre-clinical lesions in the breast tissue and early diagnoses when discovering symptoms of BC can reduce mortality drastically. The most abundant symptom is the formation of breast lumps followed by nipple abnormalities, breast pain and non-breast related symptoms like back pain and weight loss [96,97].

The treatment options for BC depend on the cancer subtype as well as the stage of spreading to distinct body parts and aim not only to eliminate BC cells but also to minimize recurrence. Breast cancer can be divided into three major subtypes, namely the luminal-type expressing the estrogen receptor (ER) and/or the progesterone receptor (PR), the human epidermal growth factor receptor 2 (HER2) gene-amplified type and the basal-like type with a phenotype lacking ERs, PRs and HER2 (triple negative) [94,98]. To target any kind of BC cell, surgery like lumpectomy or mastectomy is combined with radiation therapy and targeted medication including hormonal therapies, chemotherapy or immunotherapy. Endocrine therapies target luminal type BC cells by modulating ERs or PRs. One example is tamoxifen, an ER antagonist inhibiting downstream signaling and leading to a cell cycle arrest in the G1 phase. Hence, cell proliferation is inhibited, and cell death is initiated [99,100]. HER2-positive cells occur in 15% of BC and can be targeted by immunotherapy. Trastuzumab and pertuzumab are monoclonal antibodies binding the extracellular domain

of HER2. They are often used as a combination therapy to inhibit HER2-mediated signaling and receptor dimerization, resulting in downregulation of cell growth and spread [101,102]. Lapatinib is a small-molecule tyrosine kinase inhibitor binding to the intracellular domain of HER2 and inhibiting mitogen-activated protein kinase (MAPK) and phosphatidylinositol-3-kinase (PI3K) pathways. It is often used in combination with trastuzumab for treatment of metastatic BC cells since it is able to pass the blood brain barrier [103]. Triple negative BC can be treated with chemotherapeutic agents like docetaxel or paclitaxel, both stabilizing microtubules leading to a mitotic arrest and cell death [102,104]. Another example is the prodrug capecitabine, which inhibits the thymidylate synthase resulting in disruption of DNA synthesis and repair [105].

In further progressed stages of BC, not only the BC cells located in the breast but also metastases need to be addressed during the treatment. Metastasis can be initiated by epithelial to mesenchymal transition of BC cells leading to a loss of cell-cell adhesion and the acquisition of mesenchymal characteristics [106]. Due to a lack of inter-endothelial junctions and discontinuous basement membranes, lymphatic vessels are considered the first site of metastasis in breast cancer (stage II and stage III). Spreading of BC cells via the blood stream to distant organs (stage IV) often requires the recruitment of macrophages or pericytes secreting signal molecules leading to a disruption of epithelial layers of blood vessels for BC cell entry and targeting the cells to specific organs [107–109]. While metastases in stage II and stage III can be detected with sentinel lymph node biopsy and treated in radiation therapy, patients suffering from stage IV metastatic BC can only be treated palliatively with a maximum survival of around 40 months [110,111]. Predominant sites of metastases in late-stage breast cancer are lungs, brain and bones, characterized by individual organ-specific gene expression patterns of metastatic BC cells. While the assessment of lung and brain tissue is limited for BC cells due to narrow lung capillaries and the blood brain barrier, the bone sinusoids are more permissive and thus a primary target of metastasis [112–114]. Summarized, BC in stage II and III can only be cured successfully by treating the metastases in addition to the primary breast cancer itself, especially to prevent recurrences. The additional treatment of co-morbidities in stage IV BC patients can improve their live quality.

Cells Involved in Bone Remodeling

This thesis focuses on the treatment of breast cancer metastases in the bone niche and targeting the respective co-morbidities like the disturbed homeostasis in bone remodeling. The bone tissue undergoes a continuous remodeling process to repair damaged bones and maintain mineral homeostasis. There are several types of cells involved in bone remodeling, namely osteoclasts, osteoblasts, osteocytes and immune cells [115]. Osteoblasts are specialized cells developed from pluripotent mesenchymal stem cells under control of early differentiation markers such as runt-related transcription factor 2 (RUNX2) and activator protein-1 (AP-1), as well as late differentiation markers like the bone gamma-carboxyglutamate protein (BGLAP, osteocalcin) [116–118]. Osteoblasts express bone matrix proteins and are responsible for bone mineralization. Furthermore, they release osteoclastogenic factors leading to differentiation and activation of osteoclasts, terminally differentiated myeloid cells representing the counterpart of bone homeostasis [115,119]. Crucial cytokines for osteoclast differentiation, expansion and survival are among others the colony-stimulating factor 1 (CSF-1) and the receptor activator of nuclear factor kappa-light-chain-enhancer of activated B-cells ligand (RANKL). Osteoclasts show distinct morphological and phenotypic characteristics including the expression of tartrate-resistant acid phosphatase (TRAP), multinuclearity and a ruffled membrane for insertion into the bone-apposed plasma membrane. They are responsible for bone degradation by removing mineralized bone matrix [119]. Osteocytes are a sub-population of terminal differentiated osteoblasts and form a network throughout the mineralized bone with an abundance of up to 95% of all bone cells. They respond to mechanical strain and associated microdamage by initiating remodeling processes [120]. The role of immune cells like lymphocytes, megakaryocytes and specialized bone tissue macrophages (osteomacs) in maintaining physiological bone homeostasis is not yet fully understood. Nevertheless, they have been shown to be responsible for the crosstalk between bone and bone marrow in several pathological diseases including ovariectomy-induced bone loss or bone marrow fibrosis in hyperparathyroidism. While B-cell lymphocytes and megakaryocytes restrain osteoclastogenesis, osteomacs depletion leads to a complete loss of associated mature osteoblasts [121–123].

The Process of Bone Remodeling

Osteoblasts and osteoclasts are the main cell types responsible for remodeling of the bone. Shifting the balance between bone resorption and bone formation results in diseases like osteoporosis characterized by increased loss of bone mass or sclerosteosis, a medical condition with excessive calcification and increased bone mass [124–126]. The remodeling process takes place in multicellular clusters combining osteoclast- and osteoblast activity to ensure only minimal bone volume changes during physiological bone remodeling [127,128].

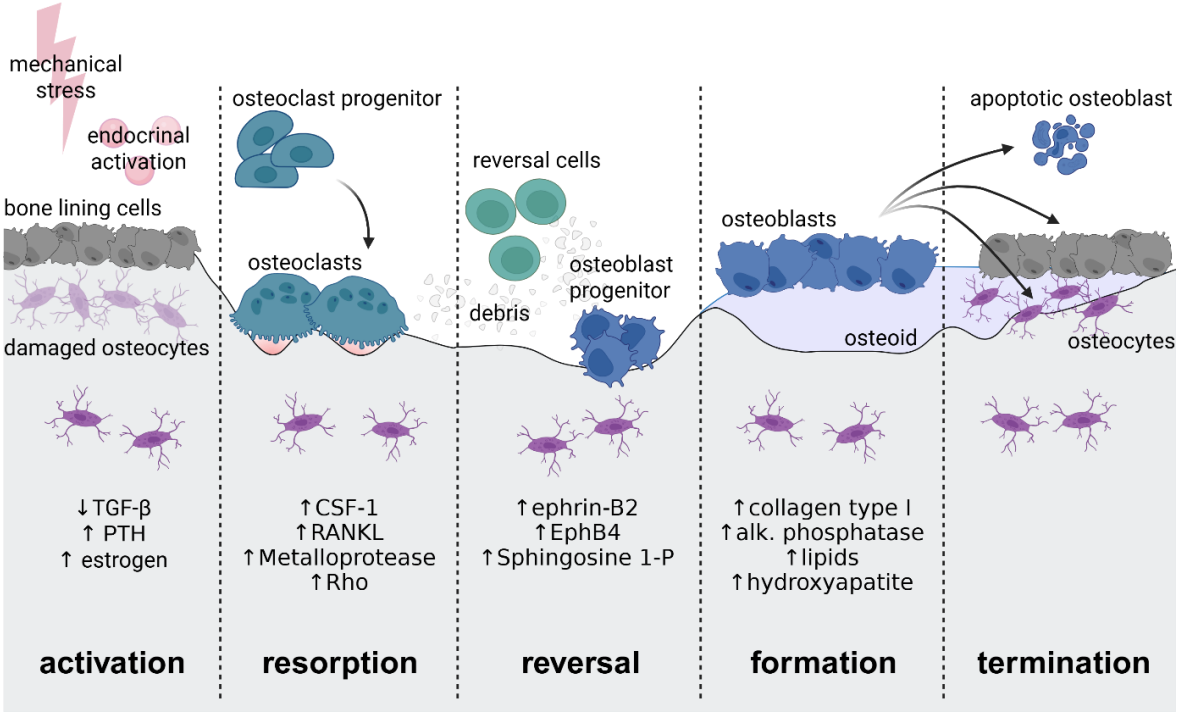


Figure 2: Schematic illustration of bone remodeling phases. Activation of bone remodeling by mechanical stress on osteocytes or endocrinal activation of osteoblastic bone lining cells by parathyroid hormone (PTH) and estrogen leads to decrease local transforming growth factor beta (TGF-β) concentrations. This triggers the recruitment and differentiation of osteoclast progenitor cells in the resorption phase via increased levels of the colony-stimulating factor 1 (CSF-1) and the receptor activator of nuclear factor kappa-light-chain-enhancer of activated B-cells ligand (RANKL) and increases the secretion of metalloproteases from mature osteoclasts. The acidic sealing zone for bone degradation is formed by osteoclasts inducing the formation of an actin ring via Rho GTPase signaling. Mononuclear undetermined "reversal cells" remove bone debris and recruit osteoblast progenitor cells via unknown signals. In addition, the interplay between osteoblastic ephrin type-B receptor 4 (EphB4) and osteoclastic ephrin-B2 as well as the signal factor Sphingosine 1-phosphate (Sphingosine 1-P) trigger osteoblast differentiation and survival of mature osteoblasts. Those form the new osteoid by secreting collagen type I, alkaline (alk.) phosphatase, lipids and hydroxyapatite. The remodeling process is terminated by osteoblast apoptosis, osteoblast differentiation to osteocytes or embedding of osteoclasts to form bone lining cells. Graphic based on the sources [129–139]. Design inspired by [140]. Created in BioRender (Stadler, N. (2026) https://BioRender.com/96xqhzs)

Bone remodeling can be divided into five phases including activation, resorption, reversal, formation and termination (Figure 2). The activation phase can be initiated by mechanical strain leading to apoptosis of osteocytes and lowering the local concentration of the transforming growth factor β (TGF-β), which normally inhibits osteoclastogenesis [120,129]. In addition, endocrinal activation of osteoblasts by the parathyroid hormone (PTH) or estrogen lead to recruitment of osteoclast precursor cells by chemoattraction, to elevated CSF-1 and RANKL concentrations to promote osteoclast differentiation and to stimulation of metalloprotease secretion for degradation of unmineralized osteoid [130–132]. The resorption phase is initiated by the binding of osteoclasts to the exposed RGD-adhesion sites within the mineralized bone via integrin, leading to the formation of a sealing zone isolating the resorptive microenvironment from extracellular space [133,141,142]. This is accomplished by the formation of an actin ring which is controlled by the activation of Rho proteins like Rho A and Rac in the osteoclasts [134,143]. Once bound to the bone, protons are transported into the sealing zone by a H^+-ATPase [144]. Together with chloride anions introduced by electroneutral chloride/bicarbonate exchangers HCl is generated acidifying the sealing zone to a pH of approximately 4.5 [145]. This triggers the degradation of the mineralized bone by collagenolytic lysosomal proteases like cathepsin K [135]. Following osteoclast-mediated resorption, mononuclear undetermined cell lineages remove remaining collagen and matrix debris in the reversal phase. Since different cell markers such as alkaline phosphatase, MOMA-2 (monocyte + macrophage antibody-2) or F4/80 (glycoprotein on macrophages) could be detected on these “reversal” cells, they could originate from the osteoblast lineage or be osteomacs [146–149]. While bone resorption takes about three weeks, osteoblastic bone formation proceeds for up to six months [139]. The reversal phase describes the transition from bone degradation by osteoclasts to bone renewal by osteoblasts and their pre-cursor cells and is controlled by several factors. Osteoclasts express ephrin-B2, a ligand that binds to the osteoblast ephrin type-B receptor 4 (EphB4). This cell-anchored bidirectional receptor-ligand complex enhances the osteogenic differentiation of osteoblasts while simultaneously suppressing osteoclast differentiation [136]. Another factor involved in the reversal phase is Sphingosine 1-phosphate secreted by osteoclasts, leading to recruitment of osteoblast progenitor cells and promoting survival of mature osteoblasts [137]. The recruited cells secrete molecules for re-mineralization in the formation phase of the bone including

collagen type I, alkaline phosphatase, lipids and hydroxyapatite [138]. Yet unknown termination signals conclude the remodeling cycle leading to osteoblast apoptosis and osteoblast embedding into the osteoid matrix for differentiation to osteocytes or forming the bone surface as inactive bone lining cells [139]. Following complete re-mineralization, a resting state is maintained until the next remodeling is initiated.

Breast Cancer Metastases in the Bone Niche – A Vicious Cycle

To reach the bone tissue, cells of the primary tumor must undergo epithelial-to-mesenchymal transition in order to invade the bloodstream. Following intravasation, these metastatic cells are exposed to stress factors like matrix detachment, shear forces and cells of the immune system [150,151]. Thus, the circulating tumor cells form emboli by interaction with blood platelets [152]. As described above, the discontinuous endothelium of sinusoids facilitates mesenchymal-to-epithelial transition of circulating tumor cells e.g. into the bone. Furthermore, gradients of cytokines contribute to the tissue distribution of metastatic cancer cells. It has been shown that C-X-C motif chemokine ligand 12 (CXCL12, also known as stromal cell-derived factor 1) plays a key role in metastasis direction of several carcinoma such as prostate cancer, brain tumors, leukemia, or breast cancer into other tissues. Each of these cancer types overexpress the G-protein coupled C-X-C chemokine receptor 4 (CXCR4) [153]. CXCR4 is involved in colonization of bone marrow by fetal hematopoietic stem cells and organogenesis during embryogenesis. In adults, CXCR4 controls the homing of bone marrow cells, is involved in signaling pathways for proliferation, migration, chemotaxis, and cell cycle control of immune cells and was identified as a co-receptor for HIV [154–156]. Following the CXCR4/CXCL12 axis, CXCR4 overexpressing metastatic cancer cells are guided towards highly CXCL12 expressing tissues like bone marrow, enabling metastatic homing [157,158].

Depending on the cancer type and secreted factors, bone metastases can act osteoclastic by increasing bone degradation, or osteoblastic characterized by abnormal bone formation [159,160]. BC metastases have been shown to act mostly osteolytic when reaching the bone niche by shifting the bone homeostasis towards degradation processes (Figure 3) [161]. Therefore, the tumor cells secrete PTH, leading to promotion of RANKL expression in osteoblasts and to RANK/RANKL-mediated maturation and activation of osteoclasts. In addition, pro-inflammatory cytokines secreted by the tumor cells such as tumor necrosis factor alpha (TNF-α) and several interleukins (IL) increase RANKL-expression on osteoblasts

and suppress the expression of osteoprotegerin (OPG), a molecule responsible for inhibition of osteoclast maturation [162]. Osteoclasts are known for secretion of miRNAs that can accelerating the tumor growth and angiogenesis by repression of tumor suppressors and apoptotic pathways [163–165]. The vascular adhesion molecule 1 (VCAM-1) expressed on BC cells leads to recruitment of osteoclast progenitor cells via the integrin α4β1, enhancing local osteoclast activity [166]. In contrast, the enhanced bone matrix degradation releases calcium and stored mitogenic factors like TGF-β promoting BC cell proliferation by increasing PTH secretion [167,168].

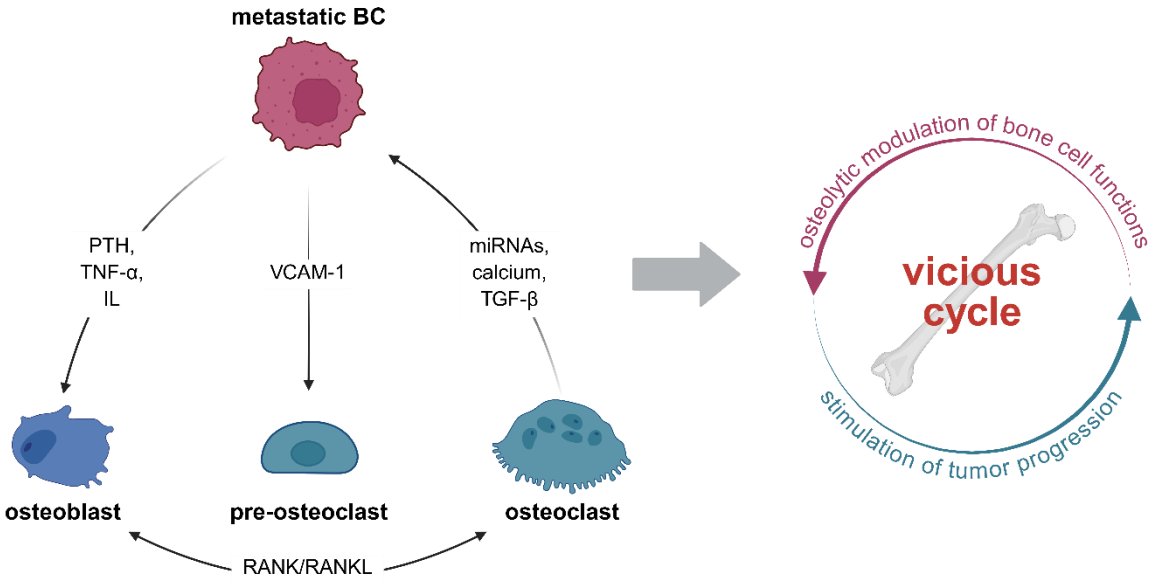


Figure 3: Factors in osteolytic modulation of bone-resident cells by breast cancer metastases. Breast carcinoma (BC) cells homing in the bone niche secrete the parathyroid hormone (PTH), tumor necrosis factor alpha (TNF-α) or interleukins (IL) stimulating the interaction of receptor activator of nuclear factor kappa-light-chain-enhancer of activated B-cells (RANK) on osteoclasts with its ligand (RANKL) secreted by osteoblasts. Furthermore, BC cells secrete the vascular adhesion molecule 1 (VCAM-1), leading to recruitment of pre-osteoclasts. Meanwhile, BC cells are further stimulated in growth and survival by microRNAs (miRNAs) secreted by osteoclasts inhibiting tumor suppressors and apoptotic pathways. Calcium and transforming growth factor beta (TGF-β) released from the degraded bone matrix also promotes BC proliferation. Graphic based on the sources [159–168]. Image created in BioRender (Stadler, N. (2026) https://BioRender.com/2d3wy61)

The disturbed bone homeostasis leads to several severe co-morbidities occurring in addition to the primary BC. Patients are prone to develop bone pain, hypercalcemia, spinal cord compression or pathological fractures due to the enhanced bone degradation, drastically diminishing their life quality [169]. In addition to the treatment of the primary BC (see section "*Breast cancer types and treatment options*") bone-targeting agents like bisphosphonates or denosumab are administered additionally for reduction of pain and

skeletal-related co-morbidities. Denosumab is a monoclonal antibody targeting and neutralizing RANKL and therefore affecting RANK/RANKL signaling pathways for osteoclast activation and maturation [170]. Bisphosphonates like zoledronic acid bind to calcified bone-matrix inhibiting interactions of osteoclasts with the bone. In addition, this nitrogen-containing bisphosphonate enters osteoclasts for inhibition of the farnesyl pyrophosphatase synthase, a key enzyme in post-translational modification of small GTPases essential for the osteoclast function, finally inducing apoptosis [171].

Multifunctional Nanocarrier for Counteract the Vicious Cycle

Biomolecule-based nanoparticles are a rising field for delivery of nucleic acids, peptides and proteins. For example, this technology has already been used to transport the p53 gene into breast cancer cells, siRNAs for gene silencing in different cell types or C3bot1 into lung cancer cells [172–174]. One prominent biomolecule used for the transport of cargos is avidin (Avi), a ~67 kDa homotetrameric glycoprotein. It derives from the egg white of oviparous species and binds up to four biotins with a very high affinity (K_D) of 10^{-15} M via specific, non-covalent interactions [175]. Biotin, or Vitamin H, is a small molecule (0.2 kDa) involved in biological processes like cell growth and the citric acid cycle [176]. The Avi/biotin complexation is stable over a wide range of pH and temperature, as well as in organic solvents [177,178]. Since biotin is quite small, biotinylation of the cargo does not significantly alter its biological activity, making Avi/biotin an optimal platform for drug delivery.

However, Avi has shown a high tendency to nonspecific binding due to its oligosaccharide content and basic isoelectric point [179]. In addition, anti-Avi antibodies are common in the general population due to Avi-containing vaccines or diet exposure. However, an antibody response upon Avi treatment of mice or human gave no evidence of vital sign alteration [180–183]. Nevertheless, there are approaches to improve the Avi/biotin system. Neutravidin is a deglycosylated analogue of Avi with increased specificity and a lower isoelectric point, preventing non-specific binding to cell surfaces and proteins [184]. Alternative biotin-binding proteins from other sources like streptavidin from *Streptomyces avidinii* or bradavidin II from *Bradyrhizobium japonicum* are also established derivatives with high affinity to biotin and fewer non-specific binding properties [185,186].

In this thesis, a novel modular Avi/biotin-based nanocarrier combining effectors for selective downregulation of breast cancer metastases and inhibition of overacting osteoclasts in the metastatic bone niche is evaluated (Figure 4).

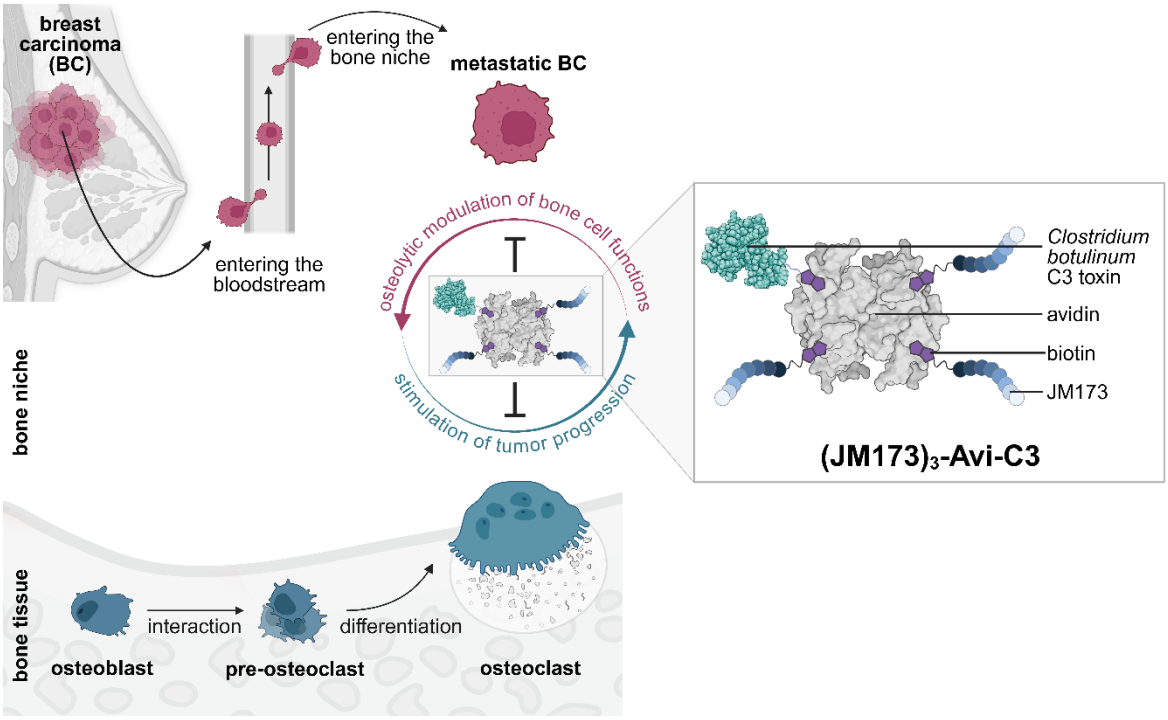


Figure 4: Schematic illustration of BC bone metastasis and the structure of the $(JM173)_3$-Avi-C3 multifunctional nanocarrier to counteract the vicious cycle. Metastatic BC cells can reach the bone niche via the bloodstream, inducing a vicious cycle of osteolysis and tumor progression [160]. The nanocarrier $(JM173)_3$-Avi-C3 is designed to target overacting osteoclasts as well as metastatic BC cells. Therefore, one entity of Clostridium botulinum C3 toxin and three entities of the CXCR4 antagonist JM173 are labelled with biotin for assembly on a central avidin platform. Figure design inspired by [187]. Image created in BioRender (Stadler, N. (2026) https://BioRender.com/4pbddcd).

It has already been shown, that the C3 toxin specifically targets monocyte-derived osteoclast-like cells inhibiting maturation and resorption activity [64]. This characteristic can be used to interfere with the vicious cycle by inhibiting the osteolytic modulation of bone-residual osteoclasts. To assemble *Clostridium botulinum* C3bot1 toxin on the nanocarrier, C3bot1 harboring an N-terminal cysteine residue (^{Cys}C3bot1, short ^{Cys}C3) was biotinylated via a pH-sensitive hydrazone linker (B-C3) enabling binding to Avi and cellular toxin release from the acidic endosomes into the cytosol (Figure 5a) [187].

To simultaneously target the metastatic BC cells, the small peptide JM173 was included by biotinylation via a stable polyethylene glycol linker (B-JM173) (Figure 5b) [187]. JM173 is composed of the first seven amino acid residues of the endogenous peptide inhibitor of CXCR4 (EPI-X4) which derives from human serum albumin (HSA). JM173 represents the N-

terminus of HSA that is responsible for the binding to CXCR4, a receptor that is highly overexpressed on metastatic breast cancer cells [158,188]. Compared to EPI-X4, the N-terminus of JM173 was modified via introduction of D-leucine and the C-terminus was truncated to increase plasma stability, resulting in the peptide (d-I)LRWSRK-NH_2 in one letter amino acid code. JM173 has been shown to act as a CXCR4 antagonist upon binding, leading to an inhibition of CXCL-12 mediated signaling pathways and migration. Additionally, CXCR4-tropic HIV-1 infection was inhibited by JM173, since CXCR4 represents one of the major co-receptors of HIV-1 [188].

It is hypothesized, that by assembling one moiety of B-C3 and three moieties of B-JM173 on an Avi platform (Figure 5c), C3 can not only target the overacting osteoclasts, but can also be taken up into non-monocytic breast cancer cells due to the forced cellular proximity by JM173 binding to CXCR4. This could potentially inhibit actin-dependent metastatic processes like migration and proliferation of the metastatic breast cancer cells. In this scenario, C3 toxin has a dual function of directing the nanocarrier into the osteoclasts and intoxication of osteoclasts as well as BC cells homed to the bone tissue. This makes the nanocarrier $(JM173)_3$-Avi-C3 a promising approach to target common co-morbidities in late-stage breast carcinoma.

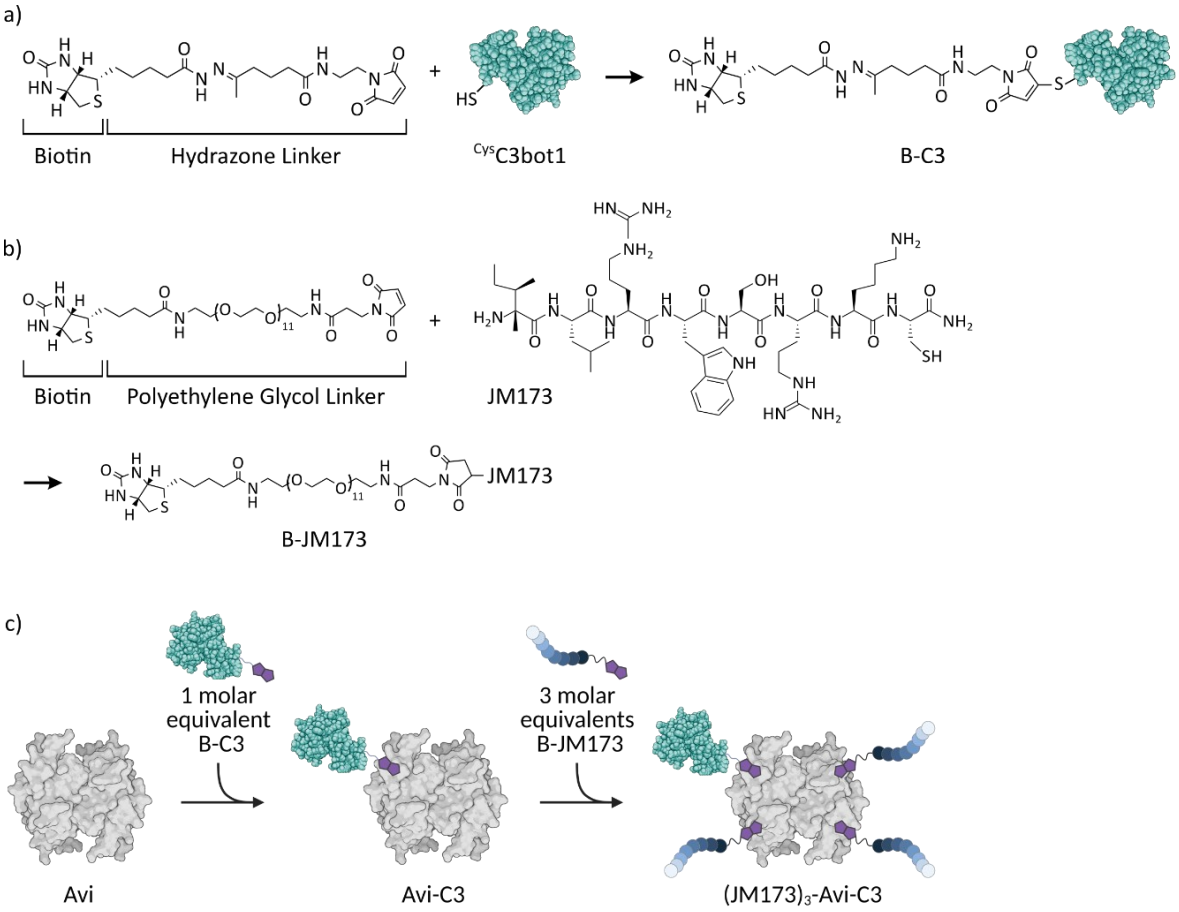


Figure 5: Biotinylation of CysC3bot1 and JM173 and assembly on the avidin platform. ***(a)*** *Mono-biotinylation of CysC3beot1 by using a bifunctional biotin-maleimide conjugate with a pH-sensitive hydrazone linker. The reaction was performed for 3 h at room temperature (RT) in 25 mM HEPES buffer in presence of Tris(2-carboxyethyl)phosphine (TCEP), resulting in biotinylated C3 toxin (B-C3).* ***(b)*** *Mono-biotinylation of the peptide JM173 (compound No. 27 in [188]) by using a bifunctional biotin-maleimide conjugate with a stable polyethylene glycol linker. The reaction was performed overnight (O.N.) at RT in 50 mM phosphate buffer in presence of TCEP, resulting in biotinylated JM173 peptide (B-JM173).* ***(c)*** *Scheme of the assembly of B-C3 and B-JM173 on an avidin platform in a stoichiometric molar ratio of 1:3:1 in a two-step reaction. The Avi-binding biotin is displayed in purple. Chemical structures are created with ChemDraw 23.1.2, the crystal structure of C3 toxin originates from PDB entry 1G24 [30]. Figure modified from [187], published with CC BY 4.0 license (https://creativecommons.org/licenses/by/4.0/), DOI: 10.3390/jfb16110399.*

1.3.2 $C3_{E174Q}$: Cell Type-Selective Delivery System for Targeted Gene Modulation

In contrast to the nanocarrier $(JM173)_3$-Avi-C3, where C3 is used as an enzymatically active cargo for inhibition of Rho in breast cancer cells and osteoclasts, this part of the thesis focuses on the catalytically inactive mutant $C3_{E174Q}$. As described before, the cell type-selective uptake of $C3_{E174Q}$ into monocyte-derived cells is not affected by the point mutation responsible for the lack of ADP-ribosylation activity. This makes $C3_{E174Q}$ a promising monocyte-selective cargo transport system. Indeed, the mutant $C3_{E174Q}$ has been used before to successfully transport several peptides and proteins specifically into

monocyte-derived cells [62,68,87,90,91]. In this thesis, $C3_{E174Q}$ from *Clostridium botulinum* was genetically fused to Cas9 to achieve monocyte-selective transport of the genome editing tool.

The CRISPR/Cas System

Clustered regulatory-interspaced short palindromic repeat (CRISPR) Cas (CRISPR associated) proteins originate from prokaryotes, where they were discovered as part of the adaptive immune system [189–191]. Upon contact with foreign genetic material e.g. by viral infection, this DNA is integrated as short sequences into the host genome as so called "spacers". These spacers are separated by short repetitive sequences, forming the CRISPR array [192]. While the CRIPSR arrays in bacteria and archaea were discovered in the late 1980s and early 1990s, the corresponding Cas nucleases were first described over a decade later [189,193–195]. The actual function of the CRISPR/Cas system as an adaptive immune system was finally disclosed in 2007. However, additional components of the system were discovered later, e.g. different small RNAs were discovered in 2011 [191,196]. To this date, six major types of CRISPR/Cas systems with several subtypes have been described that differ particularly in the functions and number of encoded Cas enzymes.

Type I CRISPR/Cas systems all encode for Cas3, a helicase unwinding DNA-DNA- and RNA-DNA duplexes with a reported endo- or exonuclease activity [197–199]. On the same operon are additional Cas enzymes encoded depending on the system subtype, all harboring different enzyme activities. These Cas enzymes are assembled into an effector complex for recognition and cleavage of foreign DNA [200]. Type III and type IV CRISPR/Cas systems also form multiprotein effector complexes, however, compared to type I these comprise different Cas enzymes and effectors. While type III is characterized by Cas10 expression, type IV is defined by the presence of the *csf1* gene, encoding for a highly reduced large subunit of the type IV effector complex [201–203]. Type II, type V and type VI CRISPR/Cas systems encode for the multidomain proteins Cas9, Cas12 or Cas3, respectively. These systems have in common that all functions of the effector complexes are combined in one enzyme [201,204].

When a type II system CRISPR array is translated into precursor CRISPR RNA (pre-crRNA), it is recognized by a small trans-acting CRISPR RNA (tracrRNA) that is partially complementary to the repetitive sequences in the transcript. Pre-crRNA and tracrRNA form an RNA duplex,

where the tracrRNA leads to recruitment and binding of Cas9. This formation of pre-crRNA with multiple bound tracrRNAs and Cas9 is cleaved by the endonuclease RNase III, forming single ribonucleoprotein (RNP) complexes consisting of Cas9 and CRISPR RNA (crRNA) [196,205]. If the prokaryotic cell is re-infected by the same virus, the Cas9-crRNA RNP complex recognizes protospacer adjacent motifs (PAMs) in the viral genome. This induces sequence-directed crRNA binding to the foreign DNA and Cas9-mediated DNA cleavage to prevent re-infection (Figure 6a) [191].

CRISPR/Cas9 as Genome Editing Tool

In 2012, first attempts to transfer the type II CRISPR/Cas9 system into mammalian cells for genome engineering were reported. Thereby, also the chimeric synthetic single guide RNA (sgRNA), a fusion of crRNA and tracrRNA, combining the properties of the original RNAs was introduced [204]. These discoveries paved the way for first *in vivo* applications of this genetic scissors and finally resulted in a Nobel Prize in Chemistry in 2020 [206,207]. The genome engineering approach not only makes use of the prokaryotic CRISPR/Cas9 system, but also of the eucaryotic DNA repair mechanisms. Upon DNA lesions, the cell can activate two major double-strand break repair mechanisms, namely non-homologous end joining (NHEJ) and homology-directed repair (HDR) (Figure 6b). HDR is a very precise repair pathway, since it utilizes the sister chromatid as template for DNA repair. In genome engineering, a donor template with homologous sequences can also be recognized by the stabilizing 3' filament on the broken DNA strand and be used as a starting point for HDR-based editing. Therefore, DNA sequences can be inserted at a specific genomic locus, disrupting host genes or bringing in new genetic information [208,209]. While HDR can only take place during the DNA replication (S) phase or the Second Gap (G_2) phase of the cell cycle, NHEJ is the more commonly used cellular DNA repair mechanism as it is employed during any cell cycle phase except mitosis [210,211]. NHEJ shows mechanistic flexibility in reparation of DNA lesions, since it can start from either end of the broken DNA stands. In addition, the enzymes involved, like nucleases, polymerases and ligases, can differ for each joining event, contributing to a flexible and fast repair mechanism. In contrast to HDR, no template for correction is used in NHEJ, leading to insertion and/or deletion (indel) events during DNA repair with an error rate far higher than HDR. These indels can cause frame shifts in a coding exon, making NHEJ an error-prone cellular mechanism, which can be hijacked for knockout approaches upon CRISPR/Cas9 treatment [212–214].

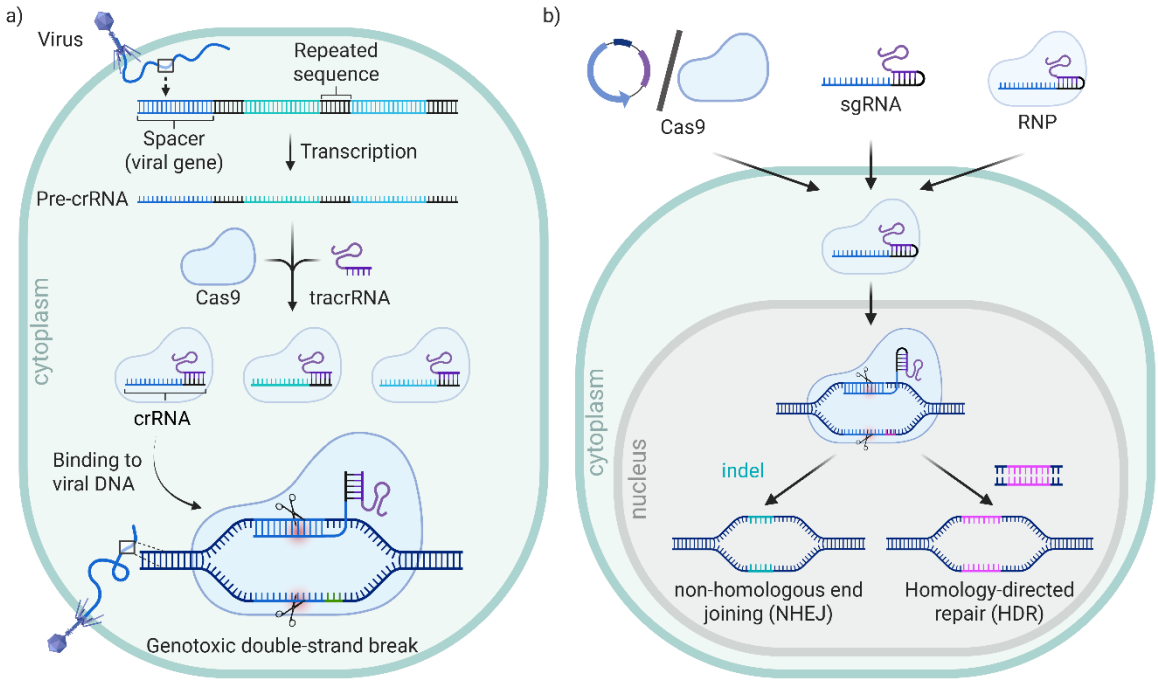


Figure 6: Schematic illustration of the CRISPR/Cas9 system as prokaryotic adaptive immune system and as genome editing tool. ***(a)*** *Upon viral infection, prokaryotic cells harboring a type II CRISPR/Cas (Clustered regulatory-interspaced short palindromic repeat/CRISPR associated) system, integrate gene fragments of the virus into the CRISPR array, separated by short repetitive sequences. The transcript of this CRISPR array, so called precursor CRISPR RNA (pre-crRNA), forms an RNA-duplex with the small trans-acting crRNA (tracrRNA), and interacts with Cas9. The pre-crRNA is cut by RNase III to form ribonucleoprotein (RNP) complexes of Cas9 and crRNA that binds complementary viral DNA in a secondary infection, leading to a genotoxic double strand break.* ***(b)*** *In genome engineering, the double strand break caused by the nuclear RNP complex can lead to indel mutations (insertion or deletions) and therefore gene knockouts caused by the error-prone cellular repair mechanism non-homologous end joining (NHEJ). If a donor template is present, error-free insertion of this DNA fragment by cellular homology-directed repair (HDR) can be accomplished. To achieve genome editing, Cas9 needs to be introduced into the cell as protein, plasmid encoded or as RNP complex. If not transported via an RNP complex, the synthetic gene targeting single guide RNA (sgRNA) combining crRNA and tracrRNA in a single molecule, needs to be introduced into the cell as well. Created in BioRender: Stadler, N. (2026) https://BioRender.com/0o19pqu (Adapted from "Streptococcus' Adaptive Immune System against Viruses: CRISPR-Cas9"; Cress, B. (2025); Retrieved from https://app.biorender.com/biorender-templates).*

Over the past decade, several CRISPR/Cas9 applications for disease modeling or gene therapy were reported. One major field is the modeling of neurodegenerative diseases like Alzheimer's disease, Parkinson's disease or Huntington's disease in animals. All these conditions share the characteristics of neuronal degeneration, that could be accurately displayed in phenotypes of animals by CRISPR/Cas induced mutations in key regulator genes of each disease [215–218]. This also accounts for other fields like cardiovascular diseases, autoimmune-related diseases or cancer research, where improved animal models created by CRISPR/Cas technology promote understanding and combating these diseases

[219–221]. Recently, the United States Food and Drug Administration (FDA) approved CASGEVY® as the first CRISPR/Cas9 gene therapy for patients with sickle cell disease, a hemoglobinopathy characterized by abnormal hemoglobin polymerization [222].

Nevertheless, CRISPR/Cas9 off-target effects caused by unintended Cas9- or sgRNA binding are considered as a significant risk for its application in *in vivo* gene therapy [223,224]. This risk cannot only be diminished by improvement of Cas9 or sgRNA variants, but also by increasing cell type-selectivity of the CRISPR/Cas9 delivery system towards human cells, which are responsible for the disease.

CRISPR/Cas9 Vehicles for Delivery of Cas9 into Monocytic Cells

For gene editing via the CRISPR/Cas9 system, Cas9 and the gene-targeting sgRNA need to be efficiently introduced into the cytosol and/or nucleus of the cell and form an RNP complex. Therefore, several vehicles for the transport of RNP complexes, plasmid-based CRISPR/Cas9 components or Cas9 mRNA together with sgRNA have been established to overcome tissue and cell membrane barriers [225]. Physical delivery methods cause host cellular and nuclear membrane disruption to facilitate the internalization of CRISPR/Cas9 components. Microinjection has already been efficiently used for germline editing in zebrafish to deliver RNPs, plasmid DNA or mRNA into the cell [226]. Electroporation is an alternative method using electric fields for delivery of macromolecules into cells via transient pores in the cell membrane with high transfection efficiency *ex vivo* or *in vitro*. A method where the CRISPR/Cas components are applied systemically is hydrodynamic injection. Therefore, large injection volumes of the components are applied into the blood stream under high pressure. The reflux of the high fluid volume leads to a transient expansion of the liver, creating temporary pores in hepatocytes for delivery of CRISPR/Cas components [227,228]. Physical methods are easy to apply but lack in scalability, tissue or cell type selectivity and cause potential cellular damage [225].

Different types of viral vectors inherently provide efficient mechanisms to infiltrate cells and introduce genetic material. Adenoviruses and adeno-associated viruses (AAVs) can transfer genetic material into various cell types with high transduction efficiency [229,230]. To improve tissue selectivity and avoid immune detection, capsid modifications were introduced e.g. allowing specifical gene editing in neural tissues of mice in a pre-clinical model [231,232]. Lentiviral vectors are commonly used for *ex vivo* gene editing in

hematopoietic stem cells, since the CRISPR/Cas components can be stably integrated into the host genome [233].

As an alternative, non-viral vectors with lower immunogenicity and reduced risk of adverse effects (i.e. by genomic integration) were designed. One of these vectors are lipid-based nanoparticles composed of spheroids with ionizable cationic lipids, phospholipids, pegylated lipids and cholesterol to stably encapsulate mRNA or RNP complexes. Since lipid compounds tend to accumulate in the liver, tissue selectivity was improved by introducing specialized lipids targeting the tissue of interest [234,235]. Several other carriers in the nanoparticle range have been developed to increase specificity and efficiency of CRISPR/Cas9 component transport. Peptide-based nanoparticles were developed for CRISPR/Cas9 delivery, allowing the incorporation of targeting ligands or imaging probes for extrahepatic delivery [236]. Natural or synthetic polymer carriers have been established for controlled release of CRISPR/Cas9 components e.g. targeting the cyclin-dependent kinase 11 expression in MCF7 breast cancer cells [237]. Recently, lipid-based vehicles from retrovirus-like structures have been developed for RNP complex delivery showing an increased number of delivered Cas9 proteins compared to classical viral vectors [238]. Therefore, non-viral vector systems represent alternative hybrid platforms with lowered safety concerns compared to viral delivery.

Nuclear Translocation and DNA Binding of Cas9

While some specialized forms of electroporation, e.g. nucleofection lead to transfection of CRISPR/Cas9 components directly into the nucleus, other delivery methods only reach the cytosol [239,240]. In this case, a short peptide called nuclear localization sequence (NLS) fused to Cas9 directs its transport from the cytosol into the nucleus. NLS signals were first discovered in viruses, activating host importin subunits responsible for nuclear translocation [241,242]. However, there are hints that the Cas9 protein can enter nuclei even without NLS sequences by hitchhiking endogenous nuclear proteins facilitating the uptake [243]. Once translocated into the nucleus, Cas9 can bind to sgRNA-directed target genes for cleavage. An essential requirement for Cas9 positioning on host DNA is the presence of a protospacer adjacent motif (PAM). The sequence of this motif varies between Cas9 proteins from different origins, e.g. Cas9 isolated from *Streptococcus pyogenes* (SpCas9) recognizes the sequence NGG (any nucleotide (N) followed by two guanines (G)). It has been shown that this sequence occurs on average in only every 16th genomic locus,

limiting the targets for CRISPR/Cas9 applications to around 1,200 genes out of ~20,000 protein-coding genes. Therefore, other CRISPR nucleases have been synthesized e.g. by phage-assisted continuous evolution to expand PAM compatibility. Resulting Cas9 variants outperformed wildtype SpCas9 not only in PAM compatibility but also in DNA specificity by reducing off-target activity [244].

$C3_{E174Q}$ as Cell Type-Selective Transport System for CRISPR/Cas9 Components

By exploiting the monocyte-selective properties of the *Clostridium botulinum* C3 toxin, this thesis aimed to use the catalytically inactive mutant $C3_{E174Q}$ as cell-type specific transport system for CRISPR/Cas9 components [62]. Therefore, $C3_{E174Q}$ was C-terminally fused to SpCas9 by a repetitive glycine-serin-linker (GSGSG in one letter amino acid code). SpCas9 harbors a C-terminal NLS sequence, followed by a hexahistidine (6x His) tag for purification of the resulting fusion protein $C3_{E174Q}$_$SpCas9^{NLS\text{-}His}$, in the following called $C3_{E174Q}$_Cas9 (Figure 7a/b).

It is hypothesized that $C3_{E174Q}$_Cas9 can enter monocytic cells via the $C3_{E174Q}$-dependent uptake route. Nevertheless, for a functional CRISPR/Cas9 gene editing setup also the sgRNA targeting the gene of interest has to be introduced into the cell. This could either be achieved by previous introduction of the sgRNA e.g. by physical methods like electroporation, or by *in vitro* formation of an RNP complex before cellular treatment. The cytosolic RNP-complex should then be translocated into the nucleus to induce a gene knockout (Figure 7c).

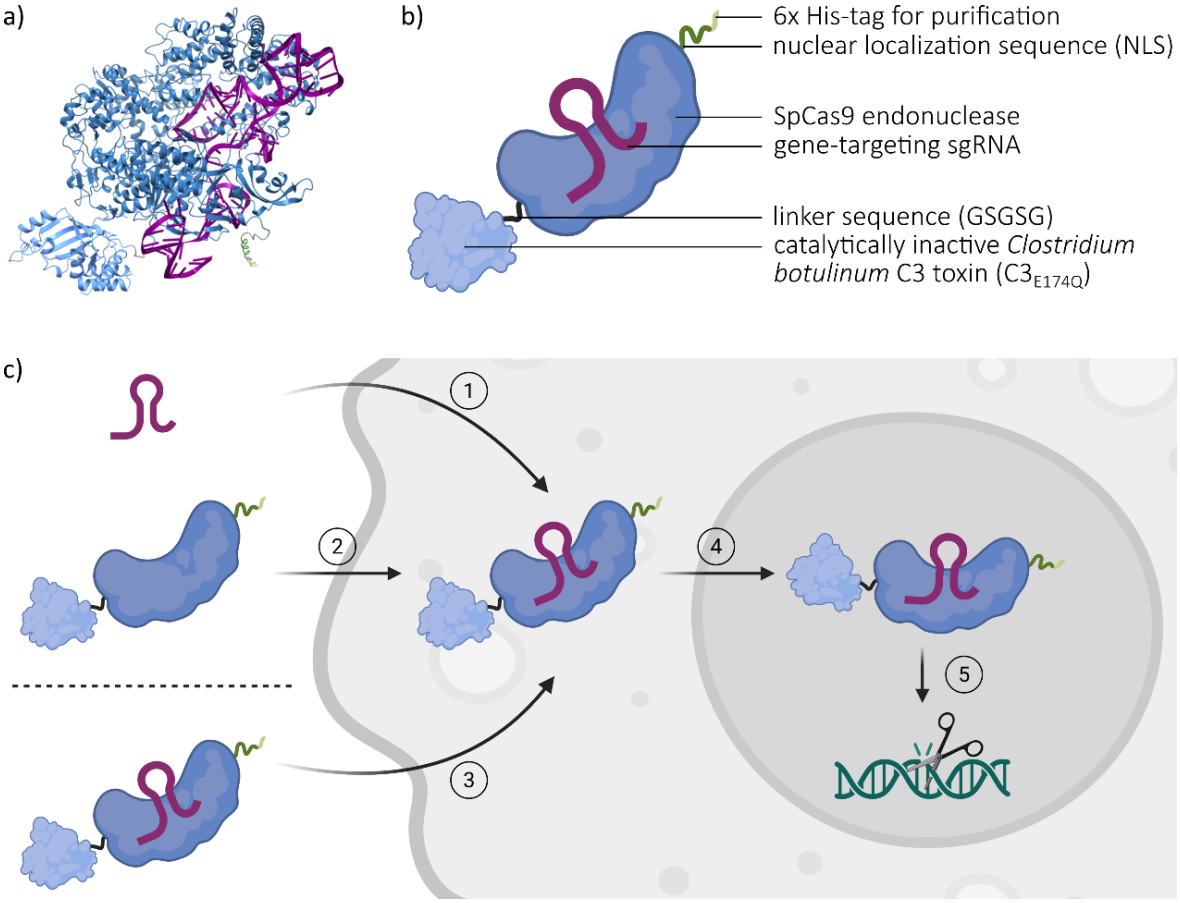


Figure 7: Schematic illustration of $C3_{E174Q}$_Cas9 structure and uptake route. ***a)*** *In silico prediction of $C3_{E174Q}$_Cas9:sgRNA complex structure using AlphaFold ([245], https://creativecommons.org/licenses/by/4.0/) with the catalytically inactive Clostridium botulinum C3 toxin ($C3_{E174Q}$) in light blue, Streptococcus pyogenes Cas9 (SpCas9) in dark blue, gene-targeting single guide RNA (sgRNA) in purple and the C-terminal nuclear localization sequence (NLS) with the hexahistidine (6x His) tag for purification in green.* ***b)*** *Schematic illustration of the $C3_{E174Q}$_Cas9:sgRNA complex depicted in a) including the linker sequence between $C3_{E174Q}$ and SpCas9.* ***c)*** *Schematic illustration of $C3_{E174Q}$_Cas9 uptake with and without bound sgRNA. $C3_{E174Q}$_Cas9 and $C3_{E174Q}$_Cas9:sgRNA are internalized into the cytosol of monocytic cells by the uptake route of C3 toxin (2, 3), while the sgRNA either can be introduced together with $C3_{E174Q}$_Cas9 as RNP complex (3) or by physical methods like electroporation (1). Once assembled to $C3_{E174Q}$_Cas9:sgRNA, NLS-dependent translocation of the RNP complex into the nucleus (4) occurs, leading to sgRNA-guided cleavage of the gene of interest (5). b) and c) were created in BioRender (Stadler, N. (2026) https://BioRender.com/i2crw0g).*

$C3_{E174Q}$_Cas9 in Gene Therapy for Monocyte-Associated Diseases

There is a wide range of disorders associated with specialized monocytic cells of myeloid clusters as primary drivers of diseases [246]. Monocytes are developed from bone marrow progenitor cells by sequential differentiation of hematopoietic stem cells [247]. They circulate through the body and are able to differentiate into macrophages or dendritic cells when infiltrating inflamed organs. These specialized cells form an important part of the innate immune system by maintaining tissue homeostasis e.g. by inducing repair mechanisms upon damage or recruiting of and interacting with T-cells to challenge

infections [248]. If those macrophages tip from their protective function to immunopathology, chronic inflammatory processes are induced that are associated with diseases like atherosclerosis, obesity, diabetes, fibrosis, chronic obstructive pulmonary disease or cancer [246]. By modifying disease-related genes e.g. responsible for cytokine production or recognition, hyperinflammatory responses could be diminished.

For gene editing in human primary myeloid cells, the CRISPR/Cas9 system has already been established. Therefore, RNP complexes or plasmid-encoded Cas9 and sgRNA were introduced *ex vivo* by nucleofection or nanoparticles [249,250]. However, since monocytes have a high activity of innate nucleases, efficient mRNA or plasmid transfections are difficult but can be performed by adding RNase inhibitors [251]. On the other hand, nucleofection has a negative impact on cell viability or leads to unintended activation of primary monocytes [250]. $C3_{E174Q}$_Cas9 offers the possibility for a $C3_{E174Q}$-dependent monocyte-selective delivery of CRISPR/Cas9 components without these adverse effects. This makes $C3_{E174Q}$_Cas9 a promising gene editing tool not only for *ex vivo* treatments, but also for targeted *in vivo* applications in inflammatory monocyte-mediated diseases.

1.4 Aim of the Thesis

Bacterial toxins have evolved to target essential cellular processes with highest specificity and efficiency, often acting at extremely low concentrations in the cytosol of target cells. This natural potency makes them powerful pharmacological tools for developing innovative research strategies and therapies. This thesis aims to exploit the *Clostridium botulinum* C3 toxin not only for the targeted down-modulation of metastatic breast cancer growth and osteolysis in the bone niche but also as delivery system to generate a monocyte-selective gene editing tool.

In the first part of this thesis, functionalized C3 toxin and CXCR4 antagonist JM173 were assembled on an avidin scaffold to specifically target breast cancer metastases within the bone microenvironment. The resulting supramolecular nanocarrier $(JM173)_3$-Avi-C3 and its single components were tested for their functionality and toxicity in cell culture models and zebrafish embryos. Afterwards, CXCR4 expressing cell lines were examined for their selective binding of JM173-containing constructs via flow cytometry. The uptake of $(JM173)_3$-Avi-C3 into these cells was verified by fluorescence microscopy and biochemically by sequential ADP-ribosylation of Rho. Finally, the effect of $(JM173)_3$-Avi-C3 on breast cancer cell growth, as well as on osteoclast differentiation and resorption activity was investigated *in vitro* to assess the potential of $(JM173)_3$-Avi-C3 to disrupt the vicious cycle between tumor progression and osteolysis.

Despite the growing number of therapeutic peptides and proteins, delivering them efficiently into the cytosol of target cells remains difficult, because these molecules do not cross membranes. Therefore, in the second part of this thesis, a C3 toxin-based monocyte-selective transport system for the gene editing enzyme Cas9 was developed. Hence, C3 or its non-toxic variant $C3_{E174Q}$ were genetically fused to *Streptococcus pyogenes* Cas9. The fusion proteins C3_Cas9 and $C3_{E174Q}$_Cas9 were tested for their ability to enter the cytosol and nucleus of monocytic cells as well as for the DNA cleavage activity of Cas9. Finally, different concepts to establish a proof-of-concept knockout model were tested, including the knockout of reporter genes, receptors, or cell surface markers of monocytic cells.

2 Material and Methods

2.1 Material

2.1.1 Chemicals

Table 1: List of used chemicals and corresponding manufacturers

Chemical	**Manufacturer**
Acrylamide/bis 30 % (Rotiphorese®)	Carl Roth GmbH & Co. KG, Karlsruhe, GER
Agar-agar	SERVA Electrophoresis GmbH, Heidelberg, GER
Agarose, universal – peqGOLD	VWR Chemicals, Radnor, PA, USA
Albumin fraction V (BSA)	Carl Roth GmbH & Co. KG, Karlsruhe, GER
Ammonium persulfate (APS)	SERVA Electrophoresis GmbH, Heidelberg, GER
Ampicillin sodium salt	Carl Roth GmbH & Co. KG, Karlsruhe, GER
Benzamidine-Sepharose 6B	GE Healthcare, Chicago, GER
Bromphenol blue	Carl Roth GmbH & Co. KG, Karlsruhe, GER
Coomassie brilliant blue R250	SERVA Electrophoresis GmbH, Heidelberg, GER
Deoxynucleotide (dNTP) solution mix	New England Biolabs, Ipswich, MA, USA
Dimethyl sulfoxide (DMSO)	Carl Roth GmbH & Co. KG, Karlsruhe, GER
Dithiothreitol (DTT)	Merck KGaA, Darmstadt, GER
DyLight 488 NHS ester	Thermo Fisher Scientific Inc., Waltham, MA, USA
Ethylenediaminetetraacetic acid (EDTA)	Merck KGaA, Darmstadt, GER
Fetal calf serum (FCS)	Thermo Fisher Scientific Inc., Waltham, MA, USA
Fluorescein-NAD^+	Bio-Techne, Minneapolis, MN, USA
Glacial acetic acid	VWR Chemicals, Radnor, PA, USA
Glucose	Carl Roth GmbH & Co. KG, Karlsruhe, GER
Glutathione agarose 4B-beads (Protino)	Macherey-Nagel GmbH & Co.KG, Düren, GER
Glycerol	Sigma-Aldrich corp., St. Louis, MO, USA

Chemical	**Manufacturer**
Glycine	Sigma-Aldrich corp., St. Louis, MO, USA
HEPES solution (1 M)	Thermo Fisher Scientific Inc., Waltham, MA, USA
Hoechst33342	Thermo Fisher Scientific Inc., Waltham, MA, USA
Imidazole	Carl Roth GmbH & Co. KG, Karlsruhe, GER
Immobilon® Western HRP substrate	Merck KGaA, Darmstadt, GER
Isopropyl β-D-1-thiogalactopyranoside (IPTG)	Carl Roth GmbH & Co. KG, Karlsruhe, GER
Kanamycin sulfate	Carl Roth GmbH & Co. KG, Karlsruhe, GER
L-Glutamine (200 mM)	Thermo Fisher Scientific Inc., Waltham, MA, USA
Magnesium chloride ($MgCl_2$)	Carl Roth GmbH & Co. KG, Karlsruhe, GER
MEM non-essential amino acid solution (100x)	Thermo Fisher Scientific Inc., Waltham, MA, USA
Methanol	VWR Chemicals, Radnor, PA, USA
Midori Green Direct	NIPPON Genetics EUROPE, Düren, GER
Nuclease-free water	New England Biolabs, Ipswich, MA, USA
Penicillin-Streptomycin (Pen/Strep, 5000 U/ml)	Thermo Fisher Scientific Inc., Waltham, MA, USA
Perfluoroalkoxy alkanes (PFA)	Merck KGaA, Darmstadt, GER
Phenylmethylsulfonyl fluoride (PMSF)	Sigma-Aldrich corp., St. Louis, MO, USA
phorbol 12-myristate 13-acetate (PMA)	Merck KGaA, Darmstadt, GER
Potassium chloride (KCl)	Merck KGaA, Darmstadt, GER
Potassium dihydrogen phosphate (KH_2PO_4)	Merck KGaA, Darmstadt, GER
PriGow II Medium	Applied Biological Materials Inc., Richmond, CAN
PureCube 100 INDIGO Ni-agarose	Cube Biotech GmbH, Monheim, GER
Puromycin (10 mg/ml solution, sterile)	InvivoGen, San Diego, CA, USA

Chemical	**Manufacturer**
Roswell Park Memorial Institute (RPMI) 1640 Medium	Thermo Fisher Scientific Inc., Waltham, MA, USA
SiR-actin	Spirochrome, Thurgau, CHE
Skimmed milk powder	AppliChem GmbH, Darmstadt, GER
Sodium azide	Carl Roth GmbH & Co. KG, Karlsruhe, GER
Sodium chloride (NaCl)	Merck KGaA, Darmstadt, GER
Sodium dihydrogen phosphate (NaH_2PO_4)	Merck KGaA, Darmstadt, GER
Sodium dodecyl sulfate (SDS)	Carl Roth GmbH & Co. KG, Karlsruhe, GER
Sodium hydrogen phosphate (Na_2HPO_4)	Merck KGaA, Darmstadt, GER
Sodium pyruvate (100 mM)	Thermo Fisher Scientific Inc., Waltham, MA, USA
SYTOX™ Green Ready Flow™ Reagent	Thermo Fisher Scientific Inc., Waltham, MA, USA
Tetramethylethylenediamine (TEMED)	AppliChem GmbH, Darmstad, GER
Tris(hydroxymethyl)aminomethane (Tris-HCl)	Sigma-Aldrich corp., St. Louis, MO, USA
Triton® X-100	Carl Roth GmbH & Co. KG, Karlsruhe, GER
Trypsin-EDTA (0.25% / 0.02%)	PAN-Biotech GmbH, Aidenbach, GER
Tryptone	Becton Dickinson and Company, Franklin Lakes, NJ, USA
Tween®20	Merck KGaA, Darmstadt, GER
Yeast-Extract	SERVA Electrophoresis GmbH, Heidelberg, GER

2.1.2 Consumables and Kits

Table 2: List of used consumables and kits

Consumable or Kit	Manufacturer
24-well tissue culture test plate	Techno Plastic Products AG, Trasadingen, CHE
Amersham™ ProtanTM 0.45 µm nitrocellulose blotting membrane	GE Healthcare Life Sciences, Chicago, IL, USA
Batch column PureCube 1-step batch Midi Plus	Cube Biotech GmbH, Monheim, GER
Blotting paper MN 827 B	Marchery-Nagel GmbH & Co. KG, Düren, GER
Cell scraper	Sarstedt AG & Co., Nümbrecht, GER
CellTiter 96® AQ_{ueous} One Solution	Promega Corporation, Madison, WI, USA
DNA SmartLadder (200 bp – 10 kbp)	Eurogentec, Seraing, BEL
EnGen® sgRNA Synthesis Kit	New England Biolabs, Ipswich, MA, USA
FastGene® Gel/PCR Extraction Kit	Nippon Genetics Co., Ltd., JPN
FastGene® Gel/PCR Extraction Kit	NIPPON Genetics EUROPE, Düren, GER
Fow cytometer tube, 5 ml, PS	Sarstedt AG & Co., Nümbrecht, GER
GeneArt™ Genomic Cleavage Detection Kit	Thermo Fisher Scientific Inc., Waltham, MA, USA
Monarch® RNA Cleanup Kit	New England Biolabs, Ipswich, MA, USA
My-Budget Plasmid Mini Kit	Bio-Budget Technologies GmbH, Krefeld, GER
NEB buffer r3.1	New England Biolabs, Ipswich, MA, USA
Neubauer counting chamber	LO-Laboroptik GmbH, Friedrichsdorf, GER
Nuclear Extraction Kit	Abcam, Cambridge, UK
Petri dish 92x16 mm	Sarstedt AG & Co, Nümbrecht, GER
Pipette tips (0.1 – 1000 µl)	Sarstedt AG & Co., Nümbrecht, GER
PriCoat™ T25 Flasks	Applied Biological Materials Inc., Richmond, CAN
Reaction tube (0.2 ml, 0.5 ml, 1.5 ml, 2 ml)	Sarstedt AG & Co, Nümbrecht, GER
Reaction tube (1.5 ml, 2.0 ml)	Sarstedt AG & Co., Nümbrecht, GER

Consumable or Kit	Manufacturer
Serological pipettes (5-25 ml)	Sarstedt AG & Co, Nümbrecht, GER
Superdex™ 75 Increase 10/300 GL column	Cytiva, Marlborough, MA, USA
Syringe BD Plastipak™ (20 ml)	Becton Dickinson and Company, Franklin Lakes, NJ, USA
Syringe filter Filtropur S 0.2	Sarstedt AG & Co, Nümbrecht, GER
Syringe filter Filtropur S 0.45	Sarstedt AG & Co, Nümbrecht, GER
Tissue culture flask T25 and T75	Techno Plastic Products AG, Trasadingen, CHE
UV cuvette	Sarstedt AG & Co., Nümbrecht, GER
Vivaspin 20 centrifugal concentrator (MWCO 30 kDa)	Sartorius AG, Goettingen, GER
Vivaspin 500 centrifugal concentrator (MWCO 30 kDa)	Sartorius AG, Goettingen, GER
Zeba™ Spin Desalting Columns, 7K MWCO	Thermo Fisher Scientific Inc., Waltham, MA, USA
Zero Blunt™ PCR Cloning Kit	Thermo Fisher Scientific Inc., Waltham, MA, USA
ZymoPURE II Plasmid Midiprep	Zymo Research Europe GmbH, Freiburg, GER
µ-Slide 8 Well plate	Ibidi GmbH, Gräfelfing, GER

2.1.3 Devices

Table 3: List of used devices

Device	Manufacturer
ÄKTA pure™ protein purification system	Cytiva, Marlborough, MA, USA
BD FACSCelesta™ multicolor flow cytometer	Becton Dickinson and Company, Franklin Lakes, NJ, USA
Centrifuge 5415 D	eppendorf AG, Hamburg, GER
Centrifuge 5417 R	eppendorf AG, Hamburg, GER
Centrifuge 5810 R	eppendorf AG, Hamburg, GER

Device	Manufacturer
Centrifuge Avanti J26S XP	Beckman Coulter, Brea, CA, USA
Centrifuge J2-HS	Beckman Coulter, Brea, CA, USA
Double gel system Twin ExW S (PerfectBlue)	PEQLAB Biotechnologie GmbH, Erlangen, GER
Electrophoresis power supply – EPS 601	GE Healthcare Life Sciences, Chicago, IL, USA
EmulsiFlex-C3 homogenizer	Avestin Inc, Ottawa, CAN
iBright™ CL1500 imaging system	Thermo Fisher Scientific Inc., Waltham, MA, USA
Incubator CERTOMAT® BS-1	B. Braun Biotech International GmbH, Melsungen, GER
Incubator Heracell 240i	B. Braun Biotech International GmbH, Melsungen, GER
Keyence BZ-X810 fluorescence microscope with filter cubes DAPI, GFP, Cy5	Keyence Corporation, Osaka, JPN
Leica DMi1 phase-contrast microscope	Leica microsystems, Wetzlar, GER
Leica DMI6000 B microscope with DFC420 C camera	Leica microsystems, Wetzlar, GER
NanoDrop™ OneC	Thermo Fisher Scientific Inc., Waltham, MA, USA
PCR thermocycler TGRADIENT	Biometra GmbH, Gottingen, GER
pH-Meter ino Lab pH 720	WTW GmbH, Weilheim, GER
Rotor JA-10 fixed angle	Beckman Coulter, Brea, CA, USA
Rotor JA-20 fixed angle	Beckman Coulter, Brea, CA, USA
Safety cabinet HERAsafe	Heraeus Holding GmbH, Hanau, GER
Shaker (orbital) Unimax 2010	Heidolph Instruments GmbH & Co.KG, Schwabach, GER
Shaker (tilt) Doumax 1030	Heidolph Instruments GmbH & Co.KG, Schwabach, GER
Sonorex™ Digital DK 102 P sonificator	BANDELIN electronic GmbH & Co. KG, Berlin, GER

Device	Manufacturer
Spectra/Por®6 dialysis tube	Spectrum Laboratories Inc., Rancho Dominguez, CA, USA
ThermoMixer® C	eppendorf AG, Hamburg, GER
Tristar 2 LB 942 Multimode Microplate Reader	Berthold Technologies GmbH & Co. KG, Bad Wildbad, GER

2.1.4 Buffers and Solutions

Table 4: List of used aqueous buffers and solutions and their composition

Buffer/Solution	Component	Concentration
25 mM HEPES buffer	HEPES	25 mM
50 mM HEPES buffer	HEPES	50 mM
ADP-ribosylation buffer (pH 7.5)	Tris-HCl EDTA DTT $MgCl_2$ cOmplete protease inhibitor	20 mM 1 mM 1 mM 5 mM 1x
Agarose gel (1.5%)	Agarose TAE-buffer	1.5 g 100 ml
Coomassie destaining solution	Methanol Glacial acetic acid	45% (v/v) 10% (v/v)
Coomassie staining solution	Methanol Glacial acetic acid Coomassie brilliant blue R250	45% (v/v) 10% (v/v) 2.5% (w/v)
GST-protein lysis buffer (pH 7.4)	Tris-HCl NaCl Triton® X-100	10 mM 20 mM 1% (v/v)
GST-protein washing buffer (pH 7.4)	Tris-HCl NaCl	150 mM 20 mM

Buffer/Solution	Component	Concentration
Laemmli buffer (5-fold, pH 6.8)	Tris-HCl SDS Glycerol Bromophenol blue Dithiothreitol	0.3 M 10% 37.5% 0.4 mM 100 mM
NPI-20-buffer (pH 8.0)	NaH_2PO_4 NaCl Imidazole	50 mM 300 mM 20 mM
NPI-250-buffer (pH 8.0)	NaH_2PO_4 NaCl Imidazole	50 mM 300 mM 250 mM
Phosphate buffer (PB, pH 7.4)	Na_2HPO_4-Heptahydrate NaH_2PO_4-Monohydrate	37.7 mM 12.3 mM
Phosphate buffered saline (PBS, pH 6.8)	NaCl KCl Na_2HPO_4-Dihydrat KH_2PO_4	137 mM 2.7 mM 8 mM 1.8 mM
Phosphate buffered saline with Tween (PBS-T, pH 6.8)	NaCl KCl Na_2HPO_4-Dihydrat KH_2PO_4 Tween®20	137 mM 2.7 mM 8 mM 1.8 mM 0.1% (v/v)
SDS gel (20%)	SDS gel buffer SDS Acrylamide/Bisacrylamide APS TEMED	24.7% 0.1% 20% 0.1% 0.01%
SDS gel (8%)	SDS gel buffer SDS Acrylamide/Bisacrylamide APS TEMED	24.7% 0.1% 8% 0.1% 0.01%
SDS gel buffer (pH 8.8)	Tris-HCl	1.5 M

Buffer/Solution	Component	Concentration
SDS running buffer	SDS Tris-HCl Glycine	0.1% (w/v) 27.2 mM 192 mM
Towbin buffer	Glycine Tris-HCl Methanol	384 mM 54 mM 20% (v/v)
Tris-acetate-EDTA (TAE) buffer	Tris-acetate EDTA	40 mM 1 mM

2.1.5 Proteins, Enzymes, Toxins and Antibodies

Table 5: List of used proteins, enzymes and toxins

Proteins, Enzymes or Toxins	Manufacturer or Description
{d-ILE}LRWSRKC-NH_2 (JM173)	Kindly provided by Dr. Mirja Harms, Institute for Molecular Virology, University Ulm, GER
Biotinylated *Clostridium botulinum* C3bot1 toxin (B-C3), Dissolved in 25 mM HEPES buffer	Kindly provided by the research group of Prof. Dr. Tanja Weil, Max Planck Institute for Polymer Research, Mainz, GER
Biotinylated JM173 (B-JM173) Dissolved in 50 mM PB	Kindly provided by the research group of Prof. Dr. Tanja Weil, Max Planck Institute for Polymer Research, Mainz, GER
Bodipy-labelled avidin (^{BDP}Avi) Dissolved in 25 nM HEPES buffer	Kindly provided by the research group of Prof. Dr. Tanja Weil, Max Planck Institute for Polymer Research, Mainz, GER
Bovine serum albumin (Albumin Fraction V)	Carl Roth GmbH & Co. KG, Karlsruhe, GER
Cas9 nuclease, *S. pyogenes*	New England Biolabs, Ipswich, MA, USA
cOmplete™ protease inhibitor cocktail (50x)	F. Hoffmann-La Roche Ltd, Basel, CHE
PagerRuler™ pre-stained ladder	Thermo Fisher Scientific Inc., Waltham, MA, USA

Proteins, Enzymes or Toxins	**Manufacturer or Description**
Proteinase K	New England Biolabs, Ipswich, MA, USA
Recombinant C3bot1_Cas9$^{NLS\text{-}His}$	Expressed and purified during this thesis
Recombinant C3bot1$_{E174Q}$_Cas9$^{NLS\text{-}His}$	Expressed and purified during this thesis
Recombinant C3lim	Expressed and purified in the Institute of Experimental and Clinical Pharmacology, Toxicology and Pharmacology of Natural Products, University of Ulm, Medical Center, Ulm, GER
Recombinant ^{Cys}C3bot1	Expressed and purified during this thesis
Recombinant ^{His}Cas9$^{NLS\text{-}Cys}$	Expressed and purified in the Institute of Experimental and Clinical Pharmacology, Toxicology and Pharmacology of Natural Products, University of Ulm, Medical Center, Ulm, GER
Thrombin protease (GE27-0846-01)	Merck KGaA, Darmstadt, GER

Table 6: Antibodies and binding proteins used for Western Blot or flow cytometry

Antibody or Binding Protein	**Manufacturer or Description**
Anti-CD11b antibody, human, REAfinity, VioBlue	Miltenyi Biotec, Bergisch Gladbach, GER
Anti-Hsp90 alpha/beta antibody (F-8)	Santa Cruz Biotechnology, Inc., Dallas, TX, USA
Anti-LaminB1, mouse, monoclonal	Proteintech Group, Rosemont, IL, USA
Goat anti-mouse IgG (H+L), HRP	Thermo Fisher Scientific Inc., Waltham, MA, USA
PE rat anti-human CD184 (clone 1D9)	Becton Dickinson and Company, Franklin Lakes, NJ, USA
PE Rat IgG2a, κ isotype control	Becton Dickinson and Company, Franklin Lakes, NJ, USA
Streptavidin-POD conjugate	Merck KGaA, Darmstadt, GER

Antibody or Binding Protein	Manufacturer or Description
Anti-fluorescein antibody (clone 5D6.2)	Merck KGaA, Darmstadt, GER
Anti-Cas9 antibody (7A9-3A3)	Santa Cruz Biotechnology, Inc., Dallas, TX, USA

2.1.6 Plasmids, Primer and Enzymes for PCR

Table 7: List of used plasmids for cloning or gene amplification approaches

Plasmid	Description
pEGFP-C1	Kanamycin resistance
pEG-His1:^{His}C3bot$^{Cys\text{-}His}$	Ampicillin resistance
pEG-His1:^{His}C3bot$_{E174Q}$$^{Cys\text{-}His}$	Ampicillin resistance
pET28a:^{His}Cas9^{NLS}	Kanamycin resistance

Table 8: Primer for cloning and sequencing approaches

Application	Primer name	Sequence (5' to 3')
Amplification of CD33 gene fragment	FP_CD33	ggatgggcaaggggaagttgc
Amplification of CD33 gene fragment	RP_CD33	agttcatgggtactgcagggca
Amplification of eGFP gene fragment	FP_eGFP	tgcttcagccgctacc
Amplification of eGFP gene fragment	RP_eGFP	acagctcgtccatgc
Amplification of LSR gene fragment	FP_LSR	acaggtggcgttcctgttga
Amplification of LSR gene fragment	RP_LSR	ggaccaccctaggcaagcaa
Cloning of C3bot1$_{(E174Q)}$_Cas9$^{NLS\text{-}His}$	FP_ pTI2-1-1	ggcaaatattctgaaatgagc
Cloning of C3bot1$_{(E174Q)}$_Cas9$^{NLS\text{-}His}$	FP_C3-Cas9	aaaaaccatggtgatgatggtgatgtc cgctccctacttttctcttttttctttggagg
Cloning of C3bot1$_{(E174Q)}$_Cas9$^{NLS\text{-}His}$	RP_ pGEX3	tcaagaattatacactccg

Application	Primer name	Sequence (5’ to 3’)
Cloning of C3bot1$_{(E174Q)}$_Cas9$^{NLS\text{-}His}$	RP_C3-Cas9	aaaaaggatccggtagcggcatggacaa gaagtacag
Sequencing C3bot1$_{(E174Q)}$_Cas9$^{NLS\text{-}His}$	FP_Cas9_1_Seq	cccaacttcaagagcaacttc
Sequencing C3bot1$_{(E174Q)}$_Cas9$^{NLS\text{-}His}$	FP_Cas9_2_Seq	agagcttcatcgagcgcatgac
Sequencing C3bot1$_{(E174Q)}$_Cas9$^{NLS\text{-}His}$	FP_Cas9_3_Seq	agcctgaccttcaaggaggacatc
Sequencing C3bot1$_{(E174Q)}$_Cas9$^{NLS\text{-}His}$	FP_Cas9_4_Seq	gaacaccaagtacgacgagaac
Sequencing C3bot1$_{(E174Q)}$_Cas9$^{NLS\text{-}His}$	FP_Cas9_5_Seq	gcaagagcaagaagctgaagagcg
Sequencing C3bot1$_{(E174Q)}$_Cas9$^{NLS\text{-}His}$	FP_N-term Cas9_Seq	tgatcaccgacgagtacaag
Sequencing C3bot1$_{(E174Q)}$_Cas9$^{NLS\text{-}His}$	FP_N-Term-C3bot$_{E174Q}$	gcaaaagcttggggtaatg

Table 9: List of enzymes used for cloning or PCR approaches

Enzymes for cloning/PCR approaches	Manufacturer
Antarctic Phosphatase with Antarctic Phosphatase reaction buffer	New England Biolabs, Ipswich, MA, USA
BamHI-HF with CutSmart® buffer	New England Biolabs, Ipswich, MA, USA
NcoI-HF with CutSmart® buffer	New England Biolabs, Ipswich, MA, USA
Q5 high-fidelity DNA polymerase with Q5 reaction buffer	New England Biolabs, Ipswich, MA, USA
Q5® high-fidelity DNA polymerase (0.01 U/ml) with 5x Q5 reaction buffer	New England Biolabs, Ipswich, MA, USA
T4 DNA ligase (20000 units)	New England Biolabs, Ipswich, MA, USA
T4 DNA ligase (5 U/µl)	New England Biolabs, Ipswich, MA, USA
Taq DNA polymerase with Taq buffer	New England Biolabs, Ipswich, MA, USA

2.1.7 DNA Oligos for sgRNA Synthesis

Table 10: DNA oligos for single guide RNA (sgRNA) synthesis with EnGen® sgRNA Synthesis Kit. sgRNAs are ordered from biomers.net GmbH, Ulm (GER)

sgRNA name	Sequence of DNA oligo for sgRNA synthesis (5' to 3')
$sgRNA^{CD33}$	TTCTAATACGACTCACTATAGACAACCAGGAGAAGAUCGGGTTTTAGAGCTAGA
$sgRNA^{GFP}$	TTCTAATACGACTCACTATAGTGAACCGCATCGAGCTGAAGTTTTAGAGCTAGA
$sgRNA^{LSR}$	TTCTAATACGACTCACTATAGGACAGCGTGCGCACCGTCAGTTTTAGAGCTAGA

2.1.8 Eukaryotic and Procaryotic Cell Lines and Corresponding Culture Media

Table 11: Composition of media used for cultivation of prokaryotic cells

Medium	Components	Concentration
LB-agar (autoclaved and poured into petri dishes)	Agar-agar LB-medium Antibiotics (added after autoclaving, < 50 °C)	1.5% add to 100% 100 µg/ml
LB-medium (autoclaved)	Tryptone Yeast-Extract Sodium Chloride	1% 0.5% 1%

Table 12: Prokaryotic cell types with corresponding culture media

Prokaryotic Cell Type	Description	Medium
Escherichia coli BL21	Competent strain used for protein expression	LB-medium or LB-agar
Escherichia coli DH5α	Competent strain used for plasmid amplification	LB-medium or LB-agar

Table 13: Eukaryotic cell lines with corresponding culture media. If not indicated otherwise, the cells were purchased from ATCC, Manassas, VA, USA

Cell Line	Origin	Medium	Supplements
4T1	Murine adenocarcinoma. Model system for stage IV human breast cancer. Provided by Max Planck Institute for Polymer Research, Mainz, GER	RPMI-1640	10% FCS 100 U/ml Pen/Strep 1 mM sodium pyruvate 10 mM HEPES 4.5 g/l glucose
A431	Human epidermoid carcinoma	RPMI-1640	10% FCS 100 U/ml Pen/Strep
HCT116	Colorectal carcinoma	DMEM	10% FCS 100 U/ml Pen/Strep 1 mM sodium pyruvate 1x non-essential amino acids
MDA-MB231	Human adenocarcinoma	DMEM	10% FCS 100 U/ml Pen/Strep 1 mM sodium pyruvate 1x non-essential amino acids
SupT1	Human lymphoblastic lymphoma; T-cell	RPMI-1640	10% FCS 100 U/ml Pen/Strep 10 mM HEPES 2 mM L-glutamine
SupT1ΔCXCR4	SupT1 cell line with CXCR4 knockout. Provided by the Institute of Molecular Virology, University of Ulm, Medical Center, GER	RPMI-1640	10% FCS 100 U/ml Pen/Strep 10 mM HEPES 2 mM L-glutamine
THP-1	Human acute monocytic leukemia.	RPMI-1640	10% FCS 100 U/ml Pen/Strep

Cell Line	Origin	Medium	Supplements
THP-1^{GFP}	THP-1 cells with stable GFP expression. Purchased from Applied Biological Materials Inc., Richmond, CAN	PriGrow II	10% FCS 100 U/ml Pen/Strep

2.1.9 Software and Online Tools

Table 14: List of used software and online tools

Software	Manufacturer
BD FACSDiva^{TM} Software	Becton Dickinson and Company, Franklin Lakes, NJ, USA
Benchling (online tool)	Benchling, San Francisco, CA, USA
BioRender (online tool)	BioRender, Toronto, CAN
BZ-X800 Analyzer	Keyence Corporation, Osaka, JPN
BZ-X800 Viewer	Keyence Corporation, Osaka, JPN
BZ-X800 WideImage Viewer	Keyence Corporation, Osaka, JPN
ChimeraX 1.10.1	University of California San Francisco Resource for Biocomputing Visualization and Informatics, Oakland, CA, USA
Flowing Software 2.5.1	Turku Biosciences, Turku, FIN
GraphPad Prism 10	GraphPad Software, Inc., San Diego, CA, USA
GraphPad Prism 10.4.1	GraphPad Software, Inc., San Diego, CA, USA
ImageJ	National Institute of Health, Bethesda, MD, USA
Incucyte® 2024A	Sartorius AG, Goettingen, GER
LAS V4.13	Leica Microsystems GmbH, Wetzlar, GER
Leica Acquire Software X (LAS X)	Leica microsystems, Wetzlar, GER
Microsoft® Office 365	Microsoft Corporation, Redmond, WA, USA
Tm Calculator version 1.16.6 (online tool)	New England Biolabs, Ipswich, MA, USA

2.2 Methods

2.2.1 Cell Culture

The human cell line MDA-MB231 and the mouse cell line J774A.1 were cultivated in DMEM medium with 10% FCS, 100 U/ml penicillin-streptomycin (Pen/Strep), 1 mM sodium pyruvate and 1x non-essential amino acids. Human A431 cells were cultivated in RPMI medium supplemented with 10% FCS and 100 U/ml Pen/Strep. The human T lymphoblast cell line SupT1 and SupT1 cells with a knockout of the CXCR4 receptor (SupT1ΔCXCR4) were cultured in RPMI medium containing 10% FCS, 100 U/ml Pen/Strep, 10 mM HEPES and 2 mM L-Glutamine. The SupT1ΔCXCR4 cell line was kindly provided by Dan Albers from the Institute of Molecular Virology at the University of Ulm, Medical Center. For cultivation of the tumor-derived murine 4T1 cell line RPMI medium supplemented with 10% FCS, 100 U/ml Pen/Strep, 1 mM sodium pyruvate, 10 mM HEPES and 4.5 g/l Glucose was used. All cell lines were cultivated at 37 °C, 5% CO_2 and constant humidity and were sub-cultivated every 2 to 3 days in a ratio of 1:3 to 1:20. The adherent cell lines MDA-MB231, A431 and 4T1 were detached by trypsinization, the J774A.1 macrophages were detached with a cell scraper before splitting or seeding.

The osteoclast precursor cell line RAW 264.7 was provided and handled by apl. Prof. Dr. Melanie Haffner-Luntzer from the Institute of Orthopaedic Research and Biomechanics at the University of Ulm, Medical Center under the direction of Prof. Dr. Anita Ignatius. The cells were cultivated in alpha-MEM-medium containing 10% FCS, 100 U/ml Pen/Strep and 2 mM L-Glutamine. The differentiation was induced by addition of 25 ng/ml recombinant human RANKL and 10 ng/ml recombinant human M-CSF. The cells were cultivated at 37 °C, 5% CO_2 and constant humidity and splitted at a confluency of around 80% by adding accutase.

The THP-1 cell line was cultivated in RPMI-1640 medium supplemented with 10% FCS and 100 U/ml Pen/Strep. The THP-1^{eGFP} cell line stably expresses the enhanced green fluorescent protein (eGFP) and was cultivated in PriGrow II medium with 10% FCS and 100 U/ml Pen/Strep as additives. To select for eGFP positive cells, 1.2 µg/ml puromycin were added freshly after each split. Cell numbers were kept between $2*10^5$ cells per ml to $1*10^6$ cells per ml and the cells were incubated at 37 °C, 5% CO_2 and constant humidity. For the differentiation of THP-1 cells or THP-1^{eGFP} cells to the respective M0 macrophages, 100-

200 nM phorbol 12-myristate 13-acetate (PMA) were added to the culture medium for at least 48 h. Differentiation was proven by binding of anti-CD11b antibody with VioBlue tag to the cell surface of the M0 macrophages on ice for 45 min. Residual antibody was removed by washing with PBS at 500 rcf for 6 min. Cell viability was monitored simultaneously by adding SYTOX™ Green Ready Flow™ Reagent for 15 min at room temperature before flow cytometry.

2.2.2 Phase-Contrast Microscopy

For analysis of cell morphology, the cells were seeded in microtiter plates and treated as indicated. Per well, one image was recorded with the phase-contrast microscope and representative images with scale bars are shown.

2.2.3 SDS-PAGE and Western Blot

To separate proteins by their molecular weight, sodium dodecyl-sulfate polyacrylamide gel electrophoresis (SDS-PAGE) with an 8-20% acrylamide gradient gel was performed. For pouring the gel, the components listed in Table 4 for SDS gels with 8% acrylamide/bisacrylamide and 20% acrylamide/bisacrylamide were mixed, respectively. An equal volume of each SDS gel was aspirated into the same 10 ml serological pipette, starting with the 8% SDS gel. One air bubble of around 0.5 ml was taken up to mix the gel solutions in the pipette. The gel was slowly poured and distributed into the assembled glass chamber resulting in a gradient from low acrylamide concentrations on the upper side of the gel and high concentration on the bottom of the gel. Samples were supplemented with 1x Laemmli buffer with dithiothreitol and heat denatured at 95 °C for 10 min to break secondary and tertiary protein structures. The gel was mounted into the running chamber, and it was filled with SDS running buffer, before samples and ladders were applied to the gel as indicated. A current of 40 mA per gel was applied for 1.5 h to separate the proteins by their molecular weight.

For immunodetection of the proteins of interest they were blotted onto a nitrocellulose membrane after SDS-PAGE. Therefore, blotting paper, the nitrocellulose membrane and the SDS gel were briefly equilibrated in Towbin buffer. A stack of three blotting paper was placed on the anode (+) followed by the nitrocellulose membrane and the SDS gel. The stack was covered with another three blotting paper and air bubbles were removed for even protein transfer before the cathode (-) was placed on top. The 1.5-fold area of the

SDS-gel equaled the applied current in mA for 1.5 h. To prevent non-specific antibody binding after blotting, the membrane was blocked for 1 h at RT with 5% skimmed milk powder in PBS-T. The indicated primary antibody targeting the protein of interest was diluted in PBS-T and incubated on the membrane over night at 4 °C. The membrane was washed three times with PBS-T for each 5 min on an orbital shaker. The secondary HRP-coupled antibody or binding protein was diluted in PBS-T and incubated on the membrane for 1 h at RT, before the washing steps were repeated. For detection of the bound antibodies, Immobilon Western Chemiluminescent HRP Substrate was applied according to the manufacturer's instructions. The chemiluminescent signal was detected in the iBright™ CL1500 imaging system, and the signal intensities were analyzed via ImageJ.

2.2.4 Cloning of C3bot1$_{(E174Q)}$_Cas9$^{NLS-His}$

Extraction of the Cas9 Gene from pET28a:^{His}Cas9^{NLS}

The Cas9 gene together with a nuclear localization sequence (NLS) was cloned from the plasmid pET28a:^{His}Cas9^{NLS} using overhang primers with restriction sites for BamHI (FP_C3-Cas9) and NcoI as well as a new His-tag (RP_C3-Cas9). The Cas9 gene was amplified via PCR containing 1 ng of plasmid DNA, 0.5 µM of each primer, 200 µM deoxynucleotides (dNTPs), 0.02 U/µl Q5® high-fidelity DNA polymerase and 6% dimethyl sulfoxide (DMSO) in Q5 reaction buffer. The DNA amplification program run in the thermocycler is depicted in Table 15. The annealing temperature was calculated using the New England Biolab Tm Calculator and the extension time was set to 30 sec/kbp of the amplified insert.

Table 15: Thermocycler program for amplification of BamHI_Cas9$^{NLS-His}$_NcoI with Q5® high-fidelity DNA polymerase

Stage	Temperature	Time	Cycles
Initial denaturation	98 °C	30 sec	1
Denaturation	98 °C	10 sec	35
Annealing	61 °C	30 sec	
Extension	72 °C	2 min 15 sec	
Final Extension	72 °C	7 min	1

The resulting gene fragment has a length of 4194 bp and contains Cas9 flanked by restriction sites for BamHI and NcoI. It was purified via the FastGene Gel/PCR Extraction Kit following the manufacturer's protocol. Therefore, the PCR product was mixed in a 1:5 (v/v)

ratio with buffer GP1, vortexed and loaded onto the column. DNA was bound to the membrane by centrifugation at 13,000 rpm for 30 sec and washed with buffer GP2. The flowthrough was discarded, and the membrane was dried by centrifugation at 13,000 rpm for 2 min. MilliQ water was pre-warmed to 70 °C and 20 µl were added onto the membrane for elution. This step was repeated after centrifugation at 13,000 rpm for 2 min and the concentration of the resulting insert BamHI_Cas9$^{NLS\text{-}His}$_NcoI was determined by measuring the absorbance at 260 nm via the NanoDrop device.

Amplification and Purification of the Insert BamHI_Cas9$^{NLS\text{-}His}$_NcoI in E. coli DH5α

The gene fragment BamHI_Cas9$^{NLS\text{-}His}$_NcoI was inserted into a pCR^{TM}-blunt vector. Therefore, 25 ng of the vector were combined with 300 ng of the insert and 5 Units T4 DNA ligase in T4 DNA ligase buffer and incubated for 1 h at room temperature. Competent *E. coli* DH5α were thawed on ice and 5 µl ligation product were added and incubated for 30 min. A heat shock transformation was performed, and a single colony was inoculated in 15 ml LB-medium incubating over-night at 37 °C and 180 rpm. To isolate the resulting pCR-blunt: BamHI_Cas9NLS-His_NcoI plasmid from the bacteria, the my-Budget plasmid mini kit protocol was performed according to the manufacturer's instructions. The DNA concentration was determined by measuring the absorbance at 260 nm via the NanoDrop device.

Assembling Backbones and the Gene of Interest

For insertion of the gene of interest (Cas9$^{NLS\text{-}His}$) into C3bot1- and C3bot1$_{E174Q}$-encoding plasmid backbones, all components need to be digested with the same restriction enzymes. Therefore, 2 µg of BamHI_Cas9$^{NLS\text{-}His}$_NcoI, pEG-His1:^{His}C3bot1$^{Cys\text{-}His}$ or pEG-His1:HisC3bot1$_{E174Q}$$^{Cys\text{-}His}$ were combined with 1 µl BamHI-HF and 1 µl NcoI-HF in 1x CutSmart buffer and incubated for 1 h at 37 °C. The digested backbones were dephosphorylated to prevent re-circularization during ligation by adding 2 µl Antarctic Phosphatase and incubation for 30 min at 37 °C. The enzyme was heat-inactivated for 2 min at 80 °C. All digested products were separated via agarose gel electrophoresis (110 V, 45 min) in a 1% agarose gel and purified by using the FastGene Gel/PCR Extraction Kit following the manufacturer's instructions as described above. The DNA concentration of the resulting products Cas9$^{NLS\text{-}His}$ (insert), and the linearized vectors pEG-His1:^{His}C3bot1$^{Cys\text{-}His}$ and pEG-His1:HisC3bot1$_{E174Q}$$^{Cys\text{-}His}$ was determined by measuring the absorbance at 260

nm via the NanoDrop device. For ligation of $Cas9^{NLS\text{-}His}$ with each dephosphorylated vector a 1:3 and 1:10 ratio (w/w) of pEG-His1:^{His}C3bot1$^{Cys\text{-}His}$ or pEG-His1:HisC3bot1$_{E174Q}{}^{Cys\text{-}His}$ to purified insert was tested and incubated for 1 h at room temperature with 1 µl T4 DNA ligase.

Colony PCR

To verify the DNA insertion into the backbone in a high throughput assay, a colony PCR was performed. Therefore, *E. coli* DH5α were heat shock transformed at 42 °C with pEG-His1:HisC3bot1_Cas9NLS-His or pEG-His1:HisC3bot1E174Q_Cas9NLS-His. The colonies were grown over night at 37 °C on an LB agar-plate. A PCR master mix containing 1.5 mM MgCl2, 333 µM dNTPs, 1.25 units Taq DNA polymerase and 0.5 µM of forward and reverse primer (FP_pTI2-1-1 and RP_pGEX3) were combined in 1x standard Taq reaction buffer. The master mix was aliquoted into PCR tubes (20 µl per tube) and a single E. coli colony per tube was picked and shortly dipped into the mix before inoculation in 1 ml LB-medium for later amplification. Table 16 shows the program run on the PCR thermocycler with the annealing temperature calculated by the New England Biolab Tm Calculator and the extension time set to 30 sec/kbp of the amplified gene. E. coli clones harboring plasmids with the gene fragment in the correct length (5189 bp) were detected by agarose gel electrophoresis of the PCR product. Positive clones were inoculated in 15 ml LB-medium and incubate over night at 37 °C and 180 rpm before the my-Budget plasmid mini kit protocol was performed according to the manufacturer's instructions to isolate the plasmid. DNA concentration was determined by measuring the absorbance at 260 nm via the NanoDrop device.

Table 16: Thermocycler program for colony PCR

Stage	**Temperature**	**Time**	**Cycles**
Initial denaturation	95 °C	30 sec	1
Denaturation	95 °C	30 sec	30
Annealing	42 °C	1 min	
Extension	68 °C	5 min 20 sec	
Final Extension	68 °C	5 min	1

Sequence Verification

The sequence of the isolated plasmid DNA was confirmed by LightRun Sanger sequencing. Therefore, 5 µl plasmid DNA (100 ng/µl) were mixed with 5 µl of the respective sequencing primer (5 µM) listed in Table 8. The mixes were sent to Eurofins Genomics, Luxemburg (LUX). For sequence comparison the Benchling online tool was used.

2.2.5 Expression of Recombinant Proteins in *E. coli* BL21

Heat shock transformation was accomplished with *E. coli* BL21 and 40 ng plasmid DNA encoding for the protein of interest. Subsequently, inoculation of a single colony in 5 ml LB-medium was performed in a shaking incubator for 5 h at 37 °C and 180 rpm. This first pre-culture was expanded to a 150 ml overnight culture before it was used to inoculate 4 L of the main culture in LB-medium. The bacteria were grown to an optical density at 600 nm of 0.6 to 0.8 at 37 °C and 180 rpm and protein expression was induced with 0.5 mM isopropyl-d-1-thiogalactopyranoside (IPTG). The main culture was incubated overnight (~18 h) at 29 °C and 180 rpm before the *E. coli* cells were harvested by centrifugation at 5500 rcf and 4 °C for 10 min. For GST-tagged proteins the pellet was resuspended in 40 ml lysis-buffer, while for His-tagged proteins 40 ml NPI-20 buffer with 1% phenylmethylsulfonyl fluoride (PMSF) was used. Cell lysis was performed with EmulsiFlex-C3 homogenizer at 1500 bar and insoluble cell debris was removed by centrifugation at 13,000 rcf at 4 °C for 30 min. The supernatant was filtered twice (0.45 µm and 0.2 µm) with syringe filters.

2.2.6 Purification of Recombinant C3bot1$_{(E174Q)}$_Cas9$^{NLS\text{-}His}$

The His-tagged proteins C3bot1_Cas9$^{NLS\text{-}His}$ and C3bot1$_{E174Q}$_Cas9$^{NLS\text{-}His}$ were expressed in *E. coli* BL21 cells as described in chapter 2.2.5. The sterile filtered supernatant harboring the protein of interest was loaded onto 1 ml bed volume of NPI20-buffer equilibrated PureCube 100 INDIGO Ni-agarose and incubated over night at 4 °C in an overhead shaker. The entire approach was loaded onto Midi Plus columns equilibrated with NPI20-buffer and washed three times with NPI20-buffer at 4 °C and 400 rcf for 10 min. In eight steps 1 ml of NPI250-buffer was added for elution of the proteins, followed by two elution steps with 0.5 ml NPI250-buffer. The elution fractions were analyzed by SDS-PAGE and Coomassie staining. Fractions with high protein concentration and purity were pooled and concentrated via Viviaspin20 with a molecular weight cut off of 30 kDa at 3113 rcf and 4 °C.

To remove the imidazole-containing NPI250-buffer dialysis was performed overnight with a dilution factor greater than 1:1000 in PBS buffer. Protein concentration was determined against a bovine serum albumin (BSA) standard with densitometric analysis after SDS-PAGE with subsequent Coomassie staining.

2.2.7 Purification of Recombinant $^{GST\text{-}Cys}$C3bot1

The GST-tagged protein $^{GST\text{-}Cys}$C3bot1 was expressed in *E. coli* BL21 cells as described in chapter 2.2.5. The sterile filtered supernatant harboring the protein of interest was incubated overnight at 4 °C with 1.2 ml Protino Glutathione (GSH) Agarose 4B-beads equilibrated in PBS (pH 7.4). The beads were washed with washing buffer and PBS (pH 7.4) by centrifugation at 4 °C and 3000 rcf for 5 min. Elution was performed by cleavage of the GST-tag by 30 NIH units thrombin per liter main culture for 1 h at room temperature. The protein was eluted from the GSH agarose beads with PBS (pH 11). Thrombin depletion was achieved by incubating the supernatant for 10 min at room temperature with 45 µl Benzamidine-Sepharose 6B-beads. The beads were removed by centrifugation at 10,000 rcf and 4 °C for 30 sec. ^{Cys}C3bot1 was re-buffered in PBS (pH 7.4) before protein concentration was determined against a bovine serum albumin (BSA) standard with densitometric analysis after SDS-PAGE with subsequent Coomassie staining.

2.2.8 Single Guide RNA Synthesis

For the synthesis of single guide RNA (sgRNA) with the EnGen® sgRNA Synthesis Kit a customized DNA oligo containing a T7 promotor sequence (5'–TTCTAATACGACTCACTATA–3'), a target specific sequence and an overlap sequence for binding the reaction partners of the kit (5'–GTTTTAGAGCTAGA–3') was designed. The target specific sequence of the designed DNA oligo determines the gene that can be recognized and bound by the final sgRNA product. For targeting the lipolysis-stimulated lipoprotein receptor (LSR), the target sequence 5'–GGACAGCGTGCGCACCGTCA–3' was used. To target the enhanced green fluorescence protein (eGFP), a DNA oligo containing the target specific sequence fragment 5'-GTGAACCGCATCGAGCTGAA–3' was designed. For targeting of the monocytic cell surface marker CD33, the DNA oligo 5'-GACAACCAGGAGAAGATCGG-3' was used for sgRNA synthesis (see Table 10).

The respective customized DNA oligo was combined with nuclease-free water, EnGen® 2X sgRNA reaction mix (S. pyogenes), DTT and the EnGen® sgRNA enzyme mix according to the

EnGen® sgRNA Synthesis Kit protocol and incubated for 30 min at 37 °C. Afterwards, the reaction was transferred to ice and 30 µl nuclease-free water and 2 µl DNase I were added to digest redundant DNA. For purification of the LSR-targeting sgRNA ($sgRNA^{LSR}$) or eGFP-targeting sgRNA ($sgRNA^{eGFP}$) the Monarch® RNA Cleanup Kit was used following the manufacturer's instructions. The elution of the final products was performed in nuclease-free water and the concentrations were determined via the NanoDrop device.

2.2.9 *In vitro* Cleavage Assay with C3bot1$_{(E174Q)}$_Cas9$^{NLS\text{-}His}$

Amplification of an eGFP Gene Fragment from Plasmid DNA

To test the functionality of Cas9 enzymes *in vitro*, a target DNA harboring the respective sgRNA protospacer sequence is used. In this assay, an eGFP gene fragment was isolated and amplified from the plasmid pEGFP-C1. Therefore, 1 ng plasmid DNA was combined with 1x Q5 reaction buffer, 0.5 µM of each primer (FP_eGFP and RP_eGFP), 200 µM dNTPs and 0.02 U/µl Q5 high-fidelity DNA polymerase. The reaction mix was placed into the thermocycler and the PCR program described in Table 17 was run. The annealing temperature was calculated using the NEB Tm calculator with the primer sequences of FP_eGFP and RP_eGFP. The extension time was set to 30 sec for the 502 bp large eGFP gene fragment that should be amplified.

Table 17: Thermocycler program for amplification of an eGFP gene fragment

Stage	Temperature	Time	Cycles
Initial denaturation	98 °C	30 sec	1
Denaturation	98 °C	10 sec	35
Annealing	63 °C	30 sec	
Extension	72 °C	30 sec	
Final Extension	72 °C	7 min	1

For purification via agarose gel electrophoresis, 5 µl Midori Green Direct were added to the sample and the complete PCR product was loaded onto a 1.5% agarose gel for 60 min at 110 V. The band at 502 bp was cut from the gel and purified using the FastGene Gel/PCR Extraction Kit following the manufacturer's instructions. The product was eluted from the column with 70 °C pre-warmed MilliQ water and the concentration was measured at 260 nm with the NanoDrop spectrophotometer.

Isolation and Amplification of an LSR Gene Fragment from HCT116 Cell Lysate

To proof the functionality of an C3bot1$_{(E174Q)}$_Cas9$^{NLS\text{-}His}$:sgRNA^{LSR} complex *in vitro*, a LSR gene fragment is needed and a genomic PCR from HCT116 cell lyssate was performed to amplify that gene. The cell lysate was collected by resuspending 0.05 – 2*10^6 HCT116 cells in 50 µl lysis buffer with protein degrader of the GeneArt® Genomic Cleavage Detection Kit. This approach was incubated in a thermoblock at 68 °C for 15 min, followed by 95 °C for 10 min for lysis of the cells. To amplify the LSR gene fragment, 0.2 µM of each primer (FP_LSR and RP_LSR) were combined with 25 µl AmpliTaq Gold® 360 Master Mix from the GeneArt™ Genomic Cleavage Detection Kit and 2 µl of the HCT116 cell lysate. The reaction mix was placed into the thermocycler and the PCR program described in Table 18 was run. The Annealing Temperature was calculated using the NEB Tm calculator online tool.

Table 18: Thermocycler program for genomic PCR to amplify an LSR gene fragment

Stage	**Temperature**	**Time**	**Cycles**
Initial denaturation	95 °C	10 min	1
Denaturation	95 °C	30 sec	40
Annealing	62 °C	30 sec	
Extension	72 °C	30 sec	
Final Extension	72 °C	7 min	1

The amplified PCR product with 1373 bp was purified as described above via agarose gel electrophoresis followed by gel extraction with the FastGene Gel/PCR Extraction Kit and concentration determination with the NanoDrop spectrophotometer.

Isolation and Amplification of a CD33 Gene Fragment from THP-1 Cell Lysate

The cell lysate of THP-1 cells, as well as the PCR mix were prepared as described in the chapter before for HCT116 cells. The reaction mix was placed into the thermocycler and the PCR program comparable to the one described in Table 18 was run with an annealing temperature of 63 °C and an extension time of 1 min. Therefore, the primer FP_CD33 and RP_CD33 (see Table 8) were used. The final PCR product had a length of 905 bp and was purified as described above via agarose gel electrophoresis followed by gel extraction with the FastGene Gel/PCR Extraction Kit and concentration determination with the NanoDrop spectrophotometer.

In vitro Cleavage Assay

To examine the ability of Cas9 that was genetically fused to C3bot1 or C3bot1$_{E174Q}$ to specifically cut DNA in the presence of sgRNA, an *in vitro* cleavage assay was performed. Therefore, sgRNA^{eGFP}, sgRNA^{LSR} or sgRNA^{CD33} were combined with the indicated Cas9 variant in a molar stochiometric ratio of 1:1 and incubated for 10 min at room temperature. Subsequently, the corresponding DNA fragment of the eGFP, LSR or CD33 gene was added in a molar stochiometric ratio of 10:1 (Cas9:sgRNA complex to DNA fragment), respectively and incubated at 37 °C for 15 min. Before analysis of the cut gene fragments via agarose gel electrophoresis, 1 µl Proteinase K was added to stop the enzymatic activity of the Cas9 variants. The gel was imaged with the iBright^{TM} CL1500.

2.2.10 Isolation of Cytosolic and Nuclear Cellular Fractions

To monitor the intracellular localization of Cas9 after treatment of cells with different Cas9 variants, the cytosolic and nuclear fraction should be separated. Therefore, cells were seeded into 24-well plates and treated with the indicated concentrations of C3bot1$_{E174Q}$_Cas9$^{NLS\text{-}His}$ or ^{His}Cas9$^{NLS\text{-}Cys}$ for a stated period of time at 37 °C, 5% CO_2 and constant humidity. All following steps and incubations were conducted at 4 °C with ice-cold buffers. The cells were harvested and residual Cas9 variants were removed by two washing steps with PBS at 500 rcf for 5 min, respectively. For extraction of the cellular compartments, the Nuclear Extraction Kit buffers were supplemented with 1x DTT and 1x protease inhibitor cocktail according to the manufacturer's instructions. The cells were resuspended in cytoplasm extraction buffer, briefly vortexed and incubated for 10 min. After centrifugation at 1000 rcf for 3 min, cytosolic proteins were collected from the supernatant. The pellet was dissolved in nuclear extraction buffer and the nuclei were disrupted mechanically by pipetting up and down 100 times before incubation for 30 min. The sample was centrifuged at 1000 rcf for 3 min to collect the supernatant harboring soluble nuclear proteins. By adding nuclear lysis buffer and sonification with 15 sec pulses (8-10 times, 30 sec rest) to shear the DNA, insoluble nuclear proteins could be isolated and both nuclear fractions were pooled. For verification of successful fractionation SDS-PAGE and Western Blot (see section 2.2.3) were performed and marker proteins for each fraction were stained with antibodies. Hsp90 is exclusively present in the cytosolic fraction and was detected with an anti-Hsp90 antibody (1:1000 in PBS-T), while LaminB1 is a marker protein for the nuclear fraction and was detected with an anti-LaminB1 antibody (1:10000 in

PBS-T). The presence of Cas9 in both fractions was examined with an anti-Cas9 antibody (1:1000 in PBS-T). For detection, a secondary HRP-coupled goat anti-mouse antibody (1:2500 in PBS-T) was used.

2.2.11 Fluorescence Labelling of C3bot1$_{(E174Q)}$_Cas9$^{NLS-His}$

To monitor the cellular binding and uptake of C3bot1$_{E174Q}$_Cas9$^{NLS-His}$, C3bot1_Cas9$^{NLS-His}$ and ^{His}Cas9$^{NLS-Cys}$ were labelled with DyLight^{488} N-hydroxysuccinimide (NHS) esters. This amine-reactive dye forms covalent bonds with the primary amines of these proteins leading to fluorescently labelled products. The dye solution was prepared fresh for each coupling reaction by dissolving 0.05 mg dye in 5 µl N,N-dimethylformamide (DMF) to achieve a 10 mg/ml stock solution. The dye was incubated with the proteins in a ten-fold molar excess for 1 h and 700 rpm on an orbital shaker at room temperature. To remove residual dye, PBS equilibrated Zeba Spin Desalting Columns with a molecular weight cut-off of 7 kDa were used and elution was performed by centrifugation for 2 min at 1500 rcf. The concentrations of the DyLight^{488} labelled products were determined via SDS-PAGE against a BSA standard. The gel was stained and destained with Coomassie staining/destaining solution and band intensities were analyzed via ImageJ.

2.2.12 Assembly of the Nanocarrier (JM173)$_3$-^{BDP}Avi-C3

To create a modular system capable of binding biotinylated proteins, peptides or molecules bodipy-labelled avidin (^{BDP}Avi) was used as assembly platform. The following steps including further purification of ^{Cys}C3bot1, biotinylation of ^{Cys}C3bot1 and JM173 as well as the HABA assay were performed by the research group of Prof. Dr. Tanja Weil in the Max Planck Institute for Polymer Research in Mainz. The recombinant ^{Cys}C3bot1 toxin was purified by ÄKTA pure™ chromatography system using a Superdex™ 75 Increase 10/300 GL column. Mono-biotinylation of ^{Cys}C3bot1 (B-C3) was performed using a bifunctional biotin-maleimide conjugate with a pH-sensitive hydrazone linker. The degree of biotinylation was determined by bicinchoninic acid assay and biotin quantitation kit according to the manufacturer's instructions. Western Blot analysis confirmed absence of residual free biotin. The second component JM173 was functionalized using a bifunctional biotin-maleimide conjugate with a stable polyethylene glycol linker (B-JM173) and purified by high-performance liquid chromatography.

To calculate the number of B-JM173 molecules that can be assembled onto avidin a competitive binding assay with 4'-hydroxyazobenzene-2-carboxylic acid (HABA) was performed according to the manufacturer. Therefore, avidin was saturated with HABA and rising molar equivalents of B-JM173 were added. The replacement of HABA by B-JM173 leads to a gradual decrease in absorbance at 500 nm, indicating binding of B-JM173 to avidin. This assay revealed that one molar equivalent of B-JM173 can be assembled per avidin binding pocket and lead to the final stoichiometric molar ratio of 1:1:3 (^{BDP}Avi to B-C3 to B-JM173) for assembly of the nanocarrier. Hence, 10 µg ^{BDP}Avi and the molar equivalent of B-C3 were combined in 50 mM HEPES buffer and incubated for 45 min on a shaker at 1000 rpm and room temperature. B-JM173 was added to the ^{BDP}Avi-C3 complex in three-fold molar excess and incubated for 15 min under the same conditions as before to generate the nanocarrier $(JM173)_3$- ^{BDP}Avi-C3. For control constructs lacking JM173, C3 toxin or both, the respective component was replaced by 50 mM HEPES buffer during the corresponding incubation step. Depletion of non-bound B-JM173 and buffer exchange to 25 mM HEPES were performed by ultrafiltration in Vivaspin 500 tubes with a molecular weight cut off of 30 kDa. The concentration of the final constructs $(JM173)_3$- ^{BDP}Avi-C3, ^{BDP}Avi-C3, $(JM173)_3$- ^{BDP}Avi and ^{BDP}Avi was determined by linear calibration against the bodipy-labelled platform at λ_{abs} = 495 nm via Nanodrop. The assembled products were stored at 4 °C for up to three weeks.

2.2.13 Determination of CXCR4 Expression Levels in Different Cell Lines

For investigation of the CXCR4 expression on the cell surface flow cytometry experiments were performed. Therefore, adherent cells were mechanically detached from the culture flask and the cell number was adjusted to $1*10^6$ cells per ml with culture medium before 200 µl cell suspension were transferred into reaction tubes, respectively. For suspension cells, 200 µl with a total cell number of $2*10^5$ cells were prepared per reaction tube. 1-5 µl of PE-labelled rat anti-humanCD14 or the corresponding rat IgG2a κ isotype control were added to the cells and incubated on ice for 1 h. The cells were washed twice with ice cold PBS by centrifugation for 3 min at 800 rcf and 4 °C, before they were resuspended in 200 µl ice cold PBS. Flow cytometric analysis of the cell surface-bound antibodies was performed using the BD FACSCelesta™ device and BD FACSDiva™ software. The data was evaluated by Flowing Software 2 and GraphPad Prism 10.

2.2.14 Binding- and Competition Assay

To examine the binding of the JM173-containing constructs to the cell surface of CXCR4 expressing cells and to proof receptor specificity of that binding, flow cytometric analysis was performed. Adherent cells were detached mechanically from the culture flask and 200 µl cell suspension with a cell number of $1*10^6$ cells per ml were prepared, respectively. The cells were incubated on ice for at least 10 min to stop endocytotic processes before treatment with 250 nM of the bodipy-labelled constructs $(JM173)_3$-^{BDP}Avi-C3, $(JM173)_3$-^{BDP}Avi, ^{BDP}Avi-C3 or ^{BDP}Avi on ice for 30 min. For competition assays, free non-biotinylated JM173 peptide was added in the indicated concentrations simultaneously. The cells were washed twice with ice cold PBS by centrifugation for 3 min at 500 rcf and 4 °C and resuspended in PBS for the measurement with BD FACSCelesta™ device. Data was analyzed with BD FACSDiva™ software, Flowing Software 2 and GraphPad Prism 10.

2.2.15 Fluorescence Microscopy

4T1 cells and A431 cells were seeded in an 8-well µ-slide with $2*10^4$ cells per ml or $1.7*10^4$ cells per ml, respectively. They were treated with the indicated concentrations of $(JM173)_3$-^{BDP}Avi-C3, $(JM173)_3$-^{BDP}Avi, ^{BDP}Avi-C3 or ^{BDP}Avi over night at 37 °C, 5% CO_2 and constant humidity. Treatment media were removed, and the cells were washed twice with PBS buffer before fixation with 4% paraformaldehyde for 20 min at RT. Following three washing steps with PBS buffer, the actin cytoskeleton was stained with SiR-actin (1:2000 in PBS) for 45 min at RT. Hoechst33342 was added in a 1:5000 dilution to the PBS-washed cells and incubated for 10 min at RT. After removing the staining solution, the cells were stored in 0.01% sodium azide in PBS buffer at 4 °C in the dark until measurement. Fluorescence microscopy pictures were taken with Keyence BZ-X810 fluorescence microscope using DAPI, GFP, and Cy5 filter. Per well, 3 to 5 images were recorded and representative pictures with scale bar are shown.

2.2.16 Sequential ADP-Ribosylation Assay

For determination of the intracellular Rho ribosylation status after intoxication with *Clostridium botulinum* C3 toxin, a sequential ADP-ribosylation assay was performed. Therefore, 4T1 cells were seeded into 24 well-plates 24 h prior to the indicated treatment with a cell number of $2*10^4$ cells per well and incubated overnight at 37 °C, 5% CO_2 and constant humidity. The cells were treated for 6 h and washed three times with PBS to

remove residual toxin. Lysis was performed at -20 °C for at least 30 min before scratching the cells off with 30 µl ADP-ribosylation buffer per well. 20 µl of the cell lysates were transferred into a 1.5 ml reaction tube and combined with 10 pmol C3lim and 15 nM fluorescein-NAD^+ or biotin-NAD^+, respectively. This mix was incubated for 30 min at 37 °C and the reaction was stopped by adding 1x Laemmli buffer with DTT and heat denaturation at 95 °C for 10 min. SDS-PAGE and Western Blot were performed (section 2.2.3) to detect fluorescein (anti-fluorescein antibody, 1:500 in PBS-T) coupled to Rho, biotin coupled to Rho (Streptavidin-POD conjugate, 1:5000 in PBS-T) and Hsp90 (anti-Hsp90 antibody, 1:1000 in PBS-T) as a housekeeping protein and loading control. Primary antibodies were detected with a horseradish peroxidase-coupled goat anti-mouse antibody (1:2500 in PBS-T). Since only non-modified Rho proteins can be labelled with fluorescein in the second reaction, weak fluorescein signals in the Western Blot correspond to a high ADP-ribosyltransferase activity of C3 toxin in living cells. All measured signals for fluorescein-labelled Rho were normalized to the respective Hsp90 loading control using ImageJ for signal quantification.

2.2.17 Cell Proliferation Assay – Colorimetric Readout

The cells were seeded into a 96-well plate 24 h prior to the indicated treatment. After incubation over a designated time, CellTiter 96® AQ_{ueous} One Solution Reagent (MTS-reagent) was added directly into the wells with 10 % of the well volume (e.g. 10 µl MTS-reagent in 100 µl treatment medium). The plate was incubated for 1-2 h at 37 °C and 5% CO_2 before the colorimetric change was measured by absorbance at 490 nm using a microplate reader.

2.2.18 Cell Proliferation Assay – Live Cell Imaging

4T1 and MDA-MB231 cells were seeded in 96-well plates with $1*10^5$ cells/13 ml or $3*10^5$ cells/13 ml, respectively and incubated over night at 37 °C, 5% CO_2 and constant humidity. The cells were each treated with the indicated concentration of $(JM173)_3$-^{BDP}Avi-C3, $(JM173)_3$-^{BDP}Avi, ^{BDP}Avi-C3, ^{BDP}Avi, C3bot1 or JM173 before live cell imaging was performed using the Incucyte® SX5. Imaging parameters: standard scan type, adherent cell-by-cell, 10x objective, phase contrast, scan interval 2 h, total scan time up to 120 h. Data were evaluated with the software Incucyte® 2024A.

2.2.19 Effect of $(JM173)_3$-Avi-C3 on Osteoclast Formation and Resorption Activity

These assays were conducted in collaboration with Iris Baum and apl. Prof. Dr. Melanie Haffner-Luntzer from the Institute of Orthopaedic Research and Biomechanics at the University of Ulm, Medical Center under the direction of Univ.-Prof. Dr. Anita Ignatius. Data collection, analysis and visualization were performed by Nicole Stadler at the Institute of Experimental and Clinical Pharmacology, Toxicology and Pharmacology of Natural Products, University of Ulm, Medical Center.

For examination of the influence of $(JM173)_3$-^{BDP}Avi-C3, $(JM173)_3$-^{BDP}Avi, ^{BDP}Avi-C3, ^{BDP}Avi or JM173 onto the differentiation of RAW 264.7 cells to osteoclasts, the indicated concentrations of all constructs were administered to the cells, respectively. By adding 25 ng/ml recombinant human receptor activator of NF-κB ligand (rhRANKL) and 10 ng/ml recombinant human macrophage colony-stimulating factor (rhM-CSF) osteoclastic differentiation was induced for three days. After a medium change and additional two days of incubation, the multinuclear differentiated osteoclasts were stained with tartrate-resistant acid phosphatase (TRAP) Kit according to the manufacturer's instructions. TRAP positive cells were counted at 100-fold magnification with a Leica DMI6000 B microscope and a DFC420 C camera.

The osteoclast resorption activity was determined in OsteoAssay human bone plates by seeding and differentiation of RAW 264.7 cells as described above under the presence of $(JM173)_3$-^{BDP}Avi-C3, $(JM173)_3$-^{BDP}Avi, ^{BDP}Avi-C3, ^{BDP}Avi, or JM173 at the indicated concentrations. After three days and seven days a medium change was performed. On day ten, the cells were detached with 5% trypsin for 5 min and the OsteoAssay human bone plate was washed twice with water. Mineralization was stained by Von Kossa staining, leading to transparent areas where the bone was degraded by active osteoclasts and black, non-resorbed areas. Imaging was performed with a Leica DMI6000 B microscope and a DFC420 C camera and the resorption area was quantified using the image processing software LASX.

2.2.20 Effect of $(JM173)_3$-^{BDP}Avi-C3-treatment on Osteoblast Differentiation

These assays were conducted in collaboration with Iris Baum and apl. Prof. Dr. Melanie Haffner-Luntzer from the Institute of Orthopaedic Research and Biomechanics at the University of Ulm, Medical Center under the direction of Univ.-Prof. Dr. Anita Ignatius. Data

collection, analysis and visualization were performed by Nicole Stadler at the Institute of Experimental and Clinical Pharmacology, Toxicology and Pharmacology of Natural Products, University of Ulm, Medical Center.

The influence of $(JM173)_3$-^{BDP}Avi-C3 on the differentiation of pre-osteoblastic MC3T3 cells, was examined following an established protocol [252]. Briefly summarized, osteoblastogenesis of MC3T3 cells was induced by addition of 10 mM β-glycerophosphate and 0.2 mM ascorbate-2-phosphate. Simultaneously, different concentrations of $(JM173)_3$-^{BDP}Avi-C3, $(JM173)_3$-^{BDP}Avi, ^{BDP}Avi-C3 or ^{BDP}Avi were added. Ten days after initiation of differentiation, total RNA was isolated from the cells and quantitative polymerase chain reaction (qPCR) was performed to analyze the mRNA levels of the differentiation markers alkaline phosphatase (AP), Runt-related transcription factor 2 (RUNX2), osteocalcin (BGLAP) and the antigen KI67 [252]. Relative gene expression compared to the housekeeping gene encoding for β2-Microglobulin (B2M) was calculated using the ΔΔCT method with PCR efficiency correction.

3 Results

The *Clostridium botulinum* C3 toxin isoform 1 (C3bot1, in the following designated as C3) holds significant pharmacological potential due to its dual capability as specific Rho-inhibitor and cell type selective transport system. C3 preferentially enters the cytosol of monocytic cells, making it valuable for targeted therapeutic applications. A single point mutation from glutamic acid to glutamine at position 174 of the C3 toxin leads to inactivation of the enzyme activity without disturbing the cellular uptake mechanism, creating a non-toxic vehicle for cell type selective delivery of pharmacologically active cargo molecules. The following set of experiments assesses the dual functionality of C3 toxin as Rho-inhibitor for down-modulation of breast cancer cell proliferation and as an cytosolic delivery system for Cas9.

3.1 *Clostridium botulinum* C3 toxin: A Rho-Inhibitor for Down-Modulation of Breast Cancer Cell Proliferation

3.1.1 Assembly and Characterization of $(JM173)_3$-Avi-C3

To assemble the nanocarrier components JM173 and C3 toxin on the avidin platform, they need to be biotinylated. Therefore, glutathione-S-transferase (GST)-coupled C3 toxin harboring a C-terminal cysteine (GST-^{Cys}C3) was recombinantly expressed in *E. coli* BL21. To achieve maximum protein yield, buffers with different pH values were tested for elution of thrombin cleaved ^{Cys}C3 from the glutathione-agarose beads (see section 2.2.7). The highest yield of ^{Cys}C3 elution can be obtained when using PBS at pH 11 (Figure 8) leading to a nearly complete detachment of ^{Cys}C3 and GST-^{Cys}C3 from the glutathione agarose beads. To further purify ^{Cys}C3 (23.3 kDa) from remaining GST-^{Cys}C3 (50.6 kDa), the elutions were pooled and purified by size exclusion chromatography using the ÄKTA pure protein purification system. By utilizing the thiol group of the C-terminal cysteine, a biotin-maleimide conjugate with a pH-sensitive hydrazone linker was coupled to ^{Cys}C3 resulting in mono-biotinylated C3 toxin (B-C3) (Figure 5a). The JM173 peptide was kindly provided by Dr. Mirja Harms (Institute for Molecular Virology, University Ulm) and functionalized with a bifunctional maleimide-biotin connected via a stable polyethylene glycol linker (Figure 5b). The biotinylation was performed by Bingjie Gao (Max-Planck Institute for Polymer Research, Mainz) in close collaboration with our common project C01 in the CRC1279.

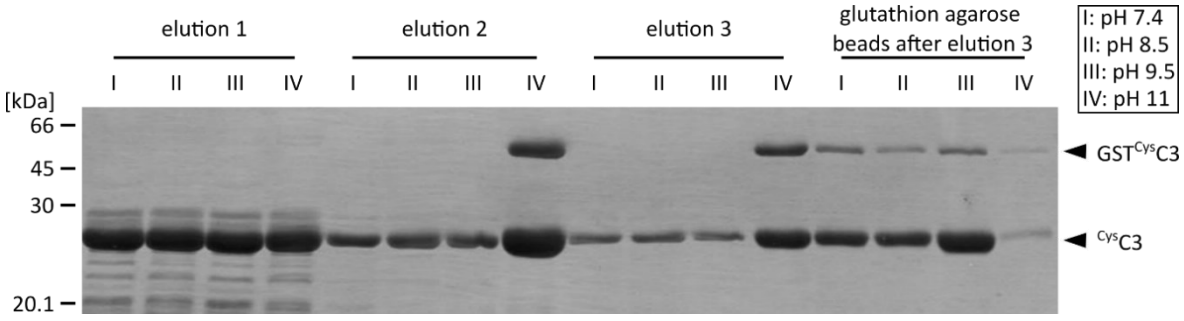


Figure 8: Optimization of ^{Cys}C3 purification. Coomassie stained SDS-PAGE of the elution fractions and glutathione agarose beads after purification of ^{Cys}C3 (23.3 kDa) to optimize the protein yield by editing the elution buffer pH from 7.4 (I) to 11 (IV). Optimization experiments were performed with Johanna Diehm, a Bachelor student under my supervision [253].

B-C3 without remaining biotin or non-biotinylated ^{Cys}C3 is crucial for the later assembly on the platform together with B-JM173. Following biotinylation of ^{Cys}C3 and ultrafiltration, the resulting B-C3 was analyzed via Western blot showing a complete depletion of residual biotin (Figure 9a). In addition, the biotinylation degree was measured and calculated by bicinchoninic acid assay and Biotin Quantitation Kit followed Matrix-assisted laser desorption/ionization time-of-flight (MALDI-ToF) mass spectrometry (Figure 9b). These analyses were performed together with Bingjie Gao (Max-Planck Institute for Polymer Research, Mainz) and revealed that the biotinylation degree varied batch dependent from 40% to 93%. To verify the remaining ADP-ribosylation activity of B-C3 after biotinylation, J774A.1 macrophages were incubated for 24 h with 100 nM or 300 nM B-C3, ^{Cys}C3 or C3 wildtype toxin, respectively. Light microscopic pictures taken hourly showed a clear C3-morphology after 8 h of incubation, defined by long protrusions and condensed cell bodies, that is independent of the C3 variant used for intoxication (Figure 9c). In summary, both molecules that will be assembled on the avidin platform have been successfully purified, biotinylated and functionally characterized.

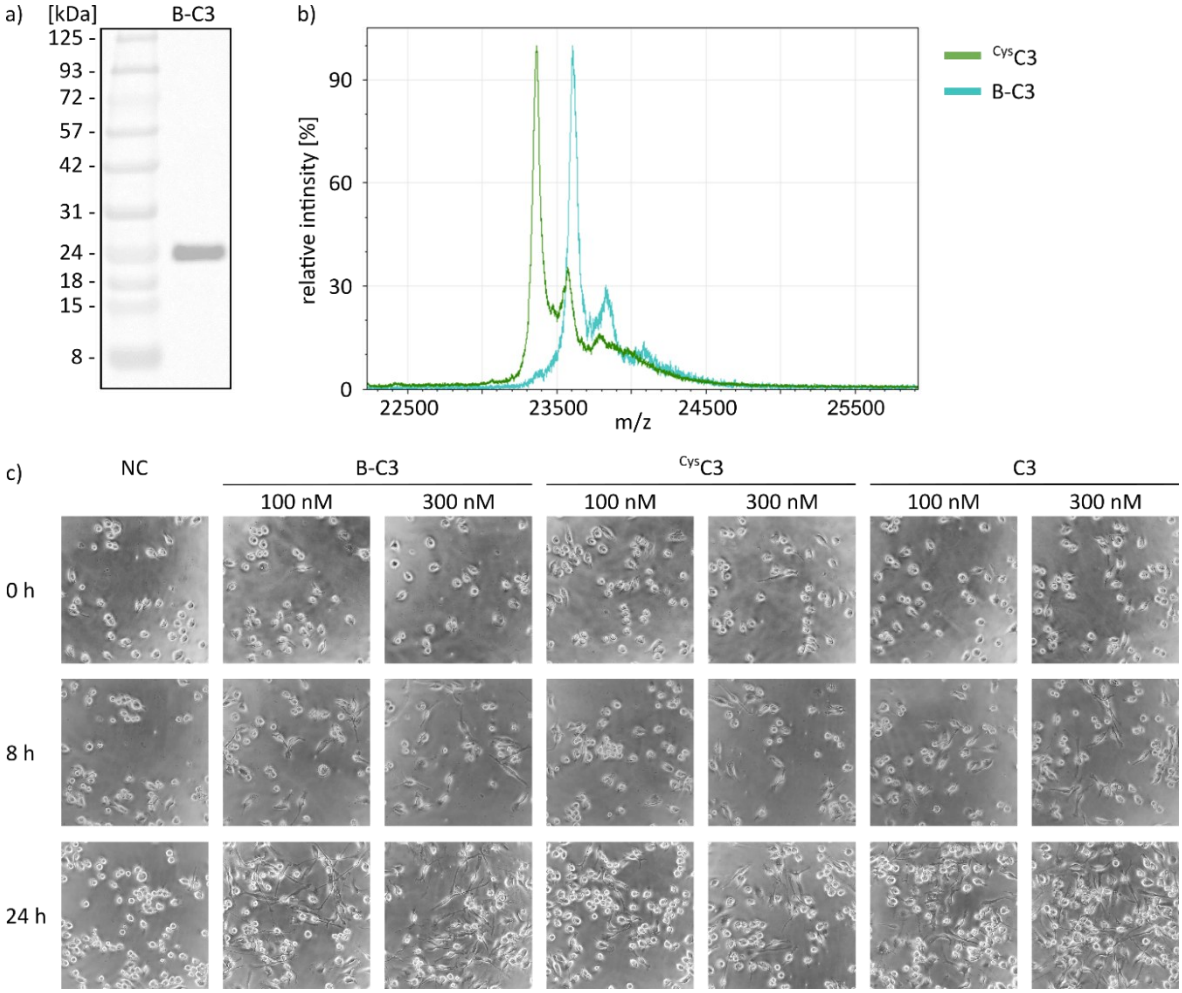


Figure 9: Purity and enzyme activity tests of ^{Cys}C3 and B-C3. ***(a)*** *Western Blot analysis of B-C3 detected with biotin-binding Streptavidin-Peroxidase conjugate showed no free biotin linker after biotinylation of ^{cys}C3.* ***(b)*** *MALDI-TOF mass spectrometry analysis of ^{Cys}C3 (m/z = 23360, green histogram) and B-C3 (m/z = 23618, blue histogram) with synaptic acid as substrate.* ***(c)*** *Light microscopy images of the intoxication of J774A.1 mouse macrophages with 100 nM or 300 nM of B-C3, ^{Cys}C3 or C3 wildtype toxin, respectively. Compared to non-treated cells (NC), typical C3-morphology indicated by the formation of long protrusions and condensed cell bodies can be observed after 8 h of intoxication. (a) and (b) were modified from [187], published with CC BY 4.0 license (https://creativecommons.org/licenses/by/4.0/), DOI: 10.3390/jfb16110399.*

Following the characterization of the single components B-JM173 and B-C3, the nanocarriers should be assembled. Therefore, the three biotin-binding platforms avidin, streptavidin and neutravidin were tested for their binding capacities in a 4'-Hydroxyazobenzol-2-carbonsäure (HABA) assay together with Bingjie Gao (Max-Planck Institute for Polymer Research, Mainz) as part of an internship by the IGradU. All binding pockets of each platform were saturated with HABA, that can be replaced by B-JM173 due to its higher affinity. Gradual addition of B-JM173 leads to a decrease in absorbance at 500 nm indicating controlled and saturable binding of B-JM173 to the respective platform.

The binding pockets of avidin and neutravidin were saturated after the addition of four molar equivalents of B-JM173, while five molar equivalents of B-JM173 can be bound to streptavidin (Figure 10a). Knowing the binding capacity of each platform, the assembly protocols were optimized for binding one molar equivalent of B-C3 and three molar equivalents of breast cancer cell-targeting B-JM173 (Figure 10b).

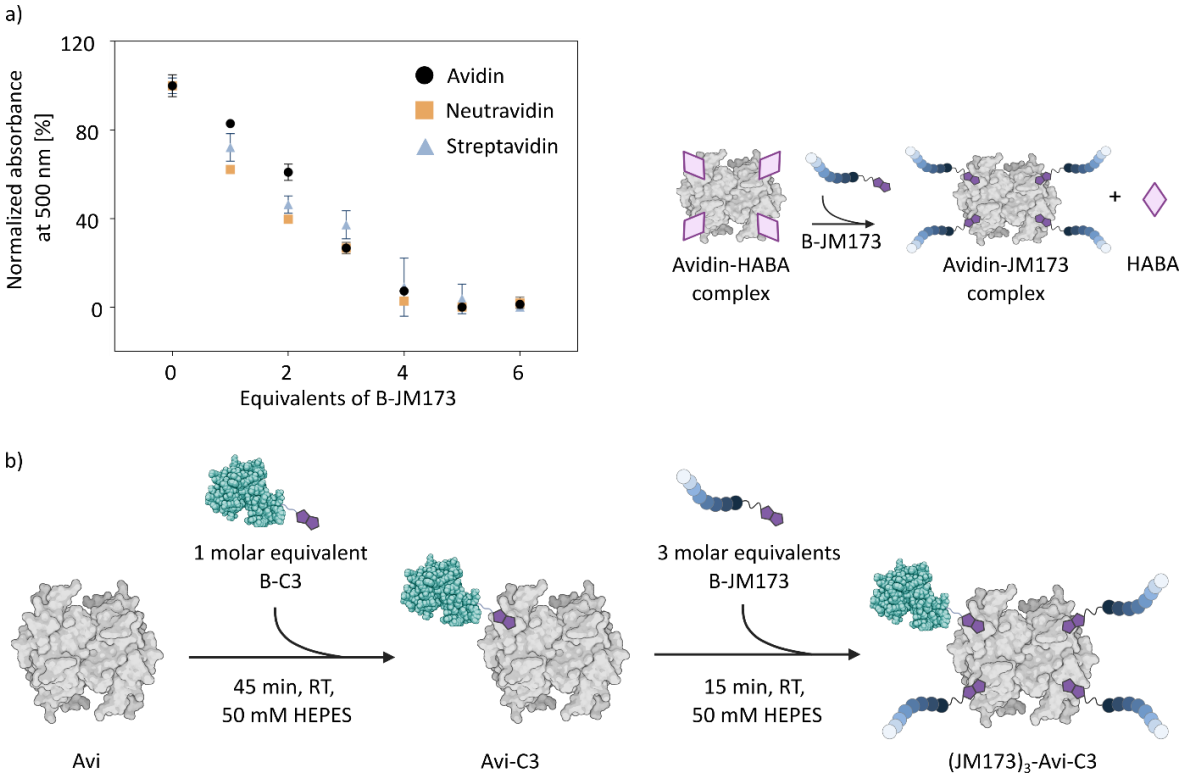


Figure 10: Optimizing the assembly of B-JM173 and B-C3 on different biotin-binding platforms. ***(a)*** *Schematic principle of the HABA assay for detection of the binding capacity of avidin (black, 1 molar equivalent B-JM173 per binding pocket), neutravidin (yellow, 1 molar equivalent B-JM173 per binding pocket) and streptavidin (blue, 4 molar equivalents of B-JM173 per binding pocket). This assay was performed together with Bingjie Gao (Max-Planck Institute for Polymer Research, Mainz) as part of an internship by the IGradU.* ***(b)*** *Schematic illustration of the in vitro assembly procedure of* $(JM173)_3$-^{BDP}*Avi-C3. In a two-step reaction biotinylated (purple) peptides and proteins can be assembled on the avidin platform. Therefore, bodipy-labelled avidin (*^{BDP}*Avi) is incubated for 45 min at room temperature (RT) with 1 molar equivalent of biotinylated C3 toxin (B-C3). In the second reaction (15 min, RT) 3 molar equivalents of biotinylated JM173 (B-JM173) are assembled to* ^{BDP}*Avi-C3. The final construct* $(JM173)_3$-^{BDP}*Avi-C3 is purified via ultrafiltration and re-buffered in 25 mM HEPES. The structures of avidin (grey, 1AVD) and C3 toxin (green, 1G24) originate from PDB, respectively [30,254]. Modified from [187], published with CC BY 4.0 license (https://creativecommons.org/licenses/by/4.0/), DOI: 10.3390/jfb16110399.*

To assess possible toxic effects of avidin and the cell targeting JM173 on cell viability, *in vitro* and *in vivo* toxicity studies were performed using the control construct $(JM173)_3$-Avi. For *in vitro* studies, the mammary gland adenocarcinoma MDA-MB231 cell line and a mouse model stage IV human breast cancer 4T1 cell line were treated for 72 h with

$(JM173)_3$-Avi, Avi or B-JM173. The cell viability was tested via MTS-assay not showing any negative effects compared to the viability of non-treated cells (Figure 11a). Based on these results, an *in vivo* toxicity study was performed in close collaboration with Prof. Gilbert Weidinger (Institute of Biochemistry and Molecular Biology, Ulm University). Therefore, zebrafish embryos were treated with rising concentrations of $(JM173)_3$-Avi, Avi or B-JM173 for 24 h while monitoring cytotoxicity, developmental toxicity, cardiotoxicity and neurotoxicity assigning the embryos into the groups "wildtype", "sublethal phenotype" or "dead/severely damaged phenotype" according to a standardized categorization system [187]. In concentrations higher than 5 µM the transporter $(JM173)_3$-Avi displayed weak, sub-lethal cell lysis that did not prevent or influence further development and survival of the zebrafish embryos (Figure 11b). Since $(JM173)_3$-Avi will be used as a cell-targeting unit for the C3 toxin and the cytotoxic effects of this toxin can already be monitored in a nanomolar range, the observed toxicity with high transporter concentrations above 5 µM does not restrict the intended use of the nanocarrier in this thesis.

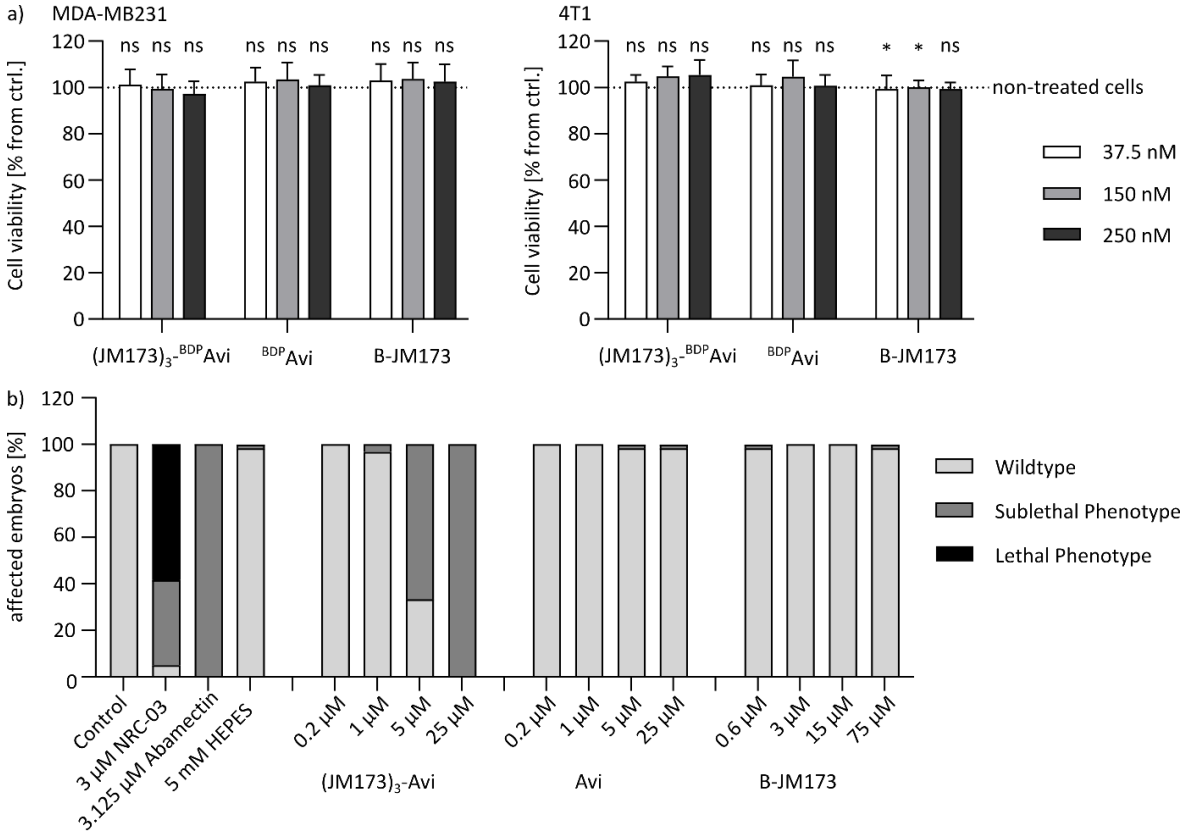


Figure 11: Toxicity studies on different breast cancer cell lines and zebrafish embryos. ***(a)*** *MDA-MB231 cells and 4T1 cells were treated with 37.5 nM, 150 nM or 250 nM of $(JM173)_3$-Avi or Avi for 72 h, respectively. The relative cell viability (% from non-treated cells) was assessed by an MTS assay and is depicted as mean ± SD of triplicates from three independent experiments. Statistical analysis was performed with a two-way ANOVA and Tukey's multiple comparisons test (ns*

*p ≥ 0.05, * p > 0.05).* ***(b)*** *In vivo toxicity studies on zebrafish embryos. Per group, 60 embryos were treated with the indicated concentration of $(JM173)_3$-Avi, Avi or B-JM173 for 24 h, respectively. Positive controls for developmental disorders were 3 µM NRC-03 for cytotoxicity and 3.125 µM Abamectin for neurotoxicity. HEPES served as solvent control. Following a standardized scoring system the embryos were monitored and categorized into the groups "wildtype" (bright grey), "sublethal phenotype" (dark grey) or dead/severely damaged phenotype (here stated as "lethal phenotype", black). [187]. Published with CC BY 4.0 license (https://creativecommons.org/licenses/by/4.0/), DOI: 10.3390/jfb16110399.*

3.1.2 $(JM173)_3$-Avi-C3 Selectively Binds to CXCR4 Expressing Cell Lines

Following the characterization of $(JM173)_3$-Avi-C3, the receptor specific binding of the supramolecular transporter to CXCR4 expressing cell lines was tested. First, CXCR4 expression levels of different cell lines were assessed via flow cytometric analysis of fluorescently labelled anti-CXCR4 antibody bound to the cell surface. As model cell lines, T-cell lymphoma SupT1 cells, epidermoid carcinoma A431 cells, MDA-MB231 cells and 4T1 cells were used. All cell lines show binding of the PE-labelled anti-CXCR4 antibody to their cell surface. The use of an isotype control antibody and an CXCR4 knockout SupT1 cell line (SupT1ΔCXCR4) excluded non-specific binding of the anti-CXCR4 antibody, verifying the CXCR4-expression in the tested cell lines (Figure 12).

Having confirmed the CXCR4 expression in the tested cell lines, they were incubated on ice with fluorescent bodipy- (BDP) labelled $(JM173)_3$-^{BDP}Avi-C3 or the controls $(JM173)_3$-^{BDP}Avi, ^{BDP}Avi-C3 or ^{BDP}Avi, respectively. The interaction of these constructs with the CXCR4 receptor was assessed via flow cytometry. It could be demonstrated that JM173-containing constructs lead to a shift in fluorescence intensity (FI) towards values two to four orders of magnitudes higher compared to the autofluorescence of the respective adherent cell line, indicating binding to the cell surface. The JM173-free control constructs ^{BDP}Avi-C3 and ^{BDP}Avi show no to little shift towards higher FI in A431 and MDA-MB231, while there is a shift of two orders of magnitude for the 4T1 cells detectable. Normalization of these shifts in FI to $(JM173)_3$-Avi-C3 reveals that in all adherent cell types the binding of JM173-free constructs to the cell surface is significantly lower compared to $(JM173)_3$-Avi-C3. The suspension SupT1 cells only bind the JM173-containing constructs, while the CXCR4 knockout cell line SupT1ΔCXCR4 does not show any binding of the tested nanocarriers. This indicates that the binding of $(JM173)_3$-Avi-C3 depends on the presence of CXCR4 and is specifically mediated by JM173 in all tested cell lines (Figure 13a). These results were strengthened by a flow cytometry-based competition assay, where fluorescently labelled JM173-containing constructs were added simultaneously to the cells with free JM173

peptide. The results revealed a significant reduction in nanocarrier-binding in the presence of excess JM173, further confirming the CXCR4 dependent cell surface binding of $(JM173)_3$-Avi-C3 (Figure 13b).

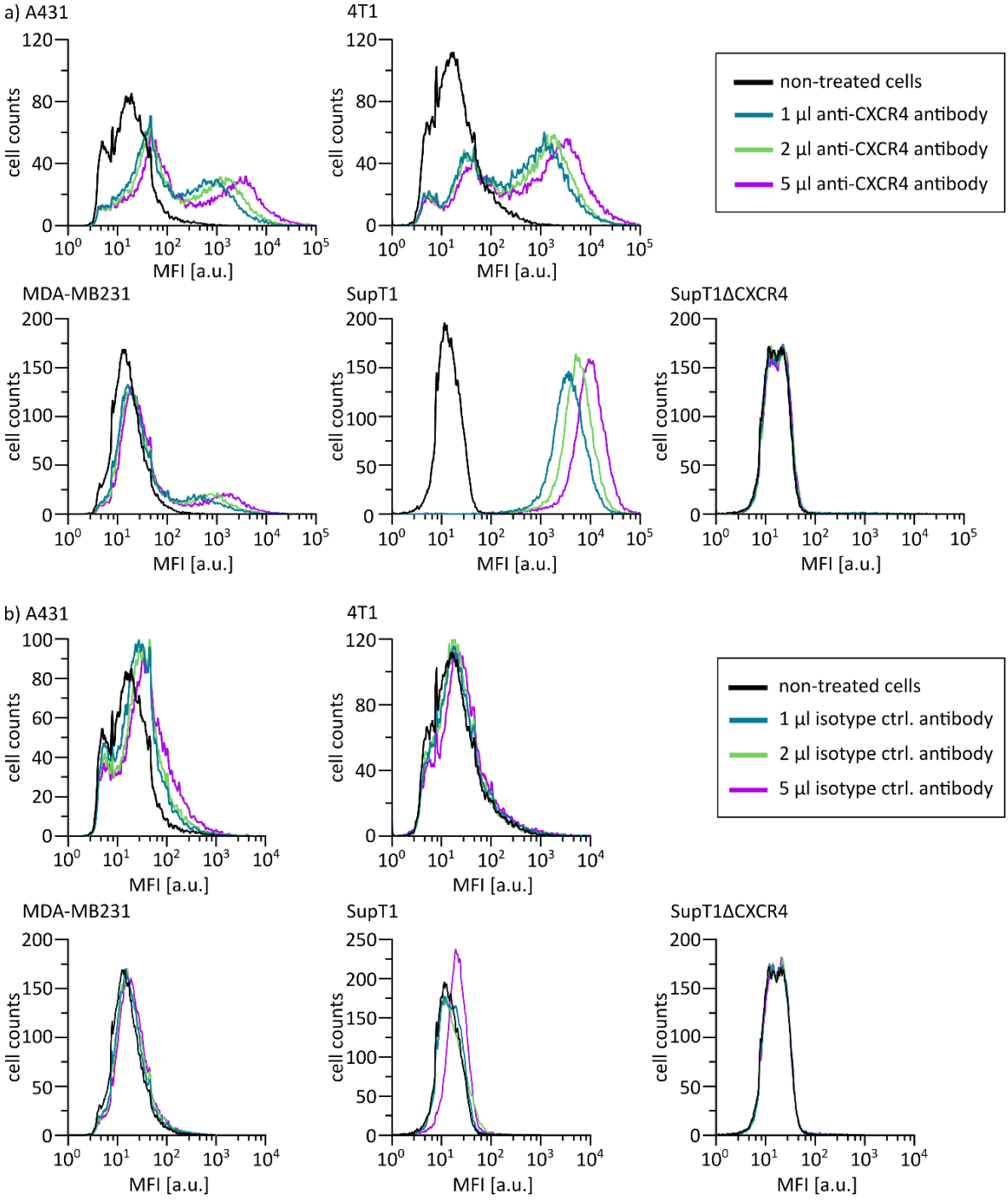


Figure 12: Flow cytometric analysis of CXCR4 expression level in different cell lines. ***(a)*** *A431 cells, 4T1 cells, MDA-MB231 cells, SupT1 cells and SupT1 cells with a CXCR4 knockout (SupT1ΔCXCR4) were incubated on ice with the indicated volumes of a fluorescently labelled anti-CXCR4 antibody to allow binding to the cell surface. After washing, antibody binding was detected via flow cytometry and is indicated as a right shift in mean fluorescence intensity (MFI) compared to the non-treated control. Data from three independent experiments.* ***(b)*** *Treatment of the cell lines with the indicated volumes of a fluorescently labelled rat IgG2a κ isotype control antibody. Washing and detection as described in (a). Data from three*

independent experiments. Adapted from [187], DOI: 10.3390/jfb16110399, published with CC BY 4.0 license (https://creativecommons.org/licenses/by/4.0/).

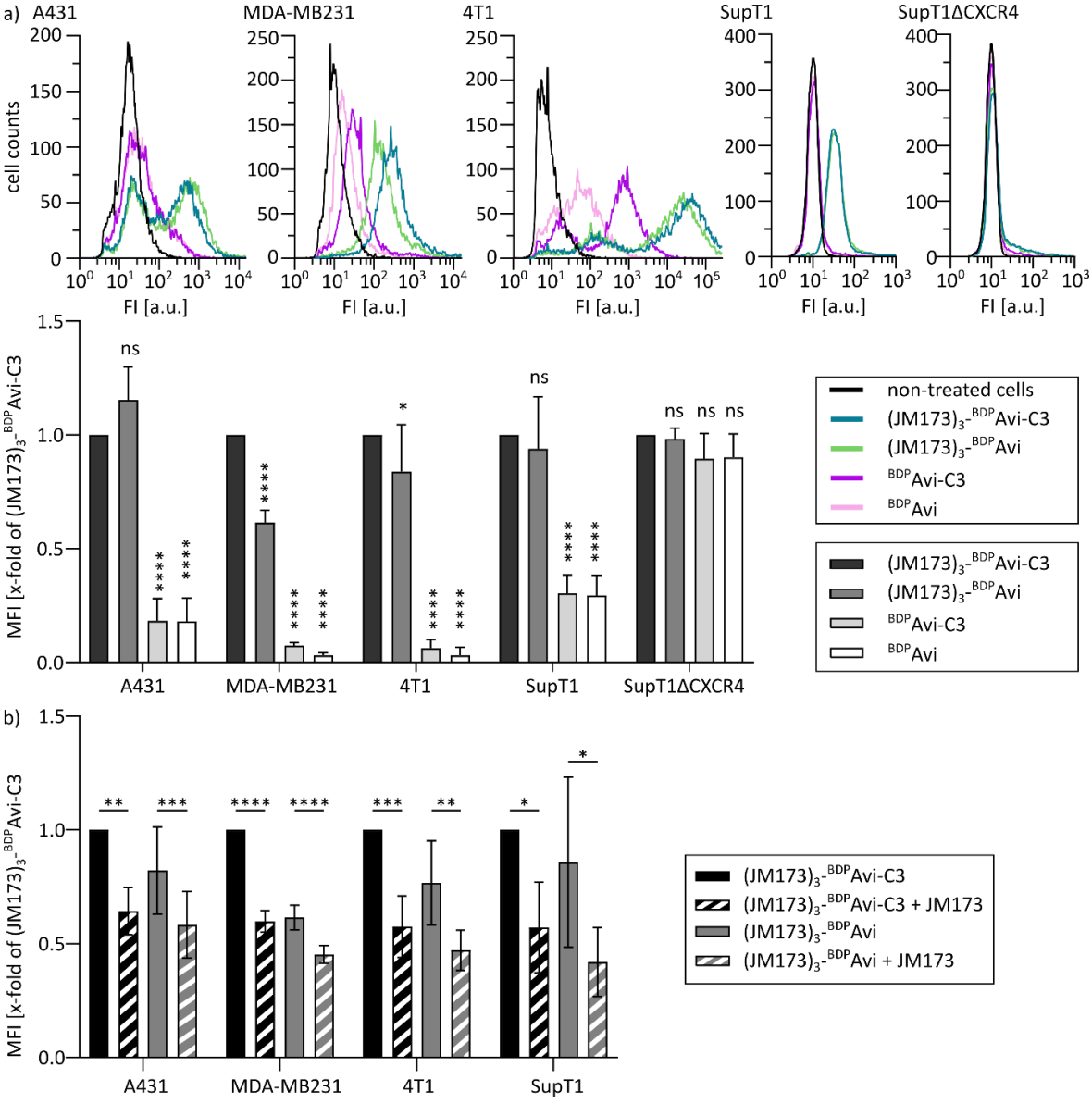


Figure 13: Flow cytometric analysis of the binding of $(JM173)_3$-^{BDP}Avi-C3 to CXCR4. ***(a)*** *Binding assay with 250 nM of $(JM173)_3$-^{BDP}Avi-C3, $(JM173)_3$-^{BDP}Avi, ^{BDP}Avi-C3 or ^{BDP}Avi incubated on ice with the respective cell type for 30 min or untreated cells as control. After washing twice, the binding was analyzed via flow cytometry. The representative histograms display single cell events plotted against their fluorescence intensity (FI) signal. Binding of the fluorescently labelled constructs to the cell surface is indicated by a right shift in FI compared to the autofluorescence of each non-treated cell type. Quantitative analysis shows the median FI (MFI) values normalized to $(JM173)_3$-^{BDP}Avi-C3 and confirms JM173-dependent and CXCR4-specific binding of the constructs to the cell surface. Significance was tested against $(JM173)_3$-^{BDP}Avi-C3 using one-way ANOVA combined with Dunn's multiple comparison test (ns $p > 0.05$, * $p < 0.05$, **** $p < 0.0001$).* ***(b)*** *Competition Assay with simultaneously added free JM173 peptide together with $(JM173)_3$-^{BDP}Avi-C3 or $(JM173)_3$-^{BDP}Avi. Data show the X-fold change of the MFI from three independent experiments compared to $(JM173)_3$-^{BDP}Avi-C3 ± SD. Significance was tested against the respective condition without free JM173 using one-way*

ANOVA combined with Dunn's multiple comparison test ($p < 0.05$, ** $p < 0.01$, *** $p < 0.001$, **** $p < 0.0001$). Adapted from [187], published with CC BY 4.0 license (https://creativecommons.org/licenses/by/4.0/), DOI: 10.3390/jfb16110399.*

3.1.3 JM173 Enhances the Uptake of C3 Toxin into CXCR4 Expressing Cell Lines

Since the C3 toxin is only poorly taken up into non-monocytic cells like breast cancer cells, the cell-targeting peptide JM173 should mediate the C3 uptake via the avidin platform into CXCR4 overexpressing cells. To verify this, the cell lines A431, MDA-MB231 and 4T1 each were incubated with the fluorescently labelled $(JM173)_3$-^{BDP}Avi-C3 or the controls $(JM173)_3$-^{BDP}Avi, ^{BDP}Avi-C3 or ^{BDP}Avi overnight. Nuclei were stained with Hoechst and the actin cytoskeleton with SiR actin to visualize the cells in fluorescence microscopy. While cells treated with ^{BDP}Avi-C3 and ^{BDP}Avi only show very weak and occasional signals in the bodipy-channel, JM173-containing nanocarriers entered the CXCR4 expressing cells significantly better (Figure 14).

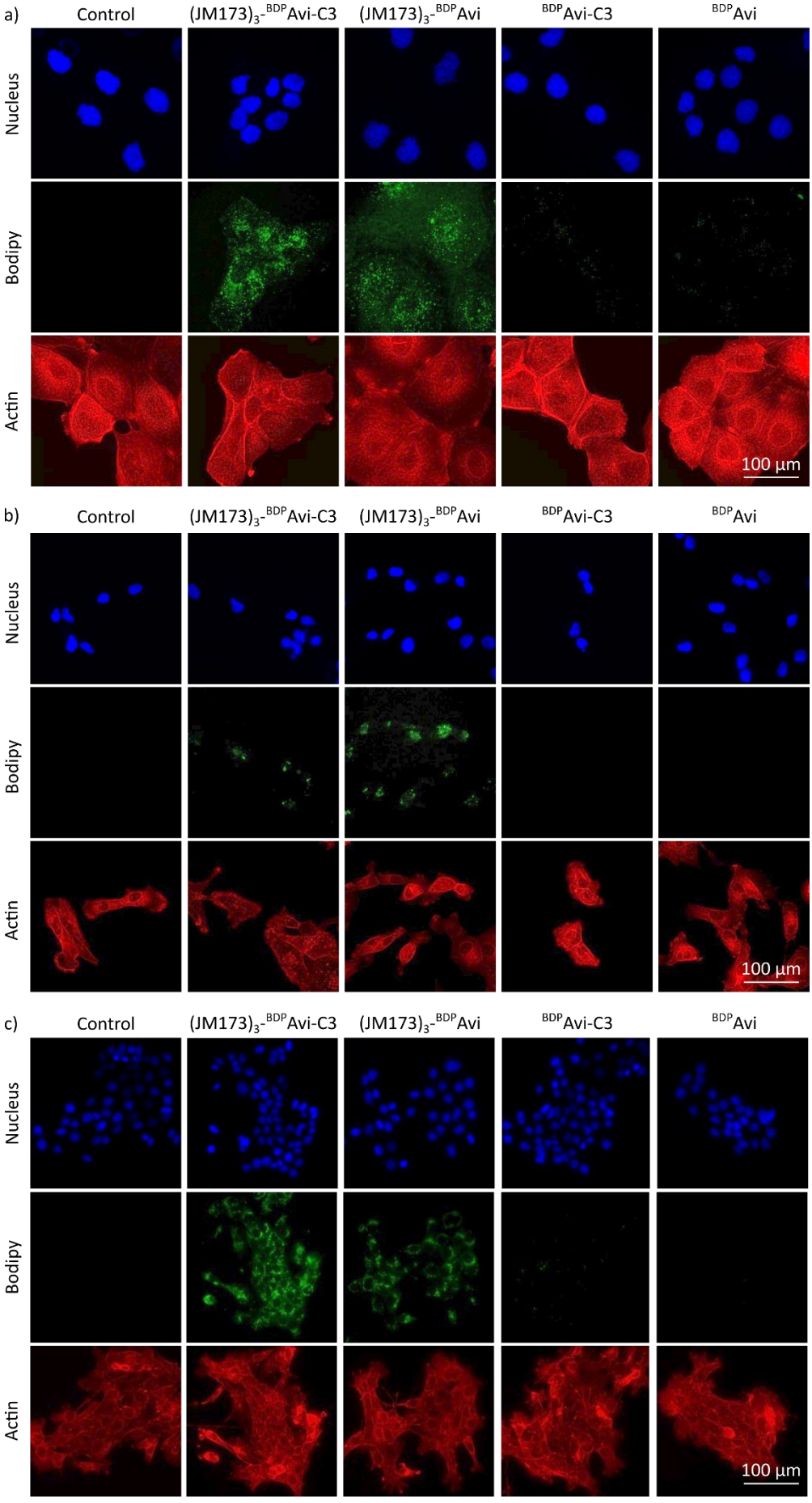

a)
Control
(JM173)3-BDPAvi-C3
(JM173)3-BDPAvi
BDPAvi-C3
BDPAvi
Nucleus
Bodipy
Actin
100 µm
b)
Control
(JM173)3-BDPAvi-C3
(JM173)3-BDPAvi
BDPAvi-C3
BDPAvi
Nucleus
Bodipy
Actin
100 µm
c)
Control
(JM173)3-BDPAvi-C3
(JM173)3-BDPAvi
BDPAvi-C3
BDPAvi
Nucleus
Bodipy
Actin
100 µm

Figure 14: Binding and uptake of $(JM173)_3$-Avi-C3 in CXCR4 expressing cells verified by fluorescence microscopy. A431 cells treated over night with 250 nM $(JM173)_3$-^{BDP}Avi-C3, $(JM173)_3$-^{BDP}Avi, ^{BDP}Avi-C3 or ^{BDP}Avi, respectively. Nuclei are stained with Hoechst33342 and imaged with the DAPI filter (blue), the actin cytoskeleton is stained with SiR actin and imaged with the Cy5 filter (red). Bodipy fluorescence is measured with the GFP filter of the Keyence BZ-X810 microscope (green). The image shows representative pictures from three independent experiments. The scale bar corresponds to 100 µm. ***(b)*** *MDA-MB231 cells treated and measured as indicated in a).* ***(c)*** *4T1 cells treated and imaged as indicated in a). 4T1 data are modified from [187], published with CC BY 4.0 license (https://creativecommons.org/licenses/by/4.0/), DOI: 10.3390/jfb16110399.*

This could also be verified by Western blotting and detection of the bodipy-labelled nanocarrier at an excitation wavelength of 500 nm. While only a little amount of ^{BDP}Avi-C3 could enter the 4T1 cells, an increased concentration dependent uptake of $(JM173)_3$-^{BDP}Avi-C3 could be observed. This is reflected by the increasing amount of BDP-labelled intracellular monomers of avidin ($^{BDP}Avi_{mono}$) (Figure 15a, lower panel). To monitor not only binding and uptake, but also the cytosolic release of active C3 toxin into the CXCR4 expressing breast cancer cells, a sequential ADP-ribosylation assay was performed. Therefore, $(JM173)_3$-^{BDP}Avi-C3, ^{BDP}Avi-C3 or C3-treated 4T1 cells were lysed and remaining non-modified toxin substrate was ADP-ribosylated in a second, labelled reaction. Hence, a weak signal in the Western blot analysis indicates a strong intoxication of living cells. $(JM173)_3$-^{BDP}Avi-C3 is efficiently internalized even at low concentrations of 37.5 nM, while wildtype C3 toxin can only affect intracellular Rho in concentrations higher than 150 nM (Figure 15a, middle panel). Summarized, ^{BDP}Avi-C3 and C3 toxin in high concentrations lead to modification of cytosolic Rho, but not as significant as the nanocarrier $(JM173)_3$-^{BDP}Avi-C3. The JM173 peptide enhances the uptake of C3 toxin into non-monocytic CXCR4 overexpressing cells, leading to intracellular release of active C3 from the nanocarrier.

To further study the effect of $(JM173)_3$-^{BDP}Avi-C3 on breast cancer cells, its influence on the proliferation of MDA-MB231 cells was tested in a live cell imaging setup. While non-treated cells show a sigmoidal growth curve over a timespan of five days, $(JM173)_3$-^{BDP}Avi-C3 and ^{BDP}Avi-C3 lead to a decrease in proliferation rate after 50 h incubation. After 100 h, the non-treated cells enter the stationary phase of growth. At this point, the cell number is circa 40% lower when treated with $(JM173)_3$-^{BDP}Avi-C3 and around 33% lower when treated with ^{BDP}Avi-C3. Wild-type C3 lowers the cell number after this time by only around 17% (Figure 15b). In summary, $(JM173)_3$-^{BDP}Avi-C3 enhances the uptake of active C3 toxin into the cytosol of CXCR4-overexpressing cells, leading to a reduction in cell proliferation.

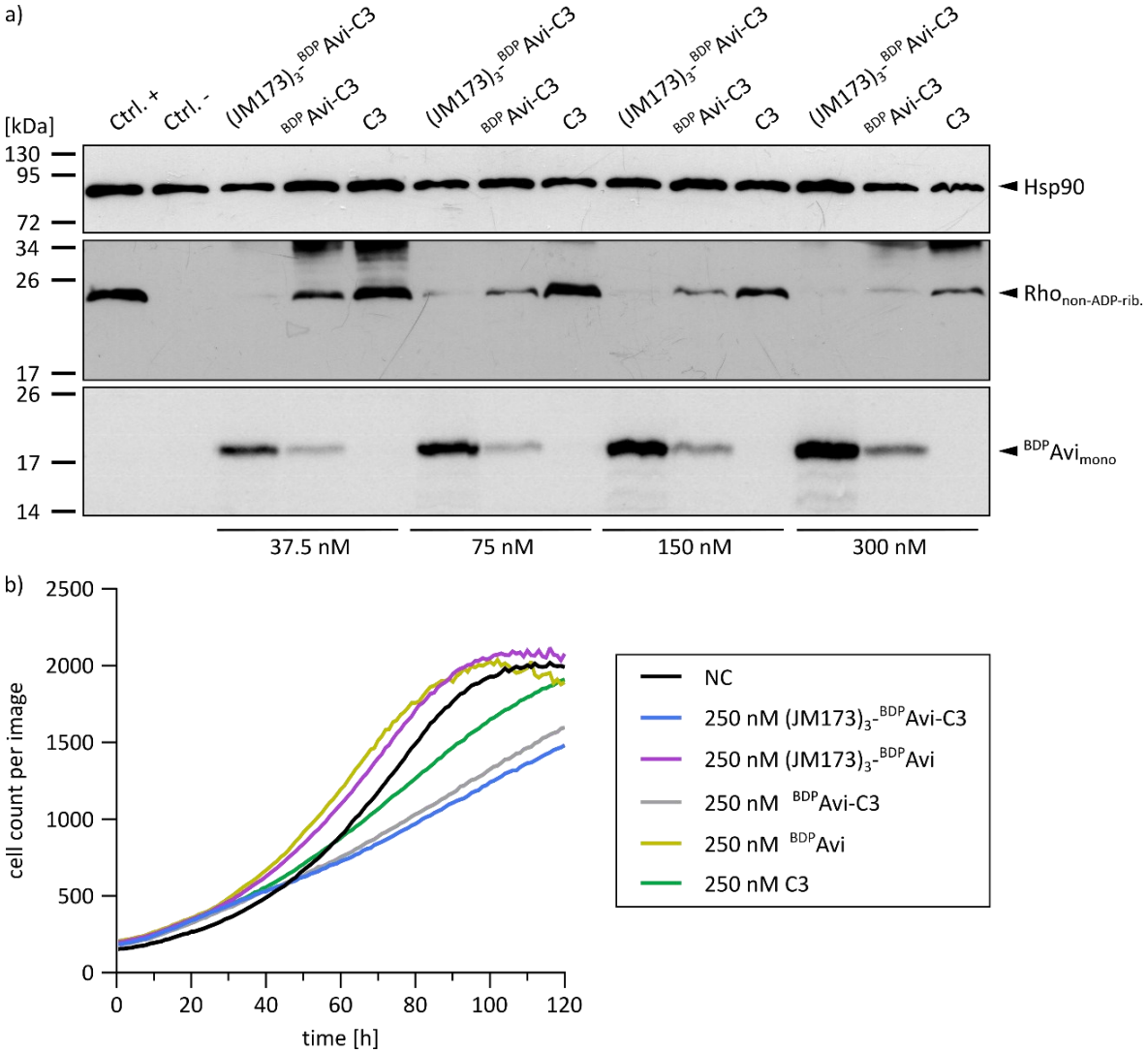


Figure 15: Influence of $(JM173)_3$-^{BDP}Avi-C3 on the intracellular ADP-ribosylation status of Rho and breast cancer cell proliferation. Sequential ADP-ribosylation assay after treatment of 4T1 cells with the indicated concentrations of $(JM173)_3$-^{BDP}Avi-C3, ^{BDP}Avi-C3 or C3 wildtype toxin for 8 h. The cells were washed, lysed and a second fluorescein labelled ADP-ribosylation reaction was performed. The Western blot membrane was first detected with an excitation wavelength of 500 nM to visualize the uptake of the bodipy-labelled constructs (lower panel, monomeric bodipy-labelled Avidin ($^{BDP}Avi_{mono}$), 17 kDa). Hsp90 served as a loading control (upper panel), while the fluorescein-labelled Rho protein ($Rho_{non\text{-}ADP\text{-}rib.}$, middle panel, 22 kDa) was detected via an anti-fluorescein antibody. Ctrl. +/- are non-treated cells with (+) or without (-) C3 toxin in the labelled reaction step. This experiment was performed together with Eva Haunschild, a former bachelor's student under my supervision. ***(b)*** *Live cell imaging after treatment of MDA-MB231 cells with the indicated constructs and controls for 120 h using the Incucyte®SX5. The graph displays the object count (cell number) per image at a given time point, showing a delayed proliferation after treatment with $(JM173)_3$-^{BDP}Avi-C3 and ^{BDP}Avi-C3. The figure is modified from [187], published with CC BY 4.0 license (https://creativecommons.org/licenses/by/4.0/), DOI: 10.3390/jfb16110399.*

3.1.4 $(JM173)_3$-Avi-C3 Inhibits Osteoclast Differentiation and Resorption Activity

After investigating the influence of $(JM173)_3$-^{BDP}Avi-C3 on breast cancer cells, its effect on the differentiation and resorption activity of osteoclasts should be tested. In very close collaboration with Melanie Haffner-Luntzer (Institute of Orthopaedic Research and Biomechanics, University of Ulm), RAW264.7 cells were differentiated to osteoclast-like cells with 25 ng/ml recombinant human receptor activator of NF-κB Ligand (rhRANKL) and 10 ng/ml recombinant human macrophage colony-stimulating factor (rhM-CSF) for five days in presence of $(JM173)_3$-^{BDP}Avi-C3, $(JM173)_3$-^{BDP}Avi, ^{BDP}Avi-C3, ^{BDP}Avi or JM173, respectively. After tartrate-resistant acid phosphatase (TRAP) staining, phase contrast microscopic pictures of whole wells were taken, and the multinuclear osteoclasts were counted, respectively. This assay revealed that all C3 toxin-containing constructs drastically reduce the number of formed osteoclasts and therefore decrease osteoclast differentiation (Figure 16a/c). To examine the influence of C3-containing constructs on the osteoclast resorption activity, RAW 264.7 cells were differentiated to osteoclast-like cells on human bone tissue before treatment with $(JM173)_3$-^{BDP}Avi-C3, $(JM173)_3$-^{BDP}Avi, ^{BDP}Avi-C3, ^{BDP}Avi or JM173, respectively. The non-resorbed, mineralized bone structures were stained with Von Kossa staining after ten days, revealing an inhibition of osteoclast resorption activity in cells treated with $(JM173)_3$-^{BDP}Avi-C3 (Figure 16b/d). In summary, the modular nanocarrier $(JM173)_3$-^{BDP}Avi-C3 has the expected inhibitory influence on osteoclast differentiation and resorption activity.

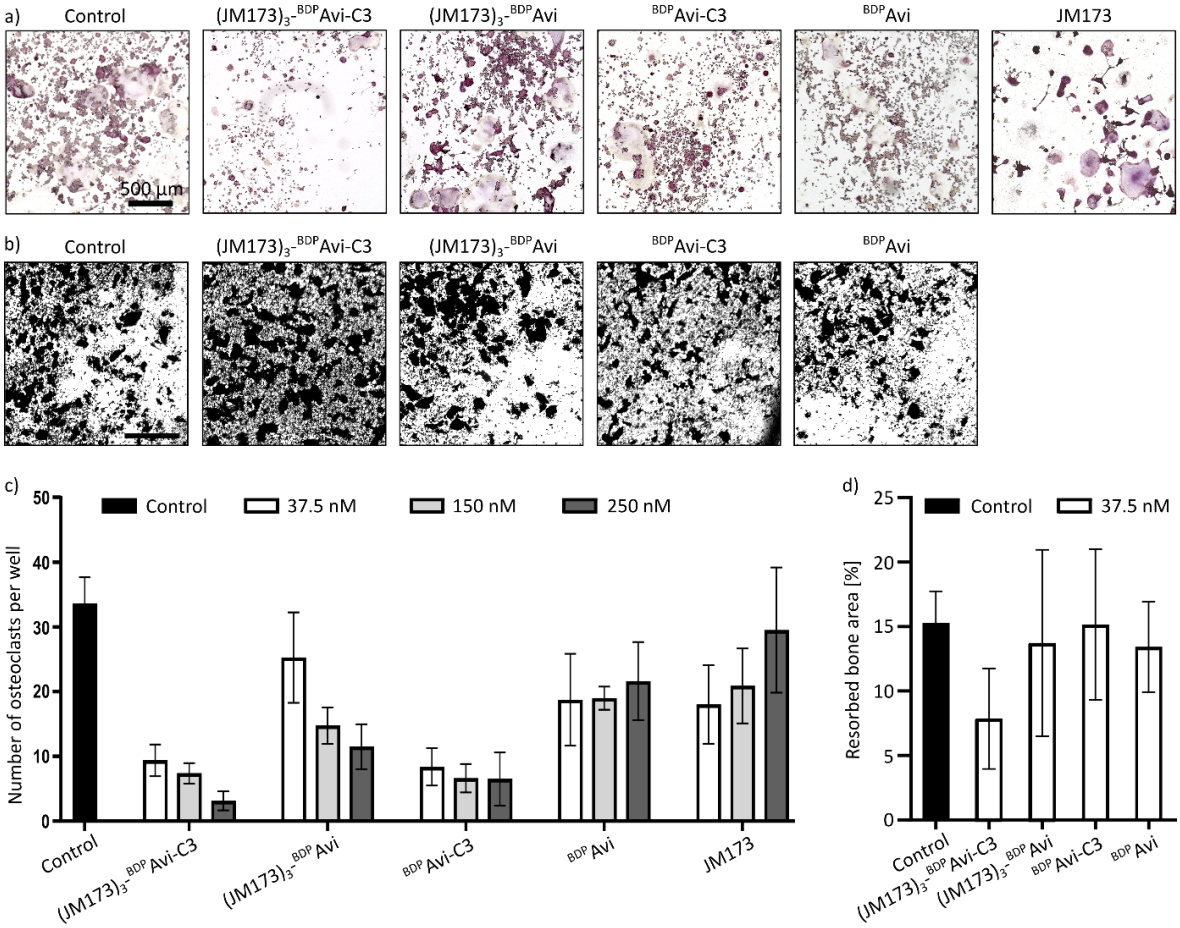


Figure 16: $(JM173)_3$-^{BDP}Avi-C3 decreases osteoclast differentiation and resorption activity. ***(a)*** *Differentiation of RAW264.7 cells into osteoclast-like cells with 25 ng/ml rhRANKL and 10 ng/ml rhM-CSF in absence (control) or presence of 37.5 nM, 150 nM or 250 nM $(JM173)_3$-^{BDP}Avi-C3, $(JM173)_3$-^{BDP}Avi, ^{BDP}Avi-C3, ^{BDP}Avi or JM173, respectively. Representative pictures show TRAP-stained cells after 5 days of treatment with 37.5 nM of the indicated nanocarriers and controls. The number and size of osteoclasts formed in the presence of C3 toxin decreases drastically. The scale bar corresponds to 500 µm and the experiment was performed as a biological triplicate.* ***(b)*** *RAW264.7 cells were seeded into an OsteoAssay human bone plate and differentiated and treated as indicated in a). After 10 days, mineralization was stained by Von Kossa Staining revealing non-resorbed areas in black and resorbed areas in white. All approaches were performed as a technical quadruplicate (control) or septuplicate (treatment conditions) and representative images of conditions treated with 37.5 nM of the respective substance are shown. $(JM173)_3$-^{BDP}Avi-C3 decreases the resorption activity of the osteoclast-like cells on human bone tissue. The scale bar corresponds to 500 µm.* ***(c)*** *Quantitative analysis of a) with n=24 (control) and n=8 (treatment conditions). The bar graph shows the number of osteoclasts formed per well ± SD. Conditions treated with C3 toxin-containing constructs lower the number of osteoclast-like cells. (d) Quantitative analysis of b) showing the resorbed bone area in percent ± SD. Only $(JM173)_3$-^{BDP}Avi-C3 lowers the resorption activity of osteoclasts [187]. Published with CC BY 4.0 license (https://creativecommons.org/licenses/by/4.0/), DOI: 10.3390/jfb16110399*

3.1.5 C3 toxin Promotes Osteoblastogenesis

Since in the bone niche of breast cancer metastasis not only overacting osteoclasts are present, the influence of $(JM173)_3$-^{BDP}Avi-C3 on osteoblasts should also be examined. Therefore, $(JM173)_3$-^{BDP}Avi-C3 and control constructs were added to osteoblastic MC3T3 cells during their differentiation process. The changes in the expression of established markers like alkaline phosphatase (AP) and runt-related transcription factor 2 (RUNX2) for early differentiation, osteocalcin (BGLAP) for late differentiation and the antigen KI67 as proliferation marker, were assessed by qPCR. Therefore, the accumulation of amplified DNA is measured in real time using a fluorescent signal that increases proportionally with the amount of product. The measured Ct value represents the cycle number at which the fluorescence crosses a defined threshold, meaning that samples with more starting template reach this threshold earlier. The Ct values of this qPCR were first normalized to the housekeeping gene of β2-Microglobulin (B2M) and then compared to a non-treated control condition, resulting in ΔΔCt values. A transformation of these values by $2^{-\Delta\Delta Ct}$ finally reflects how many times a gene is up- or downregulated compared to the control (Figure 17). C3-containing constructs lead to a ~10-fold upregulation in the expression of the early differentiation marker AP, whereas RUNX2 showed only a small upregulation upon C3 treatment. While the late differentiation marker BGLAP was not affected by C3, the proliferation marker KI67 was moderately upregulated in the presence of C3. Summarized, $(JM173)_3$-^{BDP}Avi-C3 and ^{BDP}Avi-C3 had a positive effect on early differentiation and proliferation of osteoblast progenitor cells.

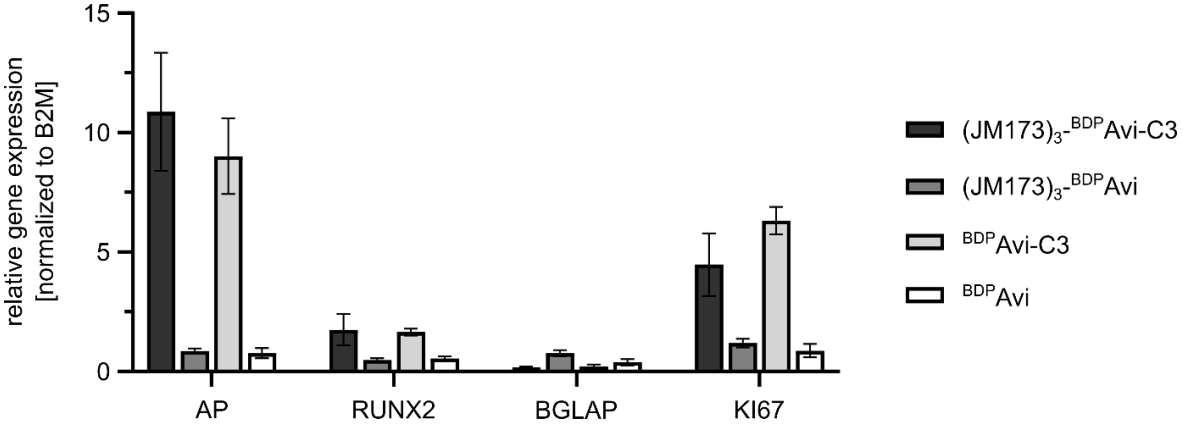


Figure 17: C3 toxin increases the gene expression of differentiation and proliferation markers in MC3T3 cells during osteoblastogenesis. Differentiation of MC3T3 osteoblast progenitor cells was induced by 10 mM β-glycerophosphate and 0.2 mM ascorbate-2-phosphate while simultaneously adding 37.5 nM $(JM173)_3$-^{BDP}Avi-C3, $(JM173)_3$-^{BDP}Avi, ^{BDP}Avi-C3 or ^{BDP}Avi. After ten days, the total RNA was isolated, and qPCR was performed for amplification of the housekeeping gene

encoding for β2-Microglobulin (B2M) for normalization, as well as the genes of interest alkaline phosphatase (AP) and runt-related transcription factor 2 (RUNX2) as early differentiation markers, osteocalcin (BGLAP) as late differentiation marker and the antigen KI67 as proliferation marker. Relative gene expression was calculated by the ΔΔCt method as described in [252]. Data represents a single experiment with six technical replicates per treatment condition and per tested gene, values are displayed as $2^{-\Delta\Delta Ct}$.

3.2 *Clostridium botulinum* C3 Toxin as Transport System for Cell Type-Selective Delivery of Cas9

In this thesis, the cargo protein Cas9 was genetically fused to $C3_{E147Q}$, a mutated non-toxic variant of the C3 toxin that acts as a cell type-selective transport system for monocytic cells. After cloning and expression of the fusion protein $C3_{E174Q}$_Cas9, the single subunits were tested for their activity. Ultimately, $C3_{E174Q}$_Cas9 should be used for cell type-selective genome editing in sgRNA-transfected cells or as a ribonucleoprotein (RNP) complex already harboring the sgRNA.

3.2.1 Cloning and Expression of C3_Cas9 and $C3_{E174Q}$_Cas9

The gene $Cas9^{NLS\text{-}His}$ encoding for Cas9, a nuclear localization sequence (NLS) and a 6x His-tag for purification was cloned from a plasmid using overhang primers with restriction sites for BamHI and NcoI. This 4194 bp insert was then ligated into a pCR-blunt vector, before digestion with the restriction enzymes, purification from agarose gel and T4 ligation into the C3bot1 or $C3bot1_{E174Q}$ containing backbones (Figure 18a). A colony PCR of transfected *E. coli* DH5α and sequencing (primers listed in Table 8) revealed the clones harboring the plasmid pEG-His1:C3bot1_$Cas9^{NLS\text{-}His}$ or pEG-His1:$C3bot1_{E174Q}$_$Cas9^{NLS\text{-}His}$ (Figure 18b). The purified plasmids were introduced into *E. coli* BL21 for expression and purification of C3bot1_$Cas9^{NLS\text{-}His}$ (short C3_Cas9) or $C3bot1_{E174Q}$_$Cas9^{NLS\text{-}His}$ (short $C3_{E174Q}$_Cas9, sequence depicted in Figure 23), respectively. Both proteins could be obtained with a low amount of impurities and in high concentrations around 10 mg/ml (Figure 18c).

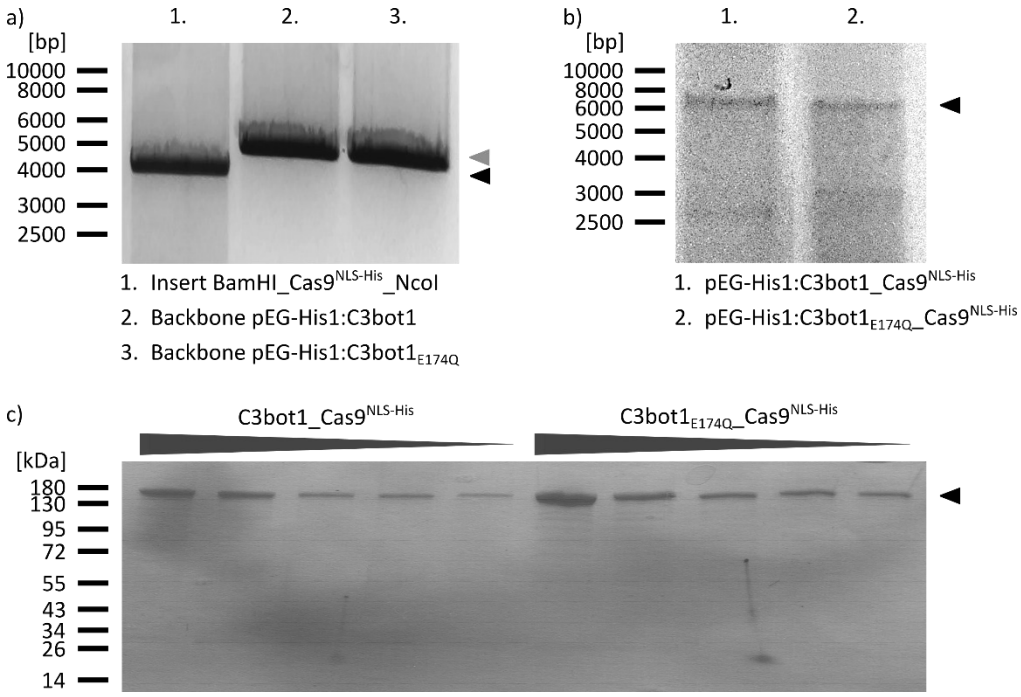


Figure 18: Cloning and expression of C3_Cas9 and C3$_{E174Q}$_Cas9. ***(a)*** *Agarose gel of the Cas9-harboring DNA-fragment with BamHI and NcoI restriction enzyme sites (lane 1., insert, black arrowhead, 4194 bp) and the plasmid backbones pEG-His1 containing C3bot1 or C3bot1$_{E174Q}$ (lane 2./3., grey arrowhead, 4964 bp each). The insert and the digested and dephosphorylated backbones were isolated from the gel for ligation.* ***(b)*** *Agarose gel after colony PCR of pEG-His1:C3bot1_Cas9$^{NLS-His}$ (lane 1.) or pEG-His1:C3bot1$_{E174Q}$_Cas9$^{NLS-His}$ (lane 2.) transfected E. coli DH5α identified clones with the correct insert (black arrowhead, 5189 bp) for amplification of the respective plasmid.* ***(c)*** *SDS-PAGE gel of C3bot1_Cas9$^{NLS-His}$ and C3bot1$_{E174Q}$_Cas9$^{NLS-His}$ expressed in and purified from E. coli BL21 (black arrowhead, 184 kDa). The applied protein volumes range from 0.2 µl to 0.005 µl (C3_Cas9$^{NLS-His}$) or from 0.15 µl to 0.0025 µl (C3$_{E174Q}$_Cas9$^{NLS-His}$).*

3.2.2 C3 Does Not Influence Cas9 Functionality in the Fusion Protein C3$_{E174Q}$_Cas9

Before assessing complex *in vivo* disease models, the ability of C3$_{E174Q}$_Cas9 to create a targeted gene knockout should be tested in proof-of-principle studies. Therefore, sgRNAs targeting the reporter gene *eGFP* (sgRNA^{eGFP}), the gene encoding for the lipolysis-stimulated lipoprotein receptor (LSR) (sgRNA^{LSR}) or for the monocytic cell surface marker CD33 (sgRNA^{CD33}) were designed. An *in vitro* cleavage assay was performed with the respective gene fragment isolated by PCR from an eGFP encoding plasmid (eGFP; 502 bp), from HCT-116 cell lysate (LSR; 1374 bp) or from THP-1 cell lysate (CD33; 905) (see chapter 2.2.9). Within this assay, RNP-complexation and the functional design of the sgRNAs, as well as the Cas9 enzyme activity could be examined (Figure 19a). For all approaches containing both, sgRNA and one of the Cas9-variants Cas9, C3_Cas9 or C3$_{E174Q}$_Cas9 RNP complexation could be observed, indicated by fainting of the sgRNA band at around 100 bp. Furthermore, in all of these samples the RNP complexes led to comparable cleavage of

the respective gene fragment into smaller DNA strands of around 340 bp and 160 bp for *eGFP* (Figure 19a, upper panel), 1050 bp and 330 bp for *LSR* (Figure 19a, middle panel) or 620 bp and 280 bp for *CD33* (Figure 19a, lower panel). This demonstrates that the genetic fusion of C3 or $C3_{E174Q}$ to Cas9 did not alter its DNA cleavage activity or its ability for sgRNA binding. Additionally, the specificity of the designed sgRNAs was shown by combining it with $C3_{E174Q}$_Cas9 and different non-targeting gene fragments, where no DNA cleavage could be observed (Figure 19b).

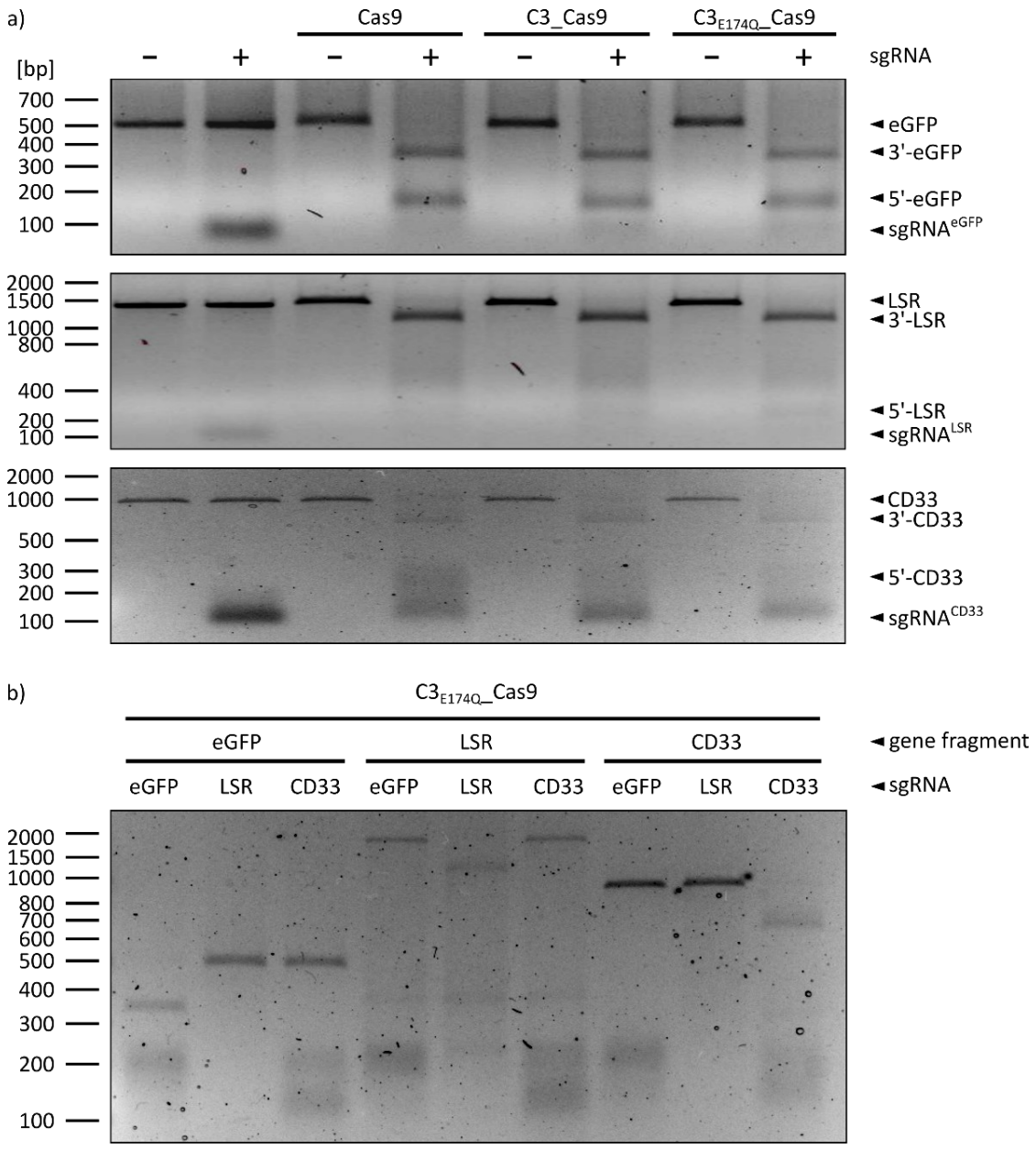


Figure 19: Cleavage assay with gene fragments of eGFP, LSR and CD33 treated with Cas9, C3_Cas9 and $C3_{E174Q}$_Cas9 and the respective targeting or non-targeting sgRNA. ***(a)*** *Cas9, C3_Cas9 or $C3_{E174Q}$_Cas9 were incubated with (+) or without (-) sgRNA targeting a gene fragment of eGFP (502 bp, upper panel), LSR (1374 bp, middle panel) or CD33 (905 bp, lower panel). Where RNP complexation of Cas9-variants and the targeting sgRNA ($sgRNA^{eGFP}$, $sgRNA^{LSR}$ or $sgRNA^{CD33}$, ~100 bp*

each) occurs, the respective gene fragment is cut. The expected cleavage products of eGFP have a size of ~340 bp (3'-eGFP) and ~160 bp (5'-eGFP), the products of LSR cleavage of ~1050 bp (3'-LSR) and ~330 bp (5'-LSR) and the products of CD33 cleavage ~620 bp (3'-CD33) and ~280 bp (5'-CD33). The figure shows ethidium bromide-stained agarose gels performed after the respective cleavage assay. ***(b)*** *Specificity of eGFP, LSR or CD33 gene fragment cleavage by RNP complexes formed by $C3_{E174Q}$_Cas9 together with sgRNA targeting eGFP, LSR or CD33, respectively. Agarose gel electrophoresis after performing the cleavage assay as described in (a).*

3.2.3 Cas9 Does Not Influence C3 Functionality in the Fusion Protein $C3_{E174Q}$_Cas9

Since the uptake mechanism of C3 into monocytic cells is widely unknown, it needs to be examined whether the fusion of the large protein Cas9 interferes with the ability of C3 or $C3_{E174Q}$ to enter the cytosol of monocytic cells. Therefore, cells were treated with C3_Cas9, $C3_{E174Q}$_Cas9 or DyLight^{488} labelled versions of the proteins (see section 2.2.11 and Figure 24) and examined visually by light- and fluorescence microscopy (see sections 2.2.2 and 2.2.15) (Figure 20).

J774A.1 cells normally show a round to slightly elongated cell shape. The intoxication of these cells with C3 toxin leads to the formation of long protrusions, condensed cell bodies, and membrane blebbing that can be microscopically monitored. First, the binding and uptake of the fusion proteins into J774A.1 cells should be monitored by fluorescence microscopy. Therefore, the cells were treated with 300 nM of DyLight^{488} labelled C3_Cas9^{488} or $C3_{E174Q}$_Cas9^{488} for 24 h before fixation and staining of cell nuclei and the actin cytoskeleton. Both fusion proteins can be detected in the DyLight^{488} channel indicating successful binding to or internalization into the J774A.1 cells. Since the microscope used does not provide confocal measurements, these two mechanisms cannot be further distinguished. However, the actin cytoskeleton of cells treated with the fusion protein harboring the active C3 variant shows the typical C3-induced morphological changes (C3-mrophology) confirming cytosolic uptake of C3_Cas9 (Figure 20a).

To further compare the intoxication process of C3_Cas9 with wildtype C3 toxin, J774A.1 cells were treated with 100 nM or 300 nM of C3_Cas9, $C3_{E174Q}$_Cas9 or wildtype C3 toxin, respectively and light microscopic pictures were taken up to 24 h post intoxication. It was expected that cells treated with the enzymatically inactive $C3_{E174Q}$_Cas9 do not show morphological changes compared to cells treated with wildtype C3. However, $C3_{E174Q}$_Cas9 lead to changes in cell morphology compared to non-treated cells which did not fit the

typical C3-morphology. C3_Cas9 treated cells exhibited a larger proportion of cells with C3-morphology than the ones treated with wildtype C3 toxin already after around 7 h (Figure 20b). This indicates that C3 is not only capable of transporting Cas9 into macrophages, but the fusion could also enhance its uptake into the cytosol of J774A.1 macrophages.

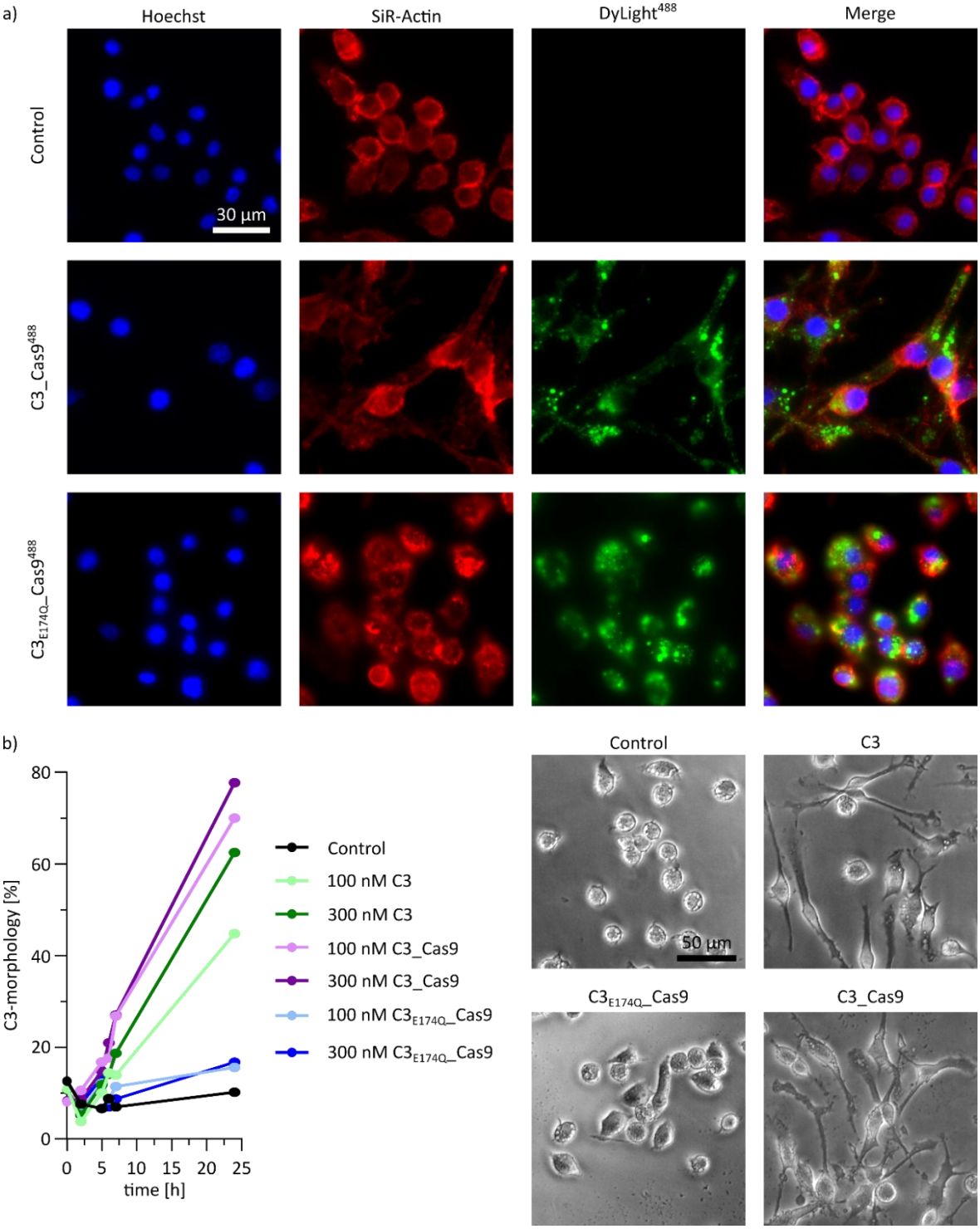


Figure 20: C3_Cas9- or $C3_{E174Q}$_Cas9-treated J774A.1 macrophages analyzed by light- and fluorescence microscopy. ***(a)*** *Representative fluorescence microscopy images after treatment of J774A.1 cells with 300 nM of DyLight^{488} labelled C3_Cas9 (C3_Cas9^{488}) and $C3_{E174Q}$_Cas9 ($C3_{E174Q}$_Cas9^{488}) for 24 h. The control cells were left untreated. After fixation,*

nuclei were stained with Hoechst33342 and imaged with the DAPI filter (blue), the actin cytoskeleton was stained with SiR actin and imaged with the Cy5 filter (red). DyLight^{488} fluorescence was measured with the GFP filter of the Keyence BZ-X810 microscope (green). The image shows representative pictures from three independent experiments. The scale bar corresponds to 30 µm. ***(b)*** *J774A.1 cells were treated with 100 nM or 300 nM of C3_Cas9, C3$_{E174Q}$_Cas9 or C3 wildtype toxin or left untreated as control for 24 h, respectively. Light microscopic images were taken, and the cells were categorized into healthy cells and cells with C3-morphology characterized by long protrusions and condensed cell bodies. The ratio of cells showing C3-morphology over time is displayed in the graph for each treatment condition. This assay was performed in three independent experiments, each with triplicates summarized in the graph. The representative pictures show the morphology of the cells 24 h after treatment with 300 nM of the indicated protein. The scale bar measures 50 µm.*

To evaluate not only effects of the fusion proteins on the morphology of monocytic cells, the level of Rho ADP-ribosylation upon treatment of cells with either C3_Cas9 or C3$_{E174Q}$_Cas9 was analyzed in a sequential ADP-ribosylation assay (Figure 21). Therefore, murine J774A.1 macrophages, as well as human THP-1 monocytes and THP-1 M0 macrophages were treated with wild type C3 toxin, C3_Cas9, C3$_{E174Q}$_Cas9 or an RNP complex of C3_Cas9 and sgRNA (C3_Cas9:sgRNA), while untreated cells served as control (ctrl.). Residual toxins or fusion proteins were removed, and the cells were lysed. In a sequential intoxication of all lysates with wild type C3, only non-modified Rho can be tagged with biotin that is transferred from the co-substrate biotin-NAD$^+$. When detecting the biotin-labelled Rho (Rho$_{non\text{-}ADP\text{-}rib.}$), strong signals in the Western Blot correlate with weak intoxication of living cells. Therefore, the strongest signals were expected in the untreated control cells, as well as in the cells treated with C3$_{E174Q}$_Cas9 due to the lack of C3 enzyme activity. This expectation was confirmed in all tested cell types. Furthermore, the levels of ADP-ribosylation activity of C3_Cas9 and the RNP complex were similar to the wild type C3 toxin indicating that the cytosolic uptake is not negatively affected by the fusion of C3 to Cas9 or the additional binding to sgRNA. Comparing the three used cell types, THP-1 M0 macrophages seem to take up C3 toxin-variants most efficiently, followed by J774A.1 cells.

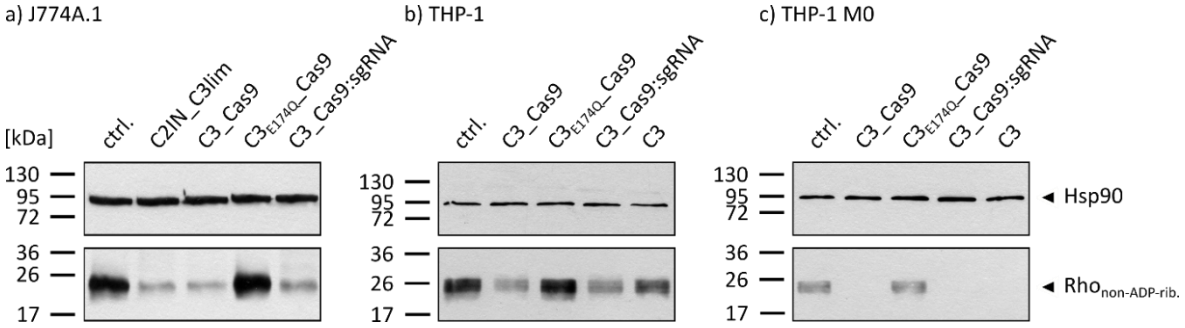


Figure 21: Analysis of the ADP-ribosylation status of Rho in various macrophage-like cells after incubation with C3_Cas9 $C3_{E174Q}$_Cas9, C3_Cas9:sgRNA RNP complex or C3 wild-type variants. ***(a)*** *J774A.1 cells were intoxicated with 300 nM C3_Cas9, $C3_{E174Q}$_Cas9, C3_Cas9:sgRNA RNP complex or 100 nM C2IN_C3lim for 7 h to allow Rho modification or left untreated as control (ctrl.). Residual treatments were removed, and the cell lysates were treated a second time with 25 pmol C2IN_C3lim and 250 pmol biotin-NAD^+ as co-substrate. Biotin-labelled Rho ($Rho_{non\text{-}ADP\text{-}rib.}$) from the sequential intoxication was detected by peroxidase-coupled streptavidin (Strep-POD, 1:5000 in PBS-T). Therefore, a strong signal in the lower panel corresponds to a weak intoxication of living cells. Hsp90 in the upper panel was detected as a loading control (anti-Hsp90 alpha/beta antibody, 1:500 in PBS-T; HRP coupled goat anti-mouse antibody, 1:2500 in PBS-T).* ***(b)*** *THP-1 monocytes were treated as indicated in a), but with 300 nM C3bot1 (C3) instead of C2IN_C3lim.* ***(c)*** *THP-1 cells were differentiated into THP-1 M0 macrophages by adding 100 nM PMA for 48 h. The cells were then treated as indicated in b). All experiments shown were performed as independent biological triplicates.*

Summarized, C3_Cas9 and $C3_{E174Q}$_Cas9 reached the cytosol of monocytes and macrophages comparable to the C3 wildtype toxin. Therefore, the fusion of C3 to Cas9 did not negatively affect the C3-mediated binding to cells or its uptake into the cytosol.

3.2.4 $C3_{E174Q}$_Cas9 Reaches the Nucleus of Monocytic Cells

In order to use $C3_{E174Q}$_Cas9 as a cell type-selective gene editing tool, it not only has to reach the cytosol, but also the nucleus of the target cell. To verify nuclear translocation initiated by the NLS at the C-terminus of $C3_{E174Q}$_Cas9, THP-1 monocytes and THP-1 M0 macrophages treated with the fusion protein were fractioned into cytosolic and nucleic compartments before Western Blot analysis was performed. Fractionation was confirmed by detection of the housekeeping proteins Hsp90 (Figure 22, upper panels) and LaminB1 (Figure 22, middle panels), specific for the cytosolic or nuclear fraction, respectively. $C3_{E174Q}$_Cas9 could be localized in both fractions to equal amounts with increasing band intensity towards higher concentrations (Figure 22, lower panels).

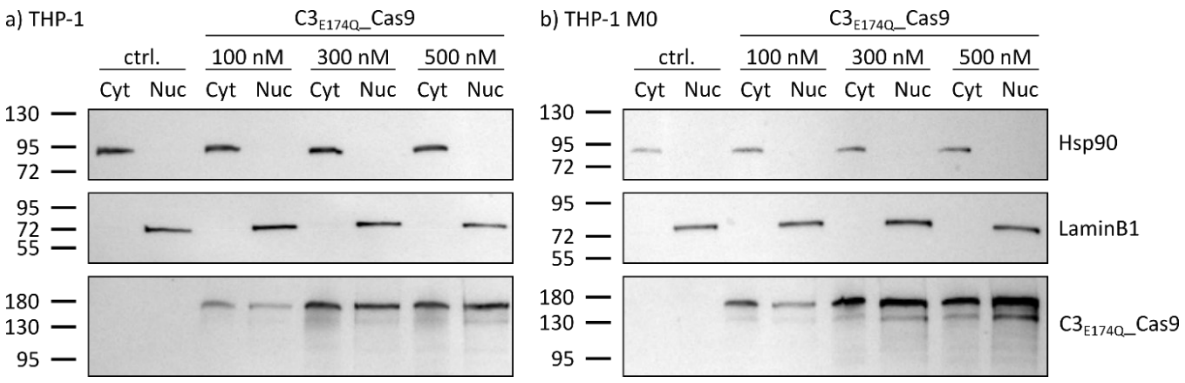


Figure 22: $C3_{E174Q}$_Cas9 enters cytosol and nucleus of monocytes and macrophages. ***(a)*** *THP-1 monocytes were treated with 100 nM, 300 nM or 500 nM $C3_{E174Q}$_Cas9 for 4 h or left untreated as control (ctrl.). The cells were separated into a cytosolic (Cyt) and a nuclear (Nuc) fraction (section 2.2.10), respectively and SDS-PAGE and Western Blot were performed. The fraction-specific housekeeping proteins Hsp90 (upper panel, anti-Hsp90 alpha/beta antibody, 1:500 in PBS-T, 90 kDa) and Lamin B1 (middle panel, anti-LaminB1 mouse monoclonal antibody, 1:10000 in PBS-T, 66 kDa) served as controls for proper separation of cytosolic and nuclear compartment, respectively. $C3_{E174Q}$_Cas9 was detected by an anti-Cas9 antibody (lower panel, 1:1000 in PBS-T, 185 kDa) in all fractions. Imaging was performed in the iBright™ CL1500 imaging system after incubation with an HRP coupled goat anti-mouse antibody (1:2500 in PBS-T).* ***(b)*** *THP-1 M0 macrophages were treated, fractionated and the indicated proteins were detected as described in a). This assay was performed in three independent biological replicates with similar results.*

Take together, these results indicate that $C3_{E174Q}$_Cas9 is able to reach not only the cytosol, but also the nucleus of THP-1 monocytes and THP-1 M0 macrophages. This makes it a promising candidate for monocyte/macrophage-selective gene editing.

4 Discussion

Traditional small-molecule medications are typically synthetic low-molecular-weight compounds with well-defined chemical structures. The arising complex, larger molecules like proteins, peptides, antibodies or RNA- and DNA-based molecules are summarized as biologics and often exhibit higher target affinity compared to small molecules [255]. One milestone in the development of protein engineering was the approval of etanercept (commercial name Enbrel®) for treatment of rheumatoid arthritis in 1998 which was also considered as the first therapeutic fusion protein [256]. Since then, not only the use of antibodies, but also of peptides or proteins as biologics emerged. Due to the high molecular weight and the physicochemical properties of proteins, they are not able to cross cellular membranes by passive diffusion. Therefore, their use is often limited to the modulation of disease-relevant receptors, rather than targeting intracellular substrates. To retarget therapeutic proteins to the cells of interest, transport systems were established that either rely on the genetic modification of the biologic itself or on the fusion to a vehicle [257]. This thesis highlights the potential of the *Clostridium botulinum* C3 toxin not only as a transport system for other pharmacologically active proteins but also as a biologic itself.

4.1 The Potential of *Clostridium botulinum* C3 Toxin as a Biologic in Cancer Treatment

The actin cytoskeleton of eucaryotic cells plays a central role in intracellular vesicle trafficking, maintaining cell shape, polarity or movement. Therefore, soluble globular actin proteins (G-actin) polymerize into polarized filamentous actin (F-actin), allowing rapid directional growth and remodeling of the cytoskeleton [258]. Dysregulation of actin organization or actin-binding proteins can induce malignancies like uncontrolled proliferation, increased motility and invasiveness leading to the metastatic behavior of cancer cells. Therefore, targeting the actin cytoskeleton and its regulators represents a promising strategy to diminish the growth of cancer cells [259]. Rho GTPases are the major regulators of the actin cytoskeleton [33,36]. The downregulation of Rho activity in mouse embryonic fibroblasts by overexpressing Rho inactivating GAP lead to an inhibition of actin filament formation, finally resulting in decreased cell motility, cell spreading and cell-to-cell adhesions [260]. Further, treatment of mice with the Rho-associated protein kinase (ROCK) inhibitor Y-27632 lead to interruption of Rho downstream signaling and to reduction of

prostate- and lung cancer by inhibiting transendothelial migration, tissue invasion, and cancer cell growth [261,262].

A well established and highly specific Rho inhibitor is the *Clostridium botulinum* C3 toxin. It mono-ADP ribosylates especially RhoA, RhoB and RhoC, leading to constant inactivation of these small GTPases [46–48]. This results in actin dysregulation and reduced actin-mediated cell functions such as migration and proliferation [51,52]. Based on these findings, this thesis aims to utilize the C3 Rho inhibitor in the context of breast cancer metastases in the bone niche. Since C3 is preferentially taken up by monocyte-derived cells, the modular bioconjugate $(JM173)_3$-Avi-C3 is generated, characterized and tested for the targeted transport of C3 into breast cancer cells and the inhibition of osteoclast formation and resorption activity.

4.1.1 Specific Binding of $(JM173)_3$-Avi-C3 to CXCR4 Expressing Cell Lines

Breast cancer cells overexpress distinct cell surface markers that can be used for targeted drug delivery. The most prominent ones are the human epidermal growth factor receptor 2 (HER2), the estrogen receptor (ER) and the progesterone receptor (PR) [263]. Up to 20% of all women diagnosed with breast cancer can be categorized as triple negative, expressing none of the cell surface markers mentioned above. This subtype of cancer often occurs in young females and is linked to high morbidity and mortality. The triple negative breast cancer cells are highly proliferative and invasive and show early metastatic spread into the central nervous system or internal organs such as liver, lungs or bones [264]. Since these cells are highly heterogenous in their expression profile of intracellular signaling pathways and do not express ER, PR or HER2 on their cell surface, targeted treatment options are limited. Currently, surgery combined with systematic chemotherapy using taxanes is considered as the standard therapy. Nevertheless, due to the development of drug resistance an early and rapid relapse of the triple negative breast cancer metastases can be observed [265]. This study aims to overcome these limitations by examining a new targeting strategy for the treatment of breast cancer metastases by retargeting the C3 toxin to the chemokine receptor CXCR4. While CXCR4 is overexpressed on ductal carcinoma cells, normal breast epithelium has no or only a low level of CXCR4 expression, making it a suitable target strategy for the abnormal cancer cells [158,266]. To retarget the C3 toxin into the CXCR4 overexpressing cancer cells, C3 and the CXCR4 antagonist JM173 were

combined on an avidin platform. Therefore, C3 toxin was successfully biotinylated while preserving an enzyme activity comparable to the wildtype C3 toxin (Figure 9). The assembly of avidin, biotinylated C3 and biotinylated JM173 was controlled by a two-step reaction in a stoichiometric ratio of 1:1:3, resulting in the nanocarrier $(JM173)_3$-Avi-C3 (Figure 10). This ratio has already been tested successfully in another study from our group, where somatostatin was assembled on Avi-C3 to retarget the C3 toxin into somatostatin receptor overexpressing cancer cells. This complex was able to efficiently inhibit tumor growth not only in the A549 cell line but also in a preclinical model of treatment-resistant non-small cell lung carcinoma xenografts [174].

The specific binding of $(JM173)_3$-Avi-C3 to the cell surface of CXCR4 expressing cell lines could be verified by flow cytometry, while cell types exhibiting a CXCR4 knockout were not able to bind the nanocarrier (Figure 12). Furthermore, addition of free JM173 peptide decreased the amount of cell bound $(JM173)_3$-Avi-C3 on CXCR4-expressing cells, indicating competitive binding and highlighting the CXCR4 specificity of JM173 binding (Figure 13). Other common CXCR4 antagonists like the FDA approved AMD3100 (Plerixafor) or TC14012 show tendencies to not only bind to CXCR4 but also interact with the atypical chemokine receptor 3 (CXCR7) [267,268]. There, they act as potent agonists leading to β-arrestin recruitment that shifts the CXCL12 axis towards β-arrestin-driven cellular reactions rather than shutting down the CXCR4/CXCL12 signaling pathway. This can finally lead to activation of different kinases promoting cell survival, proliferation, migration and angiogenesis [269–271]. Since JM173 origins from EPI-X4 which exclusively targets CXCR4, these adverse effects based on CXCR7 cross-reactivity can be excluded [272]. This makes JM173 a promising peptide not only for CXCR4 inhibition but also for retargeting C3 into metastatic breast cancer cells for Rho modulation.

4.1.2 Retargeting C3 Toxin into Metastatic Breast Cancer Cells by $(JM173)_3$-Avi-C3

To inhibit tumor growth and survival, it is crucial to introduce the C3 toxin into the cytosol of the cancer cells. Multiple studies showed that C3 toxin is preferentially taken up by monocytic cells, while other cell types are rather poorly affected by C3 intoxication [63,64,66]. Here, the JM173-dependent binding and uptake of $(JM173)_3$-Avi-C3 into CXCR4 positive cells could be verified by fluorescence microscopy (Figure 14). Furthermore, concentrations of $(JM173)_3$-Avi-C3 in the low nanomolar range were sufficient for

intracellular mono-ADP ribosylation of Rho in the murine stage IV breast cancer model cell line 4T1, (Figure 15a). This work indicates that the close spatial proximity of $(JM173)_3$-Avi-C3 to the membrane upon JM173 binding accelerates its uptake into the cancer cells compared to Avi-C3 or wildtype C3 toxin. These results are consistent with the inhibited cell proliferation of human MDA-MB231 breast adenocarcinoma cells upon $(JM173)_3$-Avi-C3 treatment (Figure 15b), clearly confirming an JM173-dependent C3 uptake into these cells. Nevertheless, with increasing concentrations, also a weak JM173-independent uptake of the Avi-C3 subunit could be measured. Avidin has an isoelectric point of around 10, leading to a positive net charge under physiological conditions at pH 7.4 [273]. This positive charge favors nonspecific electrostatic interactions with negatively charged membrane components like phospholipid head groups or glycosaminoglycans. In addition, avidin is glycosylated allowing interactions with carbohydrate-binding structures such as lectins or polysaccharides on the cell surface. These unspecific interactions could be diminished by replacing avidin with other high affinity biotin-binding platforms. Streptavidin isolated from *Streptomyces avidinii* or the chemically modified avidin analog neutravidin have a near-neutral isoelectric point of around 6 and lack glycosylation, minimizing charge-related and carbohydrate-related binding to cell membranes [274,275]. While streptavidin reduces nonspecific binding in terms of charge, it contains the tripeptide sequence Arginine-Tyrosine-Asparagine mimicking the RGD motif of integrin receptor ligands potentially causing adhesion to integrin receptor-expressing cells. Neutravidin avoids this particular off-target interaction since it lacks this amino acid motif [92]. Using these analogs could further reduce immunogenic reactions when applied intravenously compared to avidin, since humans showed basal anti-avidin antibody titers in their blood that are rising upon avidin treatment. Nevertheless, no antibody-related clinical symptoms could be observed in humans or animals upon avidin treatment [181,183]. This could be confirmed in this work by toxicity studies in 4T1 cells, MDA-MB231 cells and zebrafish embryos that were treated with the transporter and retargeting subunit $(JM173)_3$-Avi (Figure 11). Thereby, a negligible toxicity in concentration above 5 µM could be shown in the zebrafish model, that does not influence further development of the fish. Summarized, $(JM173)_3$-Avi-C3 is an efficient and CXCR4-specific transporter for the cytosolic delivery of C3 toxin into breast cancer cells, leading to inhibition of cell proliferation.

4.1.3 $(JM173)_3$-Avi-C3 Influences Osteoclastogenesis, Osteoclast Resorption Activity and Osteoblastogenesis

Since this study aimed to treat breast cancer metastases in the bone niche, co-morbidities like the imbalance in bone homeostasis due to overacting osteoclasts should be addressed as well. The tumor-induced vicious cycle between cancer cells and osteoclasts not only leads to enhanced tumor growth but also to a loss of bone mass. This results in bone pain, hypercalcemia, spinal cord compression or pathological fractures [169]. Several studies showed that C3 toxin was able to enter monocyte-derived osteoclasts inhibiting their bone resorption activity by disturbing the actin cytoskeleton [64,276]. This thesis revealed that also the nanocarrier $(JM173)_3$-Avi-C3 was able to inhibit osteoclastogenesis of differentiating RAW 264.7 cells in a low nanomolar range (Figure 16a/c). Additionally, the resorption activity of osteoclasts was lowered (Figure 16b/d), resulting in an overall reduction of bone degrading mechanisms by $(JM173)_3$-Avi-C3. When using therapeutic agents to inhibit bone resorption, it must be considered that also adverse effects have been reported. For example, bisphosphonate treatment can induce stress fractures due to over-suppression of bone remodeling, whereas denosumab can lower the bone turnover and induce hypocalcemia [277]. The treatment with $(JM173)_3$-Avi-C3 in the context of bone metastases could be advantageous over the named standard treatments. C3 toxin induces only a transient inhibition of Rho, since the de-novo synthesis of non-modified Rho gradually replaces the inactivated GTPases. This leads to recovery of Rho signaling over time, avoiding long-time effects of osteoclast inhibition. Therefore, $(JM173)_3$-Avi-C3 could support the restoration of bone homeostasis during the presence of bone metastases without leading to further co-morbidities related to bone remodeling.

Surprisingly and in contrast to results from earlier studies, C3 toxin also modulated osteoblastogenesis [276]. Upon $(JM173)_3$-Avi-C3 or Avi-C3 treatment of osteoblastic MC3T3 cells, the differentiation markers RUNX2 and AP as well as the proliferation marker KI67 were upregulated (Figure 17). Since RUNX2 is an early transcription factor that sensitizes the cell for following differentiation events, even the observed small ~2-fold changes in its expression profile can lead to a potentiation of downstream effects. RUNX2 is typically upregulated in pre-osteoblasts and immature osteoblasts and controls downstream gene expression linked to osteogenesis, including AP [278,279]. The early-to-intermediate differentiation marker AP is ~10-fold upregulated, while BGLAP is unaffected

in the presence of C3-containing constructs, indicating osteoblast differentiation and matrix maturation in an early stage [280]. In particular, the increased expression of KI67 (~5-fold) indicates sustained proliferative activity, which is characteristic of early stages of osteogenic differentiation, in which proliferation and differentiation can occur simultaneously [281,282]. In conclusion, the nanocarrier $(JM173)_3$-Avi-C3 was not only able to inhibit bone degradation by downregulation of osteoclastogenesis and osteoclast resorption activity but was also activating osteoblastogenesis in osteoblastic progenitor cells. Together with its anti-tumor properties, the tri-directional activities of $(JM173)_3$-Avi-C3 could be beneficial for restoring bone homeostasis at metastatic sites.

Nevertheless, when applying the nanocarrier $(JM173)_3$-Avi-C3 it must be considered that the CXCR4 receptor is not only expressed in the targeted breast cancer cells but also to an elevated level in the bone marrow. Systemic application of $(JM173)_3$-Avi-C3 via the blood might lead to distribution into the bone marrow due to the high CXCR4 expression and the permissive microvasculature. To circumvent this, the use of hydro- or nanogels for local application can be considered. Modern imaging systems like magnetic resonance imaging or positron emission tomography can be used to detect bone metastases in bone and bone marrow for precise application. A study successfully investigated the application of C3 toxin using a protein-DNA hybrid hydrogel with the aim of improving the treatment strategies for bone-degrading diseases like osteoporosis. There, the controlled toxin delivery over time on a local area led to selective modulation of osteoclast functions to reduce bone resorption [276]. By using hydrogel injections directly at the affected remodeling zone, the release of $(JM173)_3$-Avi-C3 could be controlled spatiotemporally without affecting bone marrow cells that are additionally protected by further bone structures [283,284].

4.1.4 Conclusion and Outlook

This study demonstrated that the nanocarrier $(JM173)_3$-Avi-C3 can be used as a biologic to target breast carcinoma metastases in bone by its dual function. $(JM173)_3$-Avi-C3 inhibits proliferation of CXCR4-expressing cancer cells by retargeting the C3 toxin into their cytosol, leading to Rho modification and actin dysregulation. In addition, $(JM173)_3$-Avi-C3 has the potential to diminish pathogenic bone degradation processes by reduction of osteoclastogenesis and osteoclast resorption activity. Furthermore, the disrupted bone homeostasis in the bone niche of cancer metastases could benefit from the positive effects

of $(JM173)_3$-Avi-C3 on osteoblastogenesis. In the next step, the role of $(JM173)_3$-Avi-C3 in the interplay between cancer cells and osteoclasts could be examined in more detail. There are several systems available to study the vicious cycle *in vitro*, for example co-culture models, organoids, or xenografts [285,286]. The more complex the model, the more accurate the microenvironment of the metastatic tumor can be mimicked. Hence, the state-of-the-art models are microfluid devices, also known as "organ-on-a-chip", where vascularization and spatial organization of the tissue can be induced. This allows the full recreation of bone marrow niches to study the migration and infiltration of breast cancer cells [287,288]. Before *in vivo* studies can be considered, further parameters like pharmacokinetics need to be assessed. Since there has been evidence that biotin-protein bonds are susceptible to hydrolysis in human plasma, $(JM173)_3$-Avi-C3 was tested for its stability by fluorescence correlation spectroscopy [187,289]. Even though a small portion of $(JM173)_3$-Avi-C3 interacted with plasma proteins, the constant hydrodynamic radii of the nanocarriers showed stably connection of biotin with both JM173 and C3 toxin [187]. To further improve the plasma stability as well as the therapeutic potency of the nanocarrier, the targeting unit JM173 could be optimized. Due to the simple assembly concept of $(JM173)_3$-Avi-C3, the targeting unit can be interchanged by other CXCR4 targeting EPI-X4 peptides that were modified by incorporating non-natural amino acids or by coupling to long-chain fatty acids. For example, JM198 shows increased affinity and antagonistic activity towards CXCR4 upon lipidation [188,290]. Taken together, $(JM173)_3$-Avi-C3 represents a highly modular system for retargeting C3 into CXCR4 overexpressing cells, providing an opportunity to treat not only breast cancer metastases, but also co-morbidities linked to the vicious cycle in the bone niche. Although several aspects of the C3 toxin function like the cell surface receptor or the exact uptake route to the cytosol are not completely understood so far, the present study highlights the potential of C3 toxin to down-modulate cancer cell growth.

4.2 $C3_{E174Q}$ as Cell Type-Selective Transport System for Targeted Gene Modulation

Efficient cytosolic delivery of proteins or peptides remains challenging, largely due to the poor membrane permeability of these biomolecules [257]. This also accounts for the delivery of CRISPR/Cas9 components for targeted gene modulation. Current strategies

largely rely on physical methods, such as electroporation or microinjection, viral delivery systems or nanoparticles for transporting Cas9 and sgRNA into cells. While these approaches can achieve high editing efficiency, they are often associated with significant limitations.

Physical methods for transfection include among other microinjections, electroporation or sonoporation and are mainly limited by the lack of cell type specificity and scalability. For example, microinjections are hardly transferrable to mammals on a larger scale since the necessary oocytes for germline editing need to be extracted, fertilized and the embryo needs to be implanted, thereby limiting the use of microinjections for clinical approaches [291]. The *in vivo* usage of electroporation is massively limited due to its restriction to the electroporated area and potential local tissue damage upon the applied electric fields [225,292]. This drawback also accounts for sonoporation, where cells are treated with low-level ultrasound waves for permeabilization of the plasma membrane [293]. To avoid cellular damage caused by physical methods, viral vectors have been established as effective tools to deliver CRISR/Cas components during infiltration of cells [229–233]. Despite the high efficiency of CRISPR/Cas gene editing via viral vectors, safety concerns arise. Challenges like the immune response against viral capsid proteins or the risk of off-target genome integration and mutagenesis with genotoxic effects limit their clinical potential. In addition, the packaging size of viral particles is limited to around 5000 base pairs e.g. in AAVs, restricting the number of transported sgRNAs or regulatory elements [294]. Also, non-viral delivery platforms like lipid-based nanoparticles were widely used for gene editing, however, they show limitations regarding Cas9 stability since the harsh packing conditions often lead to precipitation of Cas9.

A novel and promising approach for Cas9 transport into cells is the application of transporter molecules based on non-toxic portions of bacterial AB-type toxins. Since bacteria have developed highly effective strategies for the uptake of their exotoxins into the cytosol of eukaryotic cells, they could be highjacked for effective drug delivery. Several studies already showed the potential of bacterial binding- and translocation (B) components of AB-type toxins as transport systems. Examples are the *Clostridium botulinum* C2 toxin C2IIa and the *Bacillus anthracis* protective antigen (PA). They have been shown to transport proteins that are chemically or genetically fused to the N-terminus of their natural ligand, as well as proteins with positively charged N-termini into the cytosol

of target cells [295–297]. One major drawback of both pore-forming transport units is the narrow pore size of around 0.6 nm (PA) to ~2 nm (C2IIa) [298,299]. In order to pass the pore, the cargo not only needs to unfold, but also to correctly refold in the cytosol. It has been shown that stable proteins like eGFP were not able to be transported via C2IIa and can only poorly pass the PA pore [297,300]. Nevertheless, the transport of Cas9 via PA was successfully tested in the CRISPA approach, where the lipolysis-stimulated lipoprotein receptor was knocked out in HCT-116 cells [301]. One drawback of this system is the lack of cell type-selectivity, since PA cell surface receptors are found on a variety of cells.

This thesis aims to establish a new delivery strategy for CRISPR/Cas components for gene editing based on the *Clostridium botulinum* C3 toxin. In this context the use of the non-toxic C3 variant $C3_{E174Q}$ as monocyte-selective transporter for targeted cytosolic and nucleic delivery of Cas9 and sgRNA was examined.

4.2.1 The Genetic Fusion of Cas9 and $C3_{E174Q}$ Does Not Disturb the Individual Protein Functionalities

In order to create the fusion protein $C3_{E174Q}$_Cas9 and C3_Cas9, the C3-variants and Cas9 were genetically fused via a short repetitive glycine-serine linker and successfully expressed in *E. coli* BL21 as a single protein (Figure 18). To ensure correct folding and therefore functionality of the fusion protein parts, the cytosolic uptake of $C3_{E174Q}$_Cas9 was verified by treatment of J774A.1 cells, THP-1 monocytes or THP-1 M0 macrophages with C3_Cas9 monitoring the C3-induced cellular reactions. Thereby, C3_Cas9 exhibited a slightly stronger ADP-ribosylating effect than C3 wildtype reflected by enhanced C3 morphology in J774A.1 cells and stronger ADP-ribosylation of Rho in THP-1 cells (Figure 20, Figure 21). This discrepancy may be a result of the different types of protein purification. While wildtype C3 is purified via a cleavable GST-tag, C3_Cas9 harbors an His-tag that is known to be prone to interact non-specifically with cell surfaces [302,303]. Even though these interactions with negatively charged cell surface structures or metal-ions are considered weak and are not sufficient to induce cellular uptake, the closer proximity of C3 toxin to the cell membrane could enhance C3-mediated internalization of C3_Cas9. This hypothesis is strengthened by flow cytometry data indicating a weak binding of ^{His}Cas9 to the cell surface of THP-1 cells (data not shown).

As a prerequisite for applying $C3_{E174Q}$_Cas9 to biologically relevant endogenous targets, a set of genes was selected to validate the functionality, specificity, and versatility of the Cas9 unit. With the *in vitro* cleavage assay evidence had been provided that $C3_{E174Q}$_Cas9 was able to cut gene fragments of eGFP, LSR and CD33 with the respective designed sgRNA (Figure 19). The use of eGFP as a reporter gene offers an easily quantifiable readout that directly reflects the functional integrity of the encoded protein. This system offers a controlled and standardized platform in which gene perturbations can be monitored without the complexity and variability associated with endogenous loci. An eGFP knockout could therefore serve as a proof-of-principle, demonstrating that $C3_{E174Q}$_Cas9 is capable of inducing double-strand breaks that result in functional gene knockout. To extend the validation of $C3_{E174Q}$_Cas9 beyond artificial reporter systems, the knockout of the *Clostridioides difficile* CDT toxin receptor LSR has been considered. This knockout system was already proved by the institute in the CRISPA approach, where ^{His}Cas9 was successfully transported into HCT-116 cells via PA, leading to a knockout of LSR and to a resistance against CDT intoxication [301]. This thesis showed the effective fragmentation of the LSR gene when treated with an RNP complex of $C3_{E174Q}$_Cas9 and LSR targeting sgRNA on DNA-level (Figure 19). However, although flow cytometric analysis confirmed surface expression of LSR in THP-1 cells that should be used as model cel line for future knockout experiments, these cells did not exhibit CDT sensitivity in preliminary experiments (data not shown). Neither CDT intoxication-induced morphological changes nor ADP-ribosylation of actin were observed, indicating functional resistance to the toxin under the conditions tested. As acquisition of CDT resistance would have provided a straightforward readout for successful LSR knockout, the absence of CDT sensitivity in THP-1 cells limits the utility of this target in a cell-based validation assay. For this reason, another endogenous monocytic target, namely CD33, was considered for a knockout by $C3_{E174Q}$_Cas9. CD33 is a well-established surface marker of monocytic cells and has been implicated in immune regulatory pathways [304]. The sgRNA sequence used for the CD33 knockout was already validated in previously published work, where CD33 was successfully knocked out in THP-1 M0 macrophages to study its association with Alzheimer's disease [305]. The functionality of the RNP complex consisting of the sgRNA sequence targeting CD33 together with $C3_{E174Q}$_Cas9 could also been verified in the *in vitro* cleavage assay in this thesis (Figure 19). The cell surface expression of CD33 allows sensitive detection by antibody binding in flow

cytometry, making it a practical and biologically relevant validation target for $C3_{E174Q}$_Cas9-mediated knockouts.

4.2.2 Optimization of $C3_{E174Q}$_Cas9 Formulation

Treatment of J774A.1 macrophages with the recombinant $C3_{E174Q}$_Cas9 was associated with slight morphological changes, although the protein itself is not expected to exert cytotoxic or activating effects (Figure 20b). Given that $C3_{E174Q}$_Cas9 was purified from *E. coli*, a plausible explanation for this response is contamination with bacterial lipopolysaccharides (LPS), to which macrophages are highly sensitive. Previous studies have shown that J774A.1 macrophages respond to LPS concentrations in the low endotoxin units per milliliter (EU/ml) range of ~0.1–10 EU/ml with cellular activation and morphological changes [306,307]. A measurement of the endotoxin level in C3_Cas9 and $C3_{E174Q}$_Cas9 samples via a quantitative fluorescence enzyme-linked immunosorbent assay (ELISA) revealed LPS concentrations of 1878 EU/ml and 679 EU/ml (Table 19, appendix), respectively, which are substantially above the reported activation thresholds. Before conducting knockout experiments with $C3_{E174Q}$_Cas9 on monocytic cells or *in vivo* LPS should be depleted, e.g. by LPS binding beads that are surface modified with poly-lysine chains, to avoid cellular stimulation or immune reactions. Alternatively, the expression system for $C3_{E174Q}$_Cas9 could be changed to detoxified *E. coli* strains for endotoxin-free purification of the recombinant fusion protein [308].

Throughout the work with $C3_{E174Q}$_Cas9 it has been noticed that the protein tends to form aggregates when added to cell culture. This was observed as impurities in cell culture wells after treatment of J774A.1 cells or THP-1 cells with $C3_{E174Q}$_Cas9 (see black dots in Figure 20b, picture $C3_{E174Q}$_Cas9. Protein aggregation could induce pro-inflammatory signaling in monocytic cells due to enhanced phagocytosis, resulting in potential negative effects on gene editing efficiency [309]. The aggregation behavior of Cas9 proteins had been described before, however, the mechanism behind is not clarified yet. It has been hypothesized that shear-induced processes in pH near the isoelectric point (~pH 9) and the presence of sgRNA increase the instability of Cas9 in solution [310]. A study showed that efficient gene editing requires the presence of over 1300 Cas9 RNP complexes per nucleus, suggesting that aggregation inside or outside the cell could drastically impair functional delivery [311,312]. Several approaches to stabilize Cas9 and RNP complexes have been

developed, ranging from polyglutamic acid coatings to pre-heating sgRNA before RNP complexation [313,314]. To examine and quantify the aggregation behavior of $C3_{E174Q}$_Cas9 techniques such as size exclusion chromatography, dynamic light scattering or fluorescence correlation spectroscopy could be employed. However, improving the solubility by additives like salts, detergents or stabilizers is limited to not trigger monocytic stress responses resulting in unintended activation or differentiation of the target cells when treated with $C3_{E174Q}$_Cas9. Additives like HEPES, moderate salt, polyethylene glycol or arginine and glutamate can help to create near-physiological buffers while reducing aggregation without activating excessive immune stimulation [315]. Therefore, the single buffer components could be titrated while measuring monocytic markers like CD80 and CD86 or cytokines like TNF to check for cell activation [316,317]. An optimized formulation of $C3_{E174Q}$_Cas9 could enhance protein stability and therefore maximize the gene editing efficiency in monocytic cells.

4.2.3 $C3_{E174Q}$_Cas9 Delivers Cas9 into the Nucleus of Monocyte-Derived Cells

To successfully cleave DNA intracellularly, transporting $C3_{E174Q}$_Cas9 into the nucleus is essential. Therefore, the C-terminal NLS sequence should guide the fusion protein for nuclear import. This work showed that $C3_{E174Q}$_Cas9 can reach the nucleus of THP-1 monocytes and THP-1 M0 macrophages in a nanomolar range already four hours after treatment (Figure 22). With increasing concentration of $C3_{E174Q}$_Cas9 (~184 kDa) degradation products of around 160 kDa are detected by the anti-Cas9 antibody, especially in the THP-1 M0 cells. This could refer to Cas9 (158 kDa) and be a hint for degradation of $C3_{E174Q}$_Cas9 upon cellular uptake. The cell entry mechanism of C3 toxin is not fully understood yet but one hypothesis is the uptake via endocytosis resulting in C3-mediated osmotic swelling of lysosomes. The lysosomal membrane disruption leads to leakage and to the release of C3 toxin into the cytosol [69]. The whole process is considered to take around two to four hours, implying a prolonged time span for $C3_{E174Q}$_Cas9 in the acidic endosomal compartment. Lysosomes are rich in broad-spectrum proteases like cathepsins which are activated under acidic conditions. They preferably cleave flexible, non-organized and solvent-accessible structures like the repetitive glycine-serin linker connecting $C3_{E174Q}$ and Cas9 even in the absence of specific recognition motifs [318,319]. To enhance the steric or chemical resistance of $C3_{E174Q}$_Cas9 to proteases in the lysosome, the linker could be adjusted by adding non-natural residues not accessible for protease cleavage [320].

Otherwise, a pH-sensitive cleavable sequence like a hydrazone liker could even improve nuclear transport of Cas9 when it is not sterically hindered by $C3_{E174Q}$ after cytosolic uptake. Once Cas9 can enter the cytosol, the presence of $C3_{E174Q}$ is no longer necessary for the nuclear import or the DNA cleavage activity of Cas9. However, since Cas9 could be detected in the nucleus of $C3_{E174Q}$_Cas9 treated THP-1 cells, the used GSGSG-linker is sufficient for the nucleic delivery of Cas9, and linker re-design is only optional.

4.2.4 Conclusion and Outlook

This thesis demonstrated that the fusion of $C3_{E174Q}$ to Cas9 neither influenced the transport cellular uptake via $C3_{E174Q}$ nor the DNA cleavage capacity of Cas9 *in vitro*. Moreover $C3_{E174Q}$_Cas9 translocated, at least partially, from the cytosol into the nucleus of murine and human monocytic cell lines. Based on this functional characterization, $C3_{E174Q}$_Cas9 was used for proof-of-principle knockout studies of the previously tested target genes encoding for eGFP and CD33. Since it is hypothesized that $C3_{E174Q}$_Cas9 can enter the cytosol without major unfolding or refolding events following the $C3_{E174Q}$ uptake route, sgRNA could possibly be transported together with $C3_{E174Q}$_Cas9 as an RNP complex. Compared to other CRISPR/Cas-delivery methods, where the sgRNA is often encoded on a plasmid delivered by viral particles or electroporation, $C3_{E174Q}$_Cas9 RNP formation would represent a much more convenient approach. In addition, $C3_{E174Q}$_Cas9 RNPs would offer great flexibility of editing genetic targets as the sgRNA is easily interchangeable. To verify successful delivery of RNP complexes to the nucleus, labelled sgRNA could be detected in cells e.g. via fluorescence microscopy. A recent study established the fluorogenic CRISPR (fCRISPR) method, where the sgRNA harbors a sequence that can specifically bind to fluorogenic proteins that are labelled with a Tat peptide-derived Degron domain. These fluorogenic proteins are rapidly degraded by the proteasome machinery but become stabilized and fluorescent upon binding to the sgRNA. This enables the detection of the fluorescence signal in the nucleus without any background signal from unbound fluorophores and helps to visualize RNP uptake [321].

To optimize the $C3_{E174Q}$-dependent gene editing system, modified or smaller Cas-variants could be used in order to maximize cytosolic and nuclear uptake and minimize potential off-target effects. One example to decrease unintended mutagenesis is the double-nicking strategy, where the D10A mutant Cas9 nickase (Cas9n) can bind two sgRNAs targeting close

sequences within one gene. This leads to simultaneously introduced single-stranded nicks on both DNA strands that are repaired by NHEJ. The indel formation level is thereby comparable to the efficiency of wildtype Cas9 with decreased probability of off-target mutagenesis [322]. Alternatively, other Cas-variants like smaller Cas12 isoforms with a molecular weight of around 60-70 kDa could be used to enhance cytosolic uptake and subsequent delivery to the nucleus. However, these isoforms show a slower cleavage kinetic compared to Cas9 lowering the overall cleavage efficiency.

Taken together, the novel fusion protein $C3_{E174Q}$_Cas9, generated in the context of this thesis, represents a promising alternative for CRISPR/Cas-component transport and offers the potential for overcoming limitations of existing delivery methods while enabling precise, controllable genome editing in defined cell populations *ex vivo* or even *in vivo*.

5 Summary

Bacterial toxins are the primary virulence factors of many pathogenic bacteria and play a central role in developing fatal symptoms and morbidities upon infection. Therefore, bacteria evolved highly effective strategies for delivery of their toxins into host cells, including cell type-selective receptor recognition, efficient cytosolic uptake routes and robust intracellular activity. However, these same properties that underline the pathogenic potential of bacterial toxins also render them as attractive molecular tools and potential therapeutics. Prominent examples are the *Clostridium (C.) botulinum* neurotoxin for treatment of spasms or immune-related diseases as well as CRM197, a non-toxic variant of the *Corynebacterium diphtheriae* diphtheria toxin used as vaccine carrier. This thesis showed that the unique properties of *C. botulinum* C3 toxin offer use in multiple research areas. Hence, C3 has been used as pharmacological active cargo in the context of breast carcinoma induced osteolysis and as a monocyte-selective transport system for targeted gene editing. Within this thesis, C3 toxin was successfully retargeted into CXCR4 overexpressing breast cancer cells using the modular nanocarrier $(JM173)_3$-Avi-C3 based on an avidin platform and the CXCR4-targeting peptide JM173. Toxicity studies demonstrated that the retargeting platform $(JM173)_3$-Avi alone does not negatively affect the development of zebrafish embryos when using sub-micromolar concentrations. Further characterization showed that the nanocarrier exclusively binds and is taken up by CXCR4 overexpressing cell lines. Thereby, $(JM173)_3$-Avi-C3 induced intracellular mono-ADP-ribosylation of Rho in breast cancer cells, leading to a reduction in cancer cell proliferation *in vitro*. Additionally, $(JM173)_3$-Avi-C3 inhibited osteoclastogenesis as well as osteoclast activity while likely promoting osteoblast differentiation, making it a promising candidate to treat bone-related co-morbidities linked to breast cancer metastases in late disease stages. In the second part of this thesis the non-toxic C3 mutant $C3_{E174Q}$ was established as a monocyte-selective transporter for Cas9-mediated gene editing. Therefore, the fusion protein $C3_{E174Q}$_Cas9 was successfully designed, cloned and expressed. Characterization of $C3_{E174Q}$_Cas9 revealed that specific RNP complexes were formed when gene targeting sgRNA was added and Cas9 efficiently cleaved the corresponding DNA fragments *in vitro*. The cytosolic uptake of the fusion protein was monitored by using enzymatically active C3_Cas9, which led to C3-mediated morphological changes in murine macrophages and

showed ADP-ribosylation of Rho proteins in macrophages and monocytes indicating successful cytosolic delivery. Further, $C3_{E174Q}$_Cas9 was able to reach the cytosol of THP-1 monocytes and macrophages in a nanomolar range, making it a promising candidate to create cell type-selective knockouts of genes linked to monocyte-related diseases. Taken together, these findings confirm the potential of C3 toxin as a versatile therapeutic protein and cellular transport system and form the basis for future applications in both research fields.

6 List of References

1. Barth H, Stiles BG. Protein Toxins from Bacteria. In: Comprehensive Natural Products II [Internet]. Elsevier; 2010 [cited 2025 Sep 30]. p. 149–73. Available from: https://linkinghub.elsevier.com/retrieve/pii/B9780080453828001131

2. Chaudhuri K, Chatterjee SN, editors. Bacterial Toxins: A Brief Overview. In: Cholera Toxins [Internet]. Berlin, Heidelberg: Springer Berlin Heidelberg; 2009 [cited 2025 Sep 30]. p. 5–11. Available from: http://link.springer.com/10.1007/978-3-540-88452-1_2

3. Barth H, Aktories K, Popoff MR, Stiles BG. Binary Bacterial Toxins: Biochemistry, Biology, and Applications of Common *Clostridium* and *Bacillus* Proteins. Microbiol Mol Biol Rev. 2004 Sep;68(3):373–402.

4. Schleberger C, Hochmann H, Barth H, Aktories K, Schulz GE. Structure and Action of the Binary C2 Toxin from Clostridium botulinum. Journal of Molecular Biology. 2006 Dec;364(4):705–15.

5. Collier RJ. Diphtheria toxin: mode of action and structure. Bacteriological reviews. 1975;39(1):54–85.

6. Idris AOA. Bacterial Toxins: Classification, Cellular Biology, Genetics and Applications. In: Moneim Elhadi Sulieman A, Alshammari NI, editors. Microbial Toxins in Food Systems: Causes, Mechanisms, Complications, and Metabolism [Internet]. Cham: Springer Nature Switzerland; 2024 [cited 2025 Sep 30]. p. 97–108. Available from: https://link.springer.com/10.1007/978-3-031-62839-9_8

7. Goñi FM, Ostolaza H. E. coli a-hemolysin: a membrane-active protein toxin. Braz J Med Biol Res. 1998 Aug;31(8):1019–34.

8. Gill DM. Bacterial toxins: a table of lethal amounts. Microbiol Rev. 1982 Mar;46(1):86–94.

9. Schmitt CK, Meysick KC, O'Brien AD. Bacterial Toxins: Friends or Foes? Emerg Infect Dis. 1999 Apr;5(2):224–34.

10. Rieder CRM, Schestatsky P, Socal MP, Monte TL, Fricke D, Costa J, Picon PD. A Double-blind, Randomized, Crossover Study of Prosigne Versus Botox in Patients With Blepharospasm and Hemifacial Spasm. Clinical Neuropharmacology. 2007 Jan;30(1):39–42.

11. Donaldson DS, Williams NA. Bacterial Toxins as Immunomodulators. In: Fallon PG, editor. Pathogen-Derived Immunomodulatory Molecules [Internet]. New York, NY: Springer New York; 2009 [cited 2025 Sep 30]. p. 1–18. (Back N, Cohen IR, Lajtha A, Lambris JD, Paoletti R, editors. Advances in Experimental Medicine and Biology; vol. 666). Available from: http://link.springer.com/10.1007/978-1-4419-1601-3_1

12. Martarelli D, Pompei P, Mazzoni G. Inhibition of Adrenocortical Carcinoma by Diphtheria Toxin Mutant CRM197. Chemotherapy. 2009;55(6):425–32.

13. Gaillard PJ, De Boer AG. A novel opportunity for targeted drug delivery to the brain. Journal of Controlled Release. 2006 Nov;116(2):e60–2.

14. Malito E, Bursulaya B, Chen C, Surdo PL, Picchianti M, Balducci E, Biancucci M, Brock A, Berti F, Bottomley MJ, Nissum M, Costantino P, Rappuoli R, Spraggon G. Structural basis for lack of toxicity of the diphtheria toxin mutant CRM197. Proc Natl Acad Sci USA. 2012 Apr 3;109(14):5229–34.

15. Shinefield HR. Overview of the development and current use of CRM197 conjugate vaccines for pediatric use. Vaccine. 2010 Jun;28(27):4335–9.

16. Aktories K, Frevert J. ADP-ribosylation of a 21-24 kDa eukaryotic protein(s) by C3, a novel botulinum ADP-ribosyltransferase, is regulated by guanine nucleotide. Biochemical Journal. 1987 Oct 15;247(2):363–8.

17. Just I, Schallehn G, Aktories K. A novel C3-like ADP-ribosyltransferase produced by Clostridium limosum. In: Poirier GG, Moreau P, editors. ADP-Ribosylation Reactions [Internet]. New York, NY: Springer New York; 1992 [cited 2025 Oct 1]. p. 373–6. Available from: http://link.springer.com/10.1007/978-1-4419-8718-1_66

18. Just I, Schallehn G, Aktories K. ADP-ribosylation of small GTP-binding proteins by Bacillus cereus. Biochemical and Biophysical Research Communications. 1992 Mar;183(3):931–6.

19. Wilde C, Chhatwal GS, Schmalzing G, Aktories K, Just I. A Novel C3-like ADP-ribosyltransferase from Staphylococcus aureus Modifying RhoE and Rnd3. Journal of Biological Chemistry. 2001 Mar;276(12):9537–42.

20. Vogelsgesang M, Pautsch A, Aktories K. C3 exoenzymes, novel insights into structure and action of Rho-ADP-ribosylating toxins. Naunyn-Schmied Arch Pharmacol. 2007 Feb 6;374(5–6):347–60.

21. Nemoto Y, Namba T, Kozaki S, Narumiya S. Clostridium botulinum C3 ADP-ribosyltransferase gene. Cloning, sequencing, and expression of a functional protein in Escherichia coli. Journal of Biological Chemistry. 1991 Oct;266(29):19312–9.

22. Popoff M, Boquet P, Gill DM, Eklund MW. DNA sequence of exoenzyme C3, an ADP-ribosyltransferase encoded by *Clostridium botulinum* C and D phages. Nucl Acids Res. 1990;18(5):1291–1291.

23. Just I, Selzer J, Jung M, Van Damm J, Vandekerckhove J, Aktories K. Rho-ADP-ribosylating exoenzyme from Bacillus cereus. Purification, characterization, and identification of the NAD-binding site. Biochemistry. 1995 Jan 10;34(1):334–40.

24. Inoue S, Sugai M, Murooka Y, Paik SY, Hong YM, Ohgai H, Suginaka H. Molecular cloning and sequencing of the epidermal cell differentiation inhibitor gene from Staphylococcus aureus. Biochemical and Biophysical Research Communications. 1991 Jan;174(2):459–64.

25. Yamaguchi T, Hayashi T, Takami H, Ohnishi M, Murata T, Nakayama K, Asakawa K, Ohara M, Komatsuzawa H, Sugai M. Complete Nucleotide Sequence of a *Staphylococcus aureus* Exfoliative Toxin B Plasmid and Identification of a Novel ADP-Ribosyltransferase, EDIN-C. Barbieri JT, editor. Infect Immun. 2001 Dec;69(12):7760–71.

26. Aktories K, Wilde C, Vogelsgesang M. Rho-modifying C3-like ADP-ribosyltransferases. In: Reviews of Physiology, Biochemistry and Pharmacology [Internet]. Berlin, Heidelberg: Springer Berlin Heidelberg; 2005 [cited 2025 Oct 1]. p. 1–22. (Reviews of Physiology, Biochemistry and Pharmacology; vol. 152). Available from: http://link.springer.com/10.1007/s10254-004-0034-4

27. Maehama T, Sekine N, Nishina H, Takahashi K, Katada T. Characterization of botulinum C3-catalyzed ADP-ribosylation ofrho proteins and identification of mammalian C3-like ADP-ribosyltransferase. Mol Cell Biochem. 1994;138(1–2):135–40.

28. Sekine A, Fujiwara M, Narumiya S. Asparagine residue in the rho Gene Product Is the Modification Site for Botulinum ADP-ribosyltransferase. Journal of Biological Chemistry. 1989 May;264(15):8602–5.

29. Aktories K. Rho proteins: targets for bacterial toxins. Trends in microbiology. 1997;5(7):282–8.

30. Han S, Arvai AS, Clancy SB, Tainer JA. Crystal structure and novel recognition motif of Rho ADP-ribosylating C3 exoenzyme from Clostridium botulinum: structural insights for recognition specificity and catalysis. Journal of Molecular Biology. 2001 Jan;305(1):95–107.

31. Ménétrey J, Flatau G, Boquet P, Ménez A, Stura EA. Structural basis for the NAD-hydrolysis mechanism and the ARTT-loop plasticity of C3 exoenzymes. Protein Science. 2008 May;17(5):878–86.

32. Ménétrey J, Flatau G, Stura EA, Charbonnier JB, Gas F, Teulon JM, Le Du MH, Boquet P, Ménez A. NAD Binding Induces Conformational Changes in Rho ADP-ribosylating Clostridium botulinum C3 Exoenzyme. Journal of Biological Chemistry. 2002 Aug;277(34):30950–7.

33. Hall A. Rho GTPases and the Actin Cytoskeleton. Science. 1998 Jan 23;279(5350):509–14.

34. Prokopenko SN, Saint R, Bellen HJ. Untying the Gordian Knot of Cytokinesis. The Journal of Cell Biology. 2000 Mar 6;148(5):843–8.

35. Caron E, Hall A. Identification of Two Distinct Mechanisms of Phagocytosis Controlled by Different Rho GTPases. Science. 1998 Nov 27;282(5394):1717–21.

36. Nobes CD, Hall A. Rho GTPases Control Polarity, Protrusion, and Adhesion during Cell Movement. The Journal of Cell Biology. 1999 Mar 22;144(6):1235–44.

37. Perona R, Montaner S, Saniger L, Sánchez-Pérez I, Bravo R, Lacal JC. Activation of the nuclear factor-kappaB by Rho, CDC42, and Rac-1 proteins. Genes Dev. 1997 Feb 15;11(4):463–75.

38. Olson MF, Ashworth A, Hall A. An Essential Role for Rho, Rac, and Cdc42 GTPases in Cell Cycle Progression Through G_1. Science. 1995 Sep;269(5228):1270–2.

39. Johnson DI. Cdc42: An Essential Rho-Type GTPase Controlling Eukaryotic Cell Polarity. Microbiol Mol Biol Rev. 1999 Mar;63(1):54–105.

40. Boguski MS, McCormick F. Proteins regulating Ras and its relatives. Nature. 1993 Dec 16;366(6456):643–54.

41. Kjøller L, Hall A. Signaling to Rho GTPases. Experimental Cell Research. 1999 Nov;253(1):166–79.

42. Lamarche N, Hall A. GAPs for rho-related GTPases. Trends in Genetics. 1994 Dec;10(12):436–40.

43. Rittinger K, Walker PA, Eccleston JF, Nurmahomed K, Owen D, Laue E, Gamblin SJ, Smerdon SJ. Crystal structure of a small G protein in complex with the GTPase-activating protein rhoGAP. Nature. 1997 Aug 14;388(6643):693–7.

44. Rittinger K, Walker PA, Eccleston JF, Smerdon SJ, Gamblin SJ. Structure at 1.65 Å of RhoA and its GTPase-activating protein in complex with a transition-state analogue. Nature. 1997 Oct;389(6652):758–62.

45. Olofsson B. Rho Guanine Dissociation Inhibitors. Cellular Signalling. 1999 Aug;11(8):545–54.

46. Michaely PA, Mineo C, Ying Y shu, Anderson RGW. Polarized Distribution of Endogenous Rac1 and RhoA at the Cell Surface. Journal of Biological Chemistry. 1999 Jul;274(30):21430–6.

47. Fujihara H, Walker LA, Gong MC, Lemichez E, Boquet P, Somlyo AV, Somlyo AP. Inhibition of RhoA Translocation and Calcium Sensitization by In Vivo ADP-Ribosylation with the Chimeric Toxin DC3B. MBoC. 1997 Dec;8(12):2437–47.

48. Genth H, Gerhard R, Maeda A, Amano M, Kaibuchi K, Aktories K, Just I. Entrapment of Rho ADP-ribosylated by Clostridium botulinum C3 Exoenzyme in the Rho-Guanine Nucleotide Dissociation Inhibitor-1 Complex. Journal of Biological Chemistry. 2003 Aug;278(31):28523–7.

49. Stamatovic SM, Keep RF, Kunkel SL, Andjelkovic AV. Potential role of MCP-1 in endothelial cell tight junction `opening': signaling via Rho and Rho kinase. Journal of Cell Science. 2003 Nov 15;116(22):4615–28.

50. Chen LY, Zuraw BL, Liu FT, Huang S, Pan ZK. IL-1 Receptor-Associated Kinase and Low Molecular Weight GTPase RhoA Signal Molecules Are Required for Bacterial Lipopolysaccharide-Induced Cytokine Gene Transcription. The Journal of Immunology. 2002 Oct 1;169(7):3934–9.

51. Laudanna C, Campbell JJ, Butcher EC. Role of Rho in Chemoattractant-Activated Leukocyte Adhesion Through Integrins. Science. 1996 Feb 16;271(5251):981–3.

52. Millán J, Ridley AJ. Rho GTPases and leucocyte-induced endothelial remodelling. Biochemical Journal. 2005 Jan 15;385(2):329–37.

53. Ebeling J, Fünfhaus A, Genersch E. The Buzz about ADP-Ribosylation Toxins from Paenibacillus larvae, the Causative Agent of American Foulbrood in Honey Bees. Toxins. 2021 Feb 16;13(2):151.

54. Fünfhaus A, Poppinga L, Genersch E. Identification and characterization of two novel toxins expressed by the lethal honey bee pathogen *P aenibacillus larvae,* the causative agent of A merican foulbrood. Environmental Microbiology. 2013 Nov;15(11):2951–65.

55. Rohrbeck A, Schröder A, Hagemann S, Pich A, Höltje M, Ahnert-Hilger G, Just I. Vimentin Mediates Uptake of C3 Exoenzyme. Gillet D, editor. PLoS ONE. 2014 Jun 26;9(6):e101071.

56. Rohrbeck A, Höltje M, Adolf A, Oms E, Hagemann S, Ahnert-Hilger G, Just I. The Rho ADP-ribosylating C3 exoenzyme binds cells via an Arg–Gly–Asp motif. Journal of Biological Chemistry. 2017 Oct;292(43):17668–80.

57. Adolf A, Leondaritis G, Rohrbeck A, Eickholt BJ, Just I, Ahnert-Hilger G, Höltje M. The intermediate filament protein vimentin is essential for axonotrophic effects of *Clostridium botulinum* C3 exoenzyme. Journal of Neurochemistry. 2016 Oct;139(2):234–44.

58. Ludwig BS, Kessler H, Kossatz S, Reuning U. RGD-Binding Integrins Revisited: How Recently Discovered Functions and Novel Synthetic Ligands (Re-)Shape an Ever-Evolving Field. Cancers. 2021 Apr 4;13(7):1711.

59. Sehr P, Joseph G, Genth H, Just I, Pick E, Aktories K. Glucosylation and ADP Ribosylation of Rho Proteins: Effects on Nucleotide Binding, GTPase Activity, and Effector Coupling. Biochemistry. 1998 Apr 1;37(15):5296–304.

60. Boquet P, Munro P, Fiorentini C, Just I. Toxins from anaerobic bacteria: specificity and molecular mechanisms of action. Current Opinion in Microbiology. 1998 Feb;1(1):66–74.

61. Barth H, Fischer S, Möglich A, Förtsch C. Clostridial C3 Toxins Target Monocytes/Macrophages and Modulate Their Functions. Front Immunol [Internet]. 2015 Jun 30 [cited 2025 Oct 8];6. Available from: http://journal.frontiersin.org/Article/10.3389/fimmu.2015.00339/abstract

62. Dmochewitz L, Förtsch C, Zwerger C, Vaeth M, Felder E, Huber-Lang M, Barth H. A Recombinant Fusion Toxin Based on Enzymatic Inactive C3bot1 Selectively Targets Macrophages. Popoff MR, editor. PLoS ONE. 2013 Jan 21;8(1):e54517.

63. Fellermann M, Huchler C, Fechter L, Kolb T, Wondany F, Mayer D, Michaelis J, Stenger S, Mellert K, Möller P, Barth TFE, Fischer S, Barth H. Clostridial C3 Toxins Enter and Intoxicate Human Dendritic Cells. Toxins. 2020 Sep 1;12(9):563.

64. Tautzenberger A, Förtsch C, Zwerger C, Dmochewitz L, Kreja L, Ignatius A, Barth H. C3 Rho-Inhibitor for Targeted Pharmacological Manipulation of Osteoclast-Like Cells. Popoff MR, editor. PLoS ONE. 2013 Dec 27;8(12):e85695.

65. Rohrbeck A, Von Elsner L, Hagemann S, Just I. Uptake of Clostridium botulinum C3 Exoenzyme into Intact HT22 and J774A.1 Cells. Toxins. 2015 Feb 2;7(2):380–95.

66. Fahrer J, Kuban J, Heine K, Rupps G, Kaiser E, Felder E, Benz R, Barth H. Selective and specific internalization of clostridial C3 ADP-ribosyltransferases into macrophages and monocytes. Cellular Microbiology. 2010 Feb;12(2):233–47.

67. Krska D, Ravulapalli R, Fieldhouse RJ, Lugo MR, Merrill AR. C3larvin Toxin, an ADP-ribosyltransferase from Paenibacillus larvae. Journal of Biological Chemistry. 2015 Jan;290(3):1639–53.

68. Fellermann M, Stemmer M, Noschka R, Wondany F, Fischer S, Michaelis J, Stenger S, Barth H. Clostridium botulinum C3 Toxin for Selective Delivery of Cargo into Dendritic Cells and Macrophages. Toxins. 2022 Oct 18;14(10):711.

69. Turner M, Plumb J, Merrill AR, Grinstein S, Westman J. Lysosomal swelling and lysis mediate delivery of C3 toxins to their cytoplasmic targets. Molecular Microbiology. 2023 Jun;119(6):695–710.

70. Aktories K. Bacterial Protein Toxins as Tools in Cell Biology and Pharmacology. In: Cossart P, Boquet P, Normark S, Rappuoli R, editors. Cellular Microbiology [Internet]. Washington, DC, USA: ASM Press; 2014 [cited 2025 Oct 9]. p. 341–60. Available from: http://doi.wiley.com/10.1128/9781555817633.ch14

71. Chardin P, Boquet P, Madaule P, Popoff MR, Rubin EJ, Gill DM. The mammalian G protein rhoC is ADP-ribosylated by Clostridium botulinum exoenzyme C3 and affects actin microfilaments in Vero cells. The EMBO Journal. 1989 Apr;8(4):1087–92.

72. Rubin EJ, Gill DM, Boquet P, Popoff MR. Functional Modification of a 21-Kilodalton G Protein when ADP-Ribosylated by Exoenzyme C3 of *Clostridium botulinum*. Molecular and Cellular Biology. 1988 Jan 1;8(1):418–26.

73. Ridley AJ, Hall A. The small GTP-binding protein rho regulates the assembly of focal adhesions and actin stress fibers in response to growth factors. Cell. 1992 Aug;70(3):389–99.

74. Watanabe N. p140mDia, a mammalian homolog of Drosophila diaphanous, is a target protein for Rho small GTPase and is a ligand for profilin. The EMBO Journal. 1997 Jun 1;16(11):3044–56.

75. Aullo P, Giry M, Olsnes S, Popoff MR, Kocks C, Boquet P. A chimeric toxin to study the role of the 21 kDa GTP binding protein rho in the control of actin microfilament assembly. The EMBO Journal. 1993 Mar;12(3):921–31.

76. Mitamura T, Higashiyama S, Taniguchi N, Klagsbrun M, Mekada E. Diphtheria Toxin Binds to the Epidermal Growth Factor (EGF)-like Domain of Human Heparin-binding EGF-like Growth Factor/Diphtheria Toxin Receptor and Inhibits Specifically Its Mitogenic Activity. Journal of Biological Chemistry. 1995 Jan;270(3):1015–9.

77. Eckhardt M, Barth H, Blöcker D, Aktories K. Binding of Clostridium botulinum C2 Toxin to Asparagine-linked Complex and Hybrid Carbohydrates. Journal of Biological Chemistry. 2000 Jan;275(4):2328–34.

78. Barth H, Hofmann F, Olenik C, Just I, Aktories K. The N-Terminal Part of the Enzyme Component (C2I) of the Binary *Clostridium botulinum* C2 Toxin Interacts with the Binding Component C2II and Functions as a Carrier System for a Rho ADP-Ribosylating C3-Like Fusion Toxin. Infect Immun. 1998 Apr;66(4):1364–9.

79. Sahai E, Olson MF. Purification of TAT-C3 Exoenzyme. In: Methods in Enzymology [Internet]. Elsevier; 2006 [cited 2025 Oct 21]. p. 128–40. Available from: https://linkinghub.elsevier.com/retrieve/pii/S0076687906060113

80. Wadia JS, Stan RV, Dowdy SF. Transducible TAT-HA fusogenic peptide enhances escape of TAT-fusion proteins after lipid raft macropinocytosis. Nat Med. 2004 Mar;10(3):310–5.

81. Xu L, Silva MJSA, Coelho JAS, Borho J, Stadler N, Barth H, Kuan SL, Weil T. Chemoselective dual functionalization of proteins via 1,6-addition of thiols to trifunctional N-alkylpyridinium. Nat Commun. 2025 Jun 6;16(1):5278.

82. Pirooznia N, Abdi K, Beiki D, Emami F, Arab SS, Sabzevari O, Pakdin-Parizi Z, Geramifar P. Radiosynthesis, Biological Evaluation, and Preclinical Study of a^{68} Ga-Labeled Cyclic RGD Peptide as an Early Diagnostic Agent for Overexpressed $\alpha_v \beta_3$ Integrin Receptors in Non-Small-Cell Lung Cancer. Contrast Media & Molecular Imaging. 2020 Mar 31;2020:1–11.

83. Linseman D A. Diverse roles of Rho family GTPases in neuronal development, survival, and death. Front Biosci. 2008;13(13):657.

84. McKerracher L, Higuchi H. Targeting Rho To Stimulate Repair after Spinal Cord Injury. Journal of Neurotrauma. 2006 Apr;23(3–4):309–17.

85. Ahnert-Hilger G, Höltje M, Große G, Pickert G, Mucke C, Nixdorf-Bergweiler B, Boquet P, Hofmann F, Just I. Differential effects of Rho GTPases on axonal and dendritic development in hippocampal neurones. Journal of Neurochemistry. 2004 Jul;90(1):9–18.

86. Helfrich MH. Osteoclast diseases. Microscopy Res & Technique. 2003 Aug 15;61(6):514–32.

87. Böhmer J, Jung M, Sehr P, Fritz G, Popoff M, Just I, Aktories K. Active Site Mutation of the C3-like ADP-Ribosyltransferase from Clostridium limosum Analysis of Glutamic Acid 174. Biochemistry. 1996 Jan 1;35(1):282–9.

88. Saito Y, Nemoto Y, Ishizaki T, Watanabe N, Morii N, Narumiya S. Identification of Glu173 as the critical amino acid residue for the ADP-ribosyltransferase activity of Clostridium botulinum C3 exoenzyme. FEBS Letters. 1995 Sep 4;371(2):105–9.

89. Aktories K. Studies on the active-site structure of C3-like exoenzymes: Involvement of glutamic acid in catalysis of ADP-ribosylation. Biochimie. 1995;77(5):326–32.

90. Christow H, Lillich M, Sold A, Fahrer J, Barth H. Recombinant streptavidin-C3bot for delivery of proteins into macrophages. Toxicon. 2013 Dec;75:144–7.

91. Lillich M, Chen X, Weil T, Barth H, Fahrer J. Streptavidin-Conjugated C3 Protein Mediates the Delivery of Mono-Biotinylated RNAse A into Macrophages. Bioconjugate Chem. 2012 Jul 18;23(7):1426–36.

92. Alon R, Bayer EA, Wilchek M. Streptavidin contains an RYD sequence which mimics the RGD receptor domain of fibronectin. Biochemical and Biophysical Research Communications. 1990 Aug;170(3):1236–41.

93. World Health Organization. Cancer. [cited 2025 Oct 27]; Available from: https://www.who.int/news-room/fact-sheets/detail/cancer

94. World Health Organization. Breast Cancer. [cited 2025 Oct 27]; Available from: https://www.who.int/news-room/fact-sheets/detail/breast-cancer

95. Siegel RL, Kratzer TB, Giaquinto AN, Sung H, Jemal A. Cancer statistics, 2025. CA A Cancer J Clinicians. 2025 Jan;75(1):10–45.

96. Walker S, Hyde C, Hamilton W. Risk of breast cancer in symptomatic women in primary care: a case–control study using electronic records. Br J Gen Pract. 2014 Dec;64(629):e788–93.

97. Burgess C, Ramirez A, Richards M, Love S. Who and what influences delayed presentation in breast cancer? Br J Cancer. 1998 Apr;77(8):1343–8.

98. Sørlie T, Tibshirani R, Parker J, Hastie T, Marron JS, Nobel A, Deng S, Johnsen H, Pesich R, Geisler S, Demeter J, Perou CM, Lønning PE, Brown PO, Børresen-Dale AL, Botstein D. Repeated observation of breast tumor subtypes in independent gene expression data sets. Proc Natl Acad Sci USA. 2003 Jul 8;100(14):8418–23.

99. Analysis at Eight Years by “Nolvadex”, Adjuvant Trial Organisation. Controlled trial of tamoxifen as a single adjuvant agent in the management of early breast cancer: Analysis at Eight Years by ’Nolvadex’/Adjuvant Trial Organisation. Br J Cancer. 1988 Dec;57(6):608–11.

100. Ellis PA, Saccani-Jotti G, Clarke R, Johnston SRD, Anderson E, Howell A, A’hern R, Salter J, Detre S, Nicholson R, Robertson J, Smith IE, Dowsett M. Induction of apoptosis by

tamoxifen and ICI 182780 in primary breast cancer. Int J Cancer. 1997 Aug 7;72(4):608–13.

101. Piccart-Gebhart MJ, Procter M, Leyland-Jones B, Goldhirsch A, Untch M, Smith I, Gianni L, Baselga J, Bell R, Jackisch C, Cameron D, Dowsett M, Barrios CH, Steger G, Huang CS, Andersson M, Inbar M, Lichinitser M, Láng I, Nitz U, Iwata H, Thomssen C, Lohrisch C, Suter TM, Rüschoff J, Sütő T, Greatorex V, Ward C, Straehle C, McFadden E, Dolci MS, Gelber RD. Trastuzumab after Adjuvant Chemotherapy in HER2-Positive Breast Cancer. N Engl J Med. 2005 Oct 20;353(16):1659–72.

102. Swain SM, Kim SB, Cortés J, Ro J, Semiglazov V, Campone M, Ciruelos E, Ferrero JM, Schneeweiss A, Knott A, Clark E, Ross G, Benyunes MC, Baselga J. Pertuzumab, trastuzumab, and docetaxel for HER2-positive metastatic breast cancer (CLEOPATRA study): overall survival results from a randomised, double-blind, placebo-controlled, phase 3 study. The Lancet Oncology. 2013 May;14(6):461–71.

103. Yuan Y, Liu X, Cai Y, Li W. Lapatinib and lapatinib plus trastuzumab therapy versus trastuzumab therapy for HER2 positive breast cancer patients: an updated systematic review and meta-analysis. Syst Rev. 2022 Dec 10;11(1):264.

104. Saloustros E, Mavroudis D, Georgoulias V. Paclitaxel and docetaxel in the treatment of breast cancer. Expert Opinion on Pharmacotherapy. 2008 Oct;9(15):2603–16.

105. Walko CM, Lindley C. Capecitabine: A review. Clinical Therapeutics. 2005 Jan;27(1):23–44.

106. Thiery JP, Acloque H, Huang RYJ, Nieto MA. Epithelial-Mesenchymal Transitions in Development and Disease. Cell. 2009 Nov;139(5):871–90.

107. Condeelis J, Pollard JW. Macrophages: Obligate Partners for Tumor Cell Migration, Invasion, and Metastasis. Cell. 2006 Jan;124(2):263–6.

108. Roussos ET, Condeelis JS, Patsialou A. Chemotaxis in cancer. Nat Rev Cancer. 2011 Aug;11(8):573–87.

109. Keskin D, Kim J, Cooke VG, Wu CC, Sugimoto H, Gu C, De Palma M, Kalluri R, LeBleu VS. Targeting Vascular Pericytes in Hypoxic Tumors Increases Lung Metastasis via Angiopoietin-2. Cell Reports. 2015 Feb;10(7):1066–81.

110. Caswell-Jin JL, Plevritis SK, Tian L, Cadham CJ, Xu C, Stout NK, Sledge GW, Mandelblatt JS, Kurian AW. Change in Survival in Metastatic Breast Cancer with Treatment Advances: Meta-Analysis and Systematic Review. JNCI Cancer Spectrum. 2018 Oct 1;2(4):pky062.

111. Poortmans PMP, Coles C, Bernier J. Treatment of Regional Lymph Nodes in Breast Cancer—Evidence in Favor of Radiation Therapy. JAMA Oncol. 2016 Aug 1;2(8):989.

112. diSibio G, French SW. Metastatic Patterns of Cancers: Results From a Large Autopsy Study. Archives of Pathology & Laboratory Medicine. 2008 Jun 1;132(6):931–9.

113. Minn AJ, Gupta GP, Siegel PM, Bos PD, Shu W, Giri DD, Viale A, Olshen AB, Gerald WL, Massagué J. Genes that mediate breast cancer metastasis to lung. Nature. 2005 Jul 28;436(7050):518–24.

114. Bos PD, Zhang XHF, Nadal C, Shu W, Gomis RR, Nguyen DX, Minn AJ, Van De Vijver MJ, Gerald WL, Foekens JA, Massagué J. Genes that mediate breast cancer metastasis to the brain. Nature. 2009 Jun;459(7249):1005–9.

115. Karsenty G. Transcriptional Control of Skeletogenesis. Annu Rev Genom Hum Genet. 2008 Sep 1;9(1):183–96.

116. Franceschi RT, Xiao G, Jiang D, Gopalakrishnan R, Yang S, Reith E. Multiple signaling pathways converge on the Cbfa1/Runx2 transcription factor to regulate osteoblast differentiation. Connect Tissue Res. 2003;44 Suppl 1(Suppl 1):109–16.

117. Grigoriadis AE, Wang ZQ, Cecchini MG, Hofstetter W, Felix R, Fleisch HA, Wagner EF. c-Fos: a Key Regulator of Osteoclast-Macrophage Lineage Determination and Bone Remodeling. Science. 1994 Oct 21;266(5184):443–8.

118. Lian JB, Stein GS, Stein JL, Van Wijnen AJ. Osteocalcin gene promoter: Unlocking the secrets for regulation of osteoblast growth and differentiation. J Cell Biochem. 1998;72(S30-31):62–72.

119. Teitelbaum SL, Ross FP. Genetic regulation of osteoclast development and function. Nat Rev Genet. 2003 Aug;4(8):638–49.

120. Bonewald LF. Osteocytes as Dynamic Multifunctional Cells. Annals of the New York Academy of Sciences. 2007 Nov;1116(1):281–90.

121. Weitzmann MN, Pacifici R. T Cells: Unexpected Players in the Bone Loss Induced by Estrogen Deficiency and in Basal Bone Homeostasis. Annals of the New York Academy of Sciences. 2007 Nov;1116(1):360–75.

122. Lowry MB, Lotinun S, Leontovich AA, Zhang M, Maran A, Shogren KL, Palama BK, Marley K, Iwaniec UT, Turner RT. Osteitis Fibrosa Is Mediated by Platelet-Derived Growth Factor-A Via a Phosphoinositide 3-Kinase-Dependent Signaling Pathway in a Rat Model for Chronic Hyperparathyroidism. Endocrinology. 2008 Nov 1;149(11):5735–46.

123. Li Y, Toraldo G, Li A, Yang X, Zhang H, Qian WP, Weitzmann MN. B cells and T cells are critical for the preservation of bone homeostasis and attainment of peak bone mass in vivo. Blood. 2007 May 1;109(9):3839–48.

124. Truswell AS. Osteopetrosis with Syndactyly. The Journal of Bone and Joint Surgery British volume. 1958 May;40-B(2):208–18.

125. Balemans W. Increased bone density in sclerosteosis is due to the deficiency of a novel secreted protein (SOST). Human Molecular Genetics. 2001 Mar 1;10(5):537–43.

126. Blangy A, Bompard G, Guerit D, Marie P, Maurin J, Morel A, Vives V. The osteoclast cytoskeleton – current understanding and therapeutic perspectives for osteoporosis. Journal of Cell Science. 2020 Jul 1;133(13):jcs244798.

127. Hauge EM, Qvesel D, Eriksen EF, Mosekilde L, Melsen F. Cancellous Bone Remodeling Occurs in Specialized Compartments Lined by Cells Expressing Osteoblastic Markers. Journal of Bone and Mineral Research. 2001 Sep 1;16(9):1575–82.

128. Andersen TL, Sondergaard TE, Skorzynska KE, Dagnaes-Hansen F, Plesner TL, Hauge EM, Plesner T, Delaisse JM. A Physical Mechanism for Coupling Bone Resorption and Formation in Adult Human Bone. The American Journal of Pathology. 2009 Jan;174(1):239–47.

129. Heino TJ, Hentunen TA, Väänänen HK. Osteocytes inhibit osteoclastic bone resorption through transforming growth factor-β: Enhancement by estrogen*. J of Cellular Biochemistry. 2002 Jan;85(1):185–97.

130. Swarthout JT, D'Alonzo RC, Selvamurugan N, Partridge NC. Parathyroid hormone-dependent signaling pathways regulating genes in bone cells. Gene. 2002 Jan;282(1–2):1–17.

131. Yang CM, Chien CS, Yao CC, Hsiao LD, Huang YC, Wu CB. Mechanical Strain Induces Collagenase-3 (MMP-13) Expression in MC3T3-E1 Osteoblastic Cells. Journal of Biological Chemistry. 2004 May;279(21):22158–65.

132. Ma YL, Cain RL, Halladay DL, Yang X, Zeng Q, Miles RR, Chandrasekhar S, Martin TJ, Onyia JE. Catabolic Effects of Continuous Human PTH (1–38) in Vivo Is Associated with Sustained Stimulation of RANKL and Inhibition of Osteoprotegerin and Gene-Associated Bone Formation. Endocrinology. 2001 Sep 1;142(9):4047–54.

133. Teitelbaum SL. Bone Resorption by Osteoclasts. Science. 2000 Sep;289(5484):1504–8.

134. Abu-Amer Y, Ross FP, Schlesinger P, Tondravi MM, Teitelbaum SL. Substrate Recognition by Osteoclast Precursors Induces C-src/Microtubule Association. The Journal of Cell Biology. 1997 Apr 7;137(1):247–58.

135. Saftig P, Hunziker E, Wehmeyer O, Jones S, Boyde A, Rommerskirch W, Moritz JD, Schu P, Von Figura K. Impaired osteoclastic bone resorption leads to osteopetrosis in cathepsin-K-deficient mice. Proc Natl Acad Sci USA. 1998 Nov 10;95(23):13453–8.

136. Zhao C, Irie N, Takada Y, Shimoda K, Miyamoto T, Nishiwaki T, Suda T, Matsuo K. Bidirectional ephrinB2-EphB4 signaling controls bone homeostasis. Cell Metabolism. 2006 Aug;4(2):111–21.

137. Pederson L, Ruan M, Westendorf JJ, Khosla S, Oursler MJ. Regulation of bone formation by osteoclasts involves Wnt/BMP signaling and the chemokine sphingosine-1-phosphate. Proc Natl Acad Sci USA. 2008 Dec 30;105(52):20764–9.

138. Robey PG, Boskey AL. The composition of bone. Primer on the metabolic bone diseases and disorders of mineral metabolism. 2008;7:32–8.

139. Allen MR, Burr DB. Bone Modeling and Remodeling. In: Basic and Applied Bone Biology [Internet]. Elsevier; 2014 [cited 2025 Oct 29]. p. 75–90. Available from: https://linkinghub.elsevier.com/retrieve/pii/B9780124160156000046

140. Raggatt LJ, Partridge NC. Cellular and Molecular Mechanisms of Bone Remodeling. Journal of Biological Chemistry. 2010 Aug;285(33):25103–8.

141. McHugh KP, Hodivala-Dilke K, Zheng MH, Namba N, Lam J, Novack D, Feng X, Ross FP, Hynes RO, Teitelbaum SL. Mice lacking β3 integrins are osteosclerotic because of dysfunctional osteoclasts. J Clin Invest. 2000 Feb 15;105(4):433–40.

142. Faccio R, Novack DV, Zallone A, Ross FP, Teitelbaum SL. Dynamic changes in the osteoclast cytoskeleton in response to growth factors and cell attachment are controlled by β3 integrin. The Journal of Cell Biology. 2003 Aug 4;162(3):499–509.

143. Faccio R, Takeshita S, Zallone A, Ross FP, Teitelbaum SL. c-Fms and the αvβ3 integrin collaborate during osteoclast differentiation. J Clin Invest. 2003 Mar 1;111(5):749–58.

144. Blair HC, Teitelbaum SL, Ghiselli R, Gluck S. Osteoclastic Bone Resorption by a Polarized Vacuolar Proton Pump. Science. 1989 Aug 25;245(4920):855–7.

145. Schlesinger PH, Blair HC, Teitelbaum SL, Edwards JC. Characterization of the Osteoclast Ruffled Border Chloride Channel and Its Role in Bone Resorption. Journal of Biological Chemistry. 1997 Jul;272(30):18636–43.

146. Heinemann DEH, Siggelkow H, Ponce LM, Viereck V, Wiese KG, Peters JH. Alkaline Phosphatase Expression during Monocyte Differentiation Overlapping markers as a link between monocytic cells, dendritic cells, osteoclasts and osteoblasts. Immunobiology. 2000 May;202(1):68–81.

147. Kraal G, Rep M, Janse M. Macrophages in T and B Cell Compartments and Other Tissue Macrophages Recognized by Monoclonal Antibody MOMA-2: An Immunohistochemical Study. Scand J Immunol. 1987 Dec;26(6):653–61.

148. Everts V, Delaissé JM, Korper W, Jansen DC, Tigchelaar-Gutter W, Saftig P, Beertsen W. The Bone Lining Cell: Its Role in Cleaning Howship's Lacunae and Initiating Bone Formation. Journal of Bone and Mineral Research. 2002 Jan 1;17(1):77–90.

149. Newby AC. Metalloproteinase Expression in Monocytes and Macrophages and its Relationship to Atherosclerotic Plaque Instability. ATVB. 2008 Dec;28(12):2108–14.

150. Wang Y, Zhou BP. Epithelial-mesenchymal transition in breast cancer progression and metastasis. Chin J Cancer. 2011 Sep 5;30(9):603–11.

151. Mohme M, Riethdorf S, Pantel K. Circulating and disseminated tumour cells — mechanisms of immune surveillance and escape. Nat Rev Clin Oncol. 2017 Mar;14(3):155–67.

152. Gupta GP, Massagué J. Platelets and metastasis revisited: a novel fatty link. J Clin Invest. 2004 Dec 15;114(12):1691–3.

153. Kucia M, Reca R, Miekus K, Wanzeck J, Wojakowski W, Janowska-Wieczorek A, Ratajczak J, Ratajczak MZ. Trafficking of Normal Stem Cells and Metastasis of Cancer Stem Cells Involve Similar Mechanisms: Pivotal Role of the SDF-1–CXCR4 Axis. STEM CELLS. 2005 Aug;23(7):879–94.

154. Miller RJ, Banisadr G, Bhattacharyya BJ. CXCR4 signaling in the regulation of stem cell migration and development. Journal of Neuroimmunology. 2008 Jul;198(1–2):31–8.

155. Rossi D, Zlotnik A. The Biology of Chemokines and their Receptors. Annu Rev Immunol. 2000 Apr;18(1):217–42.

156. De Clercq E. Inhibition of HIV infection by bicyclams, highly potent and specific CXCR4 antagonists. Mol Pharmacol. 2000 May;57(5):833–9.

157. Kang Y, Siegel PM, Shu W, Drobnjak M, Kakonen SM, Cordón-Cardo C, Guise TA, Massagué J. A multigenic program mediating breast cancer metastasis to bone. Cancer Cell. 2003 Jun;3(6):537–49.

158. Furusato B, Rhim JS. CXCR4 and Cancer. In: Fulton AM, editor. Chemokine Receptors in Cancer [Internet]. Totowa, NJ: Humana Press; 2009 [cited 2025 Oct 28]. p. 31–45. Available from: http://link.springer.com/10.1007/978-1-60327-267-4_2

159. Ottewell PD. The role of osteoblasts in bone metastasis. Journal of Bone Oncology. 2016 Sep;5(3):124–7.

160. Maurizi A, Rucci N. The Osteoclast in Bone Metastasis: Player and Target. Cancers (Basel). 2018 Jun 27;10(7):218.

161. Coleman RE. Clinical Features of Metastatic Bone Disease and Risk of Skeletal Morbidity. Clinical Cancer Research. 2006 Oct 15;12(20):6243s–9s.

162. Azuma Y, Kaji K, Katogi R, Takeshita S, Kudo A. Tumor Necrosis Factor-α Induces Differentiation of and Bone Resorption by Osteoclasts. Journal of Biological Chemistry. 2000 Feb;275(7):4858–64.

163. Ell B, Mercatali L, Ibrahim T, Campbell N, Schwarzenbach H, Pantel K, Amadori D, Kang Y. Tumor-Induced Osteoclast miRNA Changes as Regulators and Biomarkers of Osteolytic Bone Metastasis. Cancer Cell. 2013 Oct;24(4):542–56.

164. Lee DY, Deng Z, Wang CH, Yang BB. MicroRNA-378 promotes cell survival, tumor growth, and angiogenesis by targeting SuFu and Fus-1 expression. Proc Natl Acad Sci USA. 2007 Dec 18;104(51):20350–5.

165. Frankel LB, Christoffersen NR, Jacobsen A, Lindow M, Krogh A, Lund AH. Programmed Cell Death 4 (PDCD4) Is an Important Functional Target of the MicroRNA miR-21 in Breast Cancer Cells. Journal of Biological Chemistry. 2008 Jan;283(2):1026–33.

166. Lu X, Mu E, Wei Y, Riethdorf S, Yang Q, Yuan M, Yan J, Hua Y, Tiede BJ, Lu X, Haffty BG, Pantel K, Massagué J, Kang Y. VCAM-1 Promotes Osteolytic Expansion of Indolent Bone Micrometastasis of Breast Cancer by Engaging α4β1-Positive Osteoclast Progenitors. Cancer Cell. 2011 Dec;20(6):701–14.

167. Käkönen SM, Selander KS, Chirgwin JM, Yin JJ, Burns S, Rankin WA, Grubbs BG, Dallas M, Cui Y, Guise TA. Transforming Growth Factor-β Stimulates Parathyroid Hormone-related Protein and Osteolytic Metastases via Smad and Mitogen-activated Protein Kinase Signaling Pathways. Journal of Biological Chemistry. 2002 Jul;277(27):24571–8.

168. Sanders JL, Chattopadhyay N, Kifor O, Yamaguchi T, Butters RR, Brown EM. Extracellular Calcium-Sensing Receptor Expression and Its Potential Role in Regulating Parathyroid Hormone-Related Peptide Secretion in Human Breast Cancer Cell Lines*. Endocrinology. 2000 Dec 1;141(12):4357–64.

169. Domchek SM, Younger J, Finkelstein DM, Seiden MV. Predictors of skeletal complications in patients with metastatic breast carcinoma. Cancer. 2000 Jul 15;89(2):363–8.

170. Gül G, Sendur MAN, Aksoy S, Sever AR, Altundag K. A comprehensive review of denosumab for bone metastasis in patients with solid tumors. Current Medical Research and Opinion. 2016 Jan 2;32(1):133–45.

171. Russell RGG, Watts NB, Ebetino FH, Rogers MJ. Mechanisms of action of bisphosphonates: similarities and differences and their potential influence on clinical efficacy. Osteoporos Int. 2008 Jun;19(6):733–59.

172. Qu W, Chen WH, Kuang Y, Zeng X, Cheng SX, Zhou X, Zhuo RX, Zhang XZ. Avidin–Biotin Interaction Mediated Peptide Assemblies as Efficient Gene Delivery Vectors for Cancer Therapy. Mol Pharmaceutics. 2013 Jan 7;10(1):261–9.

173. Hauser PV, Pippin JW, Kaiser C, Krofft RD, Brinkkoetter PT, Hudkins KL, Kerjaschki D, Reiser J, Alpers CE, Shankland SJ. Novel siRNA Delivery System to Target Podocytes In Vivo. Zoccali C, editor. PLoS ONE. 2010 Mar 1;5(3):e9463.

174. Kuan SL, Fischer S, Hafner S, Wang T, Syrovets T, Liu W, Tokura Y, Ng DYW, Riegger A, Förtsch C, Jäger D, Barth TFE, Simmet T, Barth H, Weil T. Boosting Antitumor Drug Efficacy with Chemically Engineered Multidomain Proteins. Advanced Science. 2018 Aug;5(8):1701036.

175. Livnah O, Bayer EA, Wilchek M, Sussman JL. Three-dimensional structures of avidin and the avidin-biotin complex. Proc Natl Acad Sci USA. 1993 Jun;90(11):5076–80.

176. Dakshinamurti K. Biotin — a regulator of gene expression. The Journal of Nutritional Biochemistry. 2005 Jul;16(7):419–23.

177. González M, Argaraña CE, Fidelio GD. Extremely high thermal stability of streptavidin and avidin upon biotin binding. Biomolecular Engineering. 1999 Dec;16(1–4):67–72.

178. Rybak J, Scheurer SB, Neri D, Elia G. Purification of biotinylated proteins on streptavidin resin: A protocol for quantitative elution. Proteomics. 2004 Aug;4(8):2296–9.

179. Duhamel RC, Whitehead JS. Prevention of nonspecific binding of avidin. In: Methods in Enzymology [Internet]. Elsevier; 1990 [cited 2025 Nov 7]. p. 201–7. Available from: https://linkinghub.elsevier.com/retrieve/pii/007668799084275L

180. Bubb MO, Green F, Conradie JD, Tchernyshev B, Bayer EA, Wilchek M. Natural antibodies to avidin in human serum. Immunology Letters. 1993 Mar;35(3):277–80.

181. Chinol M, Casalini P, Maggiolo M, Canevari S, Omodeo E, Caliceti P, Veronese F, Cremonesi M, Chiolerio F, Nardone E, Siccardi A, Paganelli G. Biochemical modifications of avidin improve pharmacokinetics and biodistribution, and reduce immunogenicity. Br J Cancer. 1998 Jul;78(2):189–97.

182. Cox JE, Cheng TL. Egg-based Vaccines. Pediatrics In Review. 2006 Mar 1;27(3):118–9.

183. Petronzelli F, Pelliccia A, Anastasi AM, Lindstedt R, Manganello S, Ferrari LE, Albertoni C, Leoni B, Rosi A, D'Alessio V, Deiana K, Paganelli G, De Santis R. Therapeutic Use of Avidin Is Not Hampered by Antiavidin Antibodies in Humans. Cancer Biotherapy and Radiopharmaceuticals. 2010 Oct;25(5):563–70.

184. Vermette P, Gengenbach T, Divisekera U, Kambouris PA, Griesser HJ, Meagher L. Immobilization and surface characterization of NeutrAvidin biotin-binding protein on different hydrogel interlayers. Journal of Colloid and Interface Science. 2003 Mar;259(1):13–26.

185. Tausig F, Wolf FJ. Streptavidin—A substance with avidin-like properties produced by microorganisms. Biochemical and Biophysical Research Communications. 1964 Jan;14(3):205–9.

186. Helppolainen SH, Määttä JAE, Halling KK, Slotte JP, Hytönen VP, Jänis J, Vainiotalo P, Kulomaa MS, Nordlund HR. Bradavidin II from Bradyrhizobium japonicum: A new avidin-like biotin-binding protein. Biochimica et Biophysica Acta (BBA) - Proteins and Proteomics. 2008 Jul;1784(7–8):1002–10.

187. Stadler N, Gao B, Silva MJ, Borho J, Haunschild E, Koynov K, Haffner-Luntzer M, Ignatius A, Weidinger G, Kuan SL, Weil T, Barth H. Multifunctional Peptide-Based Biohybrid for Targeted Reduction of Metastatic Breast Carcinoma-Associated Osteolysis. JFB. 2025 Oct 25;16(11):399.

188. Harms M, Fabech Hansson R, Gilg A, Almeida-Hernández Y, Löffler J, Rodríguez-Alfonso A, Habib MMW, Albers D, Ahmed NS, Abadi AH, Winter G, Rasche V, Beer AJ, Weidinger G, Preising N, Ständker L, Wiese S, Sanchez-Garcia E, Zelikin AN, Münch J. Development of N-Terminally Modified Variants of the CXCR4-Antagonistic Peptide EPI-X4 for Enhanced Plasma Stability. J Med Chem. 2023 Nov 23;66(22):15189–204.

189. Jansen Ruud, Embden JanDAV, Gaastra Wim, Schouls LeoM. Identification of genes that are associated with DNA repeats in prokaryotes. Molecular Microbiology. 2002 Mar;43(6):1565–75.

190. Garneau JE, Dupuis MÈ, Villion M, Romero DA, Barrangou R, Boyaval P, Fremaux C, Horvath P, Magadán AH, Moineau S. The CRISPR/Cas bacterial immune system cleaves bacteriophage and plasmid DNA. Nature. 2010 Nov 4;468(7320):67–71.

191. Barrangou R, Fremaux C, Deveau H, Richards M, Boyaval P, Moineau S, Romero DA, Horvath P. CRISPR Provides Acquired Resistance Against Viruses in Prokaryotes. Science. 2007 Mar 23;315(5819):1709–12.

192. Mojica FJM, Díez-Villaseñor C, Soria E, Juez G. Biological significance of a family of regularly spaced repeats in the genomes of Archaea, Bacteria and mitochondria. Molecular Microbiology. 2000 Apr;36(1):244–6.

193. Ishino Y, Shinagawa H, Makino K, Amemura M, Nakata A. Nucleotide sequence of the iap gene, responsible for alkaline phosphatase isozyme conversion in Escherichia coli, and identification of the gene product. J Bacteriol. 1987 Dec;169(12):5429–33.

194. Hermans PW, Van Soolingen D, Bik EM, De Haas PE, Dale JW, Van Embden JD. Insertion element IS987 from Mycobacterium bovis BCG is located in a hot-spot integration region for insertion elements in Mycobacterium tuberculosis complex strains. Infect Immun. 1991 Aug;59(8):2695–705.

195. Mojica FJM, Juez G, Rodriguez-Valera F. Transcription at different salinities of *Haloferax mediterranei* sequences adjacent to partially modified *Pst* I sites. Molecular Microbiology. 1993 Aug;9(3):613–21.

196. Deltcheva E, Chylinski K, Sharma CM, Gonzales K, Chao Y, Pirzada ZA, Eckert MR, Vogel J, Charpentier E. CRISPR RNA maturation by trans-encoded small RNA and host factor RNase III. Nature. 2011 Mar;471(7340):602–7.

197. Sinkunas T, Gasiunas G, Fremaux C, Barrangou R, Horvath P, Siksnys V. Cas3 is a single-stranded DNA nuclease and ATP-dependent helicase in the CRISPR/Cas immune system: Cas3 nuclease/helicase. The EMBO Journal. 2011 Apr 6;30(7):1335–42.

198. Mulepati S, Bailey S. Structural and Biochemical Analysis of Nuclease Domain of Clustered Regularly Interspaced Short Palindromic Repeat (CRISPR)-associated Protein 3 (Cas3). Journal of Biological Chemistry. 2011 Sep;286(36):31896–903.

199. Beloglazova N, Petit P, Flick R, Brown G, Savchenko A, Yakunin AF. Structure and activity of the Cas3 HD nuclease MJ0384, an effector enzyme of the CRISPR interference: CRISPR-associated Cas3 nuclease MJ0384. The EMBO Journal. 2011 Nov 16;30(22):4616–27.

200. Makarova KS, Koonin EV. Annotation and Classification of CRISPR-Cas Systems. In: Lundgren M, Charpentier E, Fineran PC, editors. CRISPR [Internet]. New York, NY: Springer New York; 2015 [cited 2025 Nov 18]. p. 47–75. (Methods in Molecular

Biology; vol. 1311). Available from: https://link.springer.com/10.1007/978-1-4939-2687-9_4

201. Makarova KS, Aravind L, Wolf YI, Koonin EV. Unification of Cas protein families and a simple scenario for the origin and evolution of CRISPR-Cas systems. Biol Direct. 2011 Dec;6(1):38.

202. Cocozaki AI, Ramia NF, Shao Y, Hale CR, Terns RM, Terns MP, Li H. Structure of the Cmr2 Subunit of the CRISPR-Cas RNA Silencing Complex. Structure. 2012 Mar;20(3):545–53.

203. Zhu X, Ye K. Crystal structure of Cmr2 suggests a nucleotide cyclase-related enzyme in type III CRISPR-Cas systems. FEBS Letters. 2012 Mar 23;586(6):939–45.

204. Jinek M, Chylinski K, Fonfara I, Hauer M, Doudna JA, Charpentier E. A Programmable Dual-RNA–Guided DNA Endonuclease in Adaptive Bacterial Immunity. Science. 2012 Aug 17;337(6096):816–21.

205. Brouns SJJ, Jore MM, Lundgren M, Westra ER, Slijkhuis RJH, Snijders APL, Dickman MJ, Makarova KS, Koonin EV, Van Der Oost J. Small CRISPR RNAs Guide Antiviral Defense in Prokaryotes. Science. 2008 Aug 15;321(5891):960–4.

206. Shen B, Zhang J, Wu H, Wang J, Ma K, Li Z, Zhang X, Zhang P, Huang X. Generation of gene-modified mice via Cas9/RNA-mediated gene targeting. Cell Res. 2013 May;23(5):720–3.

207. Genetic scissors: a tool for rewriting the code of life. [cited 2025 Nov 17]; Available from: https://www.nobelprize.org/prizes/chemistry/2020/press-release/

208. Davis L, Maizels N. Homology-directed repair of DNA nicks via pathways distinct from canonical double-strand break repair. Proc Natl Acad Sci USA. 2014 Mar 11;111(10):E924-932.

209. Andres SN, Vergnes A, Ristic D, Wyman C, Modesti M, Junop M. A human XRCC4–XLF complex bridges DNA. Nucleic acids research. 2012;40(4):1868–78.

210. Hendrickson EA. Cell-cycle regulation of mammalian DNA double-strand-break repair. Am J Hum Genet. 1997 Oct;61(4):795–800.

211. Lieber MR, Gu J, Lu H, Shimazaki N, Tsai AG. Nonhomologous DNA End Joining (NHEJ) and Chromosomal Translocations in Humans. In: Nasheuer HP, editor. Genome Stability and Human Diseases [Internet]. Dordrecht: Springer Netherlands; 2010. p. 279–96. Available from: https://doi.org/10.1007/978-90-481-3471-7_14

212. Ghezraoui H, Piganeau M, Renouf B, Renaud JB, Sallmyr A, Ruis B, Oh S, Tomkinson AE, Hendrickson EA, Giovannangeli C, Jasin M, Brunet E. Chromosomal Translocations in Human Cells Are Generated by Canonical Nonhomologous End-Joining. Molecular Cell. 2014 Sep;55(6):829–42.

213. Lieber MR. The Mechanism of Double-Strand DNA Break Repair by the Nonhomologous DNA End-Joining Pathway. Annu Rev Biochem. 2010 Jun 7;79(1):181–211.

214. Ran FA, Hsu PD, Wright J, Agarwala V, Scott DA, Zhang F. Genome engineering using the CRISPR-Cas9 system. Nat Protoc. 2013 Nov;8(11):2281–308.

215. Dugger BN, Dickson DW. Pathology of Neurodegenerative Diseases. Cold Spring Harb Perspect Biol. 2017 Jul;9(7):a028035.

216. Lu L, Yu X, Cai Y, Sun M, Yang H. Application of CRISPR/Cas9 in Alzheimer's Disease. Front Neurosci. 2021 Dec 21;15:803894.

217. Yang W, Liu Y, Tu Z, Xiao C, Yan S, Ma X, Guo X, Chen X, Yin P, Yang Z, Yang S, Jiang T, Li S, Qin C, Li XJ. CRISPR/Cas9-mediated PINK1 deletion leads to neurodegeneration in rhesus monkeys. Cell Res. 2019 Apr;29(4):334–6.

218. Yan S, Tu Z, Liu Z, Fan N, Yang H, Yang S, Yang W, Zhao Y, Ouyang Z, Lai C, Yang H, Li L, Liu Q, Shi H, Xu G, Zhao H, Wei H, Pei Z, Li S, Lai L, Li XJ. A Huntingtin Knockin Pig Model Recapitulates Features of Selective Neurodegeneration in Huntington's Disease. Cell. 2018 May;173(4):989-1002.e13.

219. Liu N, Olson EN. CRISPR Modeling and Correction of Cardiovascular Disease. Circulation Research. 2022 Jun 10;130(12):1827–50.

220. Simeonov DR, Gowen BG, Boontanrart M, Roth TL, Gagnon JD, Mumbach MR, Satpathy AT, Lee Y, Bray NL, Chan AY, Lituiev DS, Nguyen ML, Gate RE, Subramaniam M, Li Z, Woo JM, Mitros T, Ray GJ, Curie GL, Naddaf N, Chu JS, Ma H, Boyer E, Van Gool F, Huang H, Liu R, Tobin VR, Schumann K, Daly MJ, Farh KK, Ansel KM, Ye CJ, Greenleaf WJ, Anderson MS, Bluestone JA, Chang HY, Corn JE, Marson A. Discovery of stimulation-responsive immune enhancers with CRISPR activation. Nature. 2017 Sep 7;549(7670):111–5.

221. Koo T, Yoon AR, Cho HY, Bae S, Yun CO, Kim JS. Selective disruption of an oncogenic mutant allele by CRISPR/Cas9 induces efficient tumor regression. Nucleic Acids Research. 2017 Jul 27;45(13):7897–908.

222. Singh A, Irfan H, Fatima E, Nazir Z, Verma A, Akilimali A. Revolutionary breakthrough: FDA approves CASGEVY, the first CRISPR/Cas9 gene therapy for sickle cell disease. Annals of Medicine & Surgery. 2024 Aug;86(8):4555–9.

223. Fu Y, Foden JA, Khayter C, Maeder ML, Reyon D, Joung JK, Sander JD. High-frequency off-target mutagenesis induced by CRISPR-Cas nucleases in human cells. Nat Biotechnol. 2013 Sep;31(9):822–6.

224. Wu X, Scott DA, Kriz AJ, Chiu AC, Hsu PD, Dadon DB, Cheng AW, Trevino AE, Konermann S, Chen S, Jaenisch R, Zhang F, Sharp PA. Genome-wide binding of the CRISPR endonuclease Cas9 in mammalian cells. Nat Biotechnol. 2014 Jul;32(7):670–6.

225. Seijas A, Cora D, Novo M, Al-Soufi W, Sánchez L, Arana ÁJ. CRISPR/Cas9 Delivery Systems to Enhance Gene Editing Efficiency. IJMS. 2025 May 6;26(9):4420.

226. Chen S, Jiao Y, Pan F, Guan Z, Cheng SH, Sun D. Knock-In of a Large Reporter Gene via the High-Throughput Microinjection of the CRISPR/Cas9 System. IEEE Trans Biomed Eng. 2022 Aug;69(8):2524–32.

227. Kanefuji T, Yokoo T, Suda T, Abe H, Kamimura K, Liu D. Hemodynamics of a hydrodynamic injection. Molecular Therapy - Methods & Clinical Development. 2014;1:14029.

228. Niola F, Dagnæs-Hansen F, Frödin M. In Vivo Editing of the Adult Mouse Liver Using CRISPR/Cas9 and Hydrodynamic Tail Vein Injection. In: Luo Y, editor. CRISPR Gene Editing [Internet]. New York, NY: Springer New York; 2019 [cited 2025 Nov 19]. p. 329–41. (Methods in Molecular Biology; vol. 1961). Available from: http://link.springer.com/10.1007/978-1-4939-9170-9_20

229. Warrington KH, Herzog RW. Treatment of human disease by adeno-associated viral gene transfer. Hum Genet. 2006 Jul;119(6):571–603.

230. Naso MF, Tomkowicz B, Perry WL, Strohl WR. Adeno-Associated Virus (AAV) as a Vector for Gene Therapy. BioDrugs. 2017 Aug;31(4):317–34.

231. Li C, Samulski RJ. Engineering adeno-associated virus vectors for gene therapy. Nat Rev Genet. 2020 Apr;21(4):255–72.

232. Moffa JC, Bland IN, Tooley JR, Kalyanaraman V, Heitmeier M, Creed MC, Copits BA. Cell-Specific Single Viral Vector CRISPR/Cas9 Editing and Genetically Encoded Tool Delivery in the Central and Peripheral Nervous Systems. eNeuro. 2024 Jul;11(7):ENEURO.0438-23.2024.

233. Follenzi A, Sabatino G, Lombardo A, Boccaccio C, Naldini L. Efficient Gene Delivery and Targeted Expression to Hepatocytes *In Vivo* by Improved Lentiviral Vectors. Human Gene Therapy. 2002 Jan 20;13(2):243–60.

234. Wang M, Zuris JA, Meng F, Rees H, Sun S, Deng P, Han Y, Gao X, Pouli D, Wu Q, Georgakoudi I, Liu DR, Xu Q. Efficient delivery of genome-editing proteins using bioreducible lipid nanoparticles. Proc Natl Acad Sci USA. 2016 Mar 15;113(11):2868–73.

235. Kulkarni JA, Myhre JL, Chen S, Tam YYC, Danescu A, Richman JM, Cullis PR. Design of lipid nanoparticles for in vitro and in vivo delivery of plasmid DNA. Nanomedicine: Nanotechnology, Biology and Medicine. 2017 May;13(4):1377–87.

236. Yoo J, Park C, Yi G, Lee D, Koo H. Active Targeting Strategies Using Biological Ligands for Nanoparticle Drug Delivery Systems. Cancers. 2019 May 8;11(5):640.

237. Liu BY, He XY, Zhuo RX, Cheng SX. Tumor targeted genome editing mediated by a multi-functional gene vector for regulating cell behaviors. Journal of Controlled Release. 2018 Dec;291:90–8.

238. Karp H, Zoltek M, Wasko K, Vazquez AL, Brim J, Ngo W, Schepartz A, Doudna JA. Packaged delivery of CRISPR–Cas9 ribonucleoproteins accelerates genome editing. Nucleic Acids Research. 2025 Feb 27;53(5):gkaf105.

239. Bamundo M, Palumbo S, D'Auria L, Missero C, Di Girolamo D. CRISPR/Cas9 Ribonucleoprotein Nucleofection for Genome Editing in Primary Human Keratinocytes: Knockouts, Deletions, and Homology-Directed Repair Mutagenesis. Current Protocols. 2024 Nov;4(11):e70056.

240. Christenson AE, Divekar NS, Hernández Zamora MG, Nguyen CD, Nuñez JK. CRISPR Epigenome Editing in Human Cells using Plasmid DNA Transfection and mRNA Nucleofection Delivery. JoVE. 2025 May 30;(219):68089.

241. Adam SA, Lobl TJ, Mitchell MA, Gerace L. Identification of specific binding proteins for a nuclear location sequence. Nature. 1989 Jan;337(6204):276–9.

242. Stewart M. Molecular mechanism of the nuclear protein import cycle. Nat Rev Mol Cell Biol. 2007 Mar;8(3):195–208.

243. Zhang W, Wang H, Luo Z, Jian Y, Gong C, Wang H, Lin X, Liu M, Wang Y, Shao H. Hitchhiking of Cas9 with nucleus-localized proteins impairs its controllability and leads to efficient genome editing of NLS-free Cas9. Molecular Therapy. 2024 Apr;32(4):920–34.

244. Hu JH, Miller SM, Geurts MH, Tang W, Chen L, Sun N, Zeina CM, Gao X, Rees HA, Lin Z, Liu DR. Evolved Cas9 variants with broad PAM compatibility and high DNA specificity. Nature. 2018 Apr;556(7699):57–63.

245. Fleming J, Magana P, Nair S, Tsenkov M, Bertoni D, Pidruchna I, Lima Afonso MQ, Midlik A, Paramval U, Žídek A, Laydon A, Kovalevskiy O, Pan J, Cheng J, Avsec Ž, Bycroft C, Wong LH, Last M, Mirdita M, Steinegger M, Kohli P, Váradi M, Velankar S. AlphaFold Protein Structure Database and 3D-Beacons: New Data and Capabilities. Journal of Molecular Biology. 2025 Aug;437(15):168967.

246. Schultze JL, Schmieder A, Goerdt S. Macrophage activation in human diseases. Seminars in Immunology. 2015 Aug;27(4):249–56.

247. Ginhoux F, Jung S. Monocytes and macrophages: developmental pathways and tissue homeostasis. Nat Rev Immunol. 2014 Jun;14(6):392–404.

248. Murray PJ. Immune regulation by monocytes. Seminars in Immunology. 2018 Feb;35:12–8.

249. Luo YL, Xu CF, Li HJ, Cao ZT, Liu J, Wang JL, Du XJ, Yang XZ, Gu Z, Wang J. Macrophage-Specific *in Vivo* Gene Editing Using Cationic Lipid-Assisted Polymeric Nanoparticles. ACS Nano. 2018 Feb 27;12(2):994–1005.

250. Freund EC, Lock JY, Oh J, Maculins T, Delamarre L, Bohlen CJ, Haley B, Murthy A. Efficient gene knockout in primary human and murine myeloid cells by non-viral

delivery of CRISPR-Cas9. Journal of Experimental Medicine. 2020 Jul 6;217(7):e20191692.

251. Laoharawee K, Johnson MJ, Lahr WS, Sipe CJ, Kleinboehl E, Peterson JJ, Lonetree C lin, Bell JB, Slipek NJ, Crane AT, Webber BR, Moriarity BS. A Pan-RNase Inhibitor Enabling CRISPR-mRNA Platforms for Engineering of Primary Human Monocytes. IJMS. 2022 Aug 28;23(17):9749.

252. Haffner-Luntzer M, Heilmann A, Rapp AE, Roessler R, Schinke T, Amling M, Ignatius A, Liedert A. Antagonizing midkine accelerates fracture healing in mice by enhanced bone formation in the fracture callus. British J Pharmacology. 2016 Jul;173(14):2237–49.

253. Diehm J. Optimization of the purification of CysC3bot1 in Escherichia coli BL21 (unpublished, bachelors thesis under supervision of Nicole Stadler). 2022.

254. Pugliese L, Coda A, Malcovati M, Bolognesi M. Three-dimensional Structure of the Tetragonal Crystal Form of Egg-white Avidin in its functional Complex with Biotin at 2·7 Å Resolution. Journal of Molecular Biology. 1993 Jun;231(3):698–710.

255. McGonigle P. How Biologics Have Changed the Drug Discovery Landscape. Annual Review of Pharmacology and Toxicology. 2025 Jan 23;65(1):29–46.

256. Moreland LW, Baumgartner SW, Schiff MH, Tindall EA, Fleischmann RM, Weaver AL, Ettlinger RE, Cohen S, Koopman WJ, Mohler K, Widmer MB, Blosch CM. Treatment of Rheumatoid Arthritis with a Recombinant Human Tumor Necrosis Factor Receptor (p75)–Fc Fusion Protein. N Engl J Med. 1997 Jul 17;337(3):141–7.

257. Bruce VJ, McNaughton BR. Inside Job: Methods for Delivering Proteins to the Interior of Mammalian Cells. Cell Chemical Biology. 2017 Aug;24(8):924–34.

258. Dominguez R, Holmes KC. Actin Structure and Function. Annu Rev Biophys. 2011 Jun 9;40(1):169–86.

259. Gibieža P, Petrikaitė V. The regulation of actin dynamics during cell division and malignancy. Am J Cancer Res. 2021;11(9):4050–69.

260. Begum R, Nur-E-Kamal MSA, Zaman M. The role of Rho GTPases in the regulation of the rearrangement of actin cytoskeleton and cell movement. Exp Mol Med. 2004 Aug 1;36(4):358–66.

261. Itoh K, Yoshioka K, Akedo H, Uehata M, Ishizaki T, Narumiya S. An essential part for Rho–associated kinase in the transcellular invasion of tumor cells. Nat Med. 1999 Feb;5(2):221–5.

262. Somlyo AV, Bradshaw D, Ramos S, Murphy C, Myers CE, Somlyo AP. Rho-Kinase Inhibitor Retards Migration and in Vivo Dissemination of Human Prostate Cancer Cells. Biochemical and Biophysical Research Communications. 2000 Mar;269(3):652–9.

263. Dai X, Li T, Bai Z, Yang Y, Liu X, Zhan J, Shi B. Breast cancer intrinsic subtype classification, clinical use and future trends. Am J Cancer Res. 2015;5(10):2929–43.

264. Carey LA, Perou CM, Livasy CA, Dressler LG, Cowan D, Conway K, Karaca G, Troester MA, Tse CK, Edmiston S, Deming SL, Geradts J, Cheang MCU, Nielsen TO, Moorman PG, Earp HS, Millikan RC. Race, Breast Cancer Subtypes, and Survival in the Carolina Breast Cancer Study. JAMA. 2006 Jun 7;295(21):2492.

265. Brenton JD, Carey LA, Ahmed AA, Caldas C. Molecular Classification and Molecular Forecasting of Breast Cancer: Ready for Clinical Application? JCO. 2005 Oct 10;23(29):7350–60.

266. Schmid BC, Rudas M, Rezniczek GA, Leodolter S, Zeillinger R. CXCR4 is Expressed in Ductal Carcinoma in situ of the Breast and in Atypical Ductal Hyperplasia. Breast Cancer Res Treat. 2004 Apr;84(3):247–50.

267. Kalatskaya I, Berchiche YA, Gravel S, Limberg BJ, Rosenbaum JS, Heveker N. AMD3100 Is a CXCR7 Ligand with Allosteric Agonist Properties. Molecular Pharmacology. 2009 May;75(5):1240–7.

268. Gravel S, Malouf C, Boulais PE, Berchiche YA, Oishi S, Fujii N, Leduc R, Sinnett D, Heveker N. The Peptidomimetic CXCR4 Antagonist TC14012 Recruits β-Arrestin to CXCR7. Journal of Biological Chemistry. 2010 Dec;285(49):37939–43.

269. Yang Y, Guo Y, Tan S, Ke B, Tao J, Liu H, Jiang J, Chen J, Chen G, Wu B. β-Arrestin1 enhances hepatocellular carcinogenesis through inflammation-mediated Akt signalling. Nat Commun. 2015 Jun 16;6(1):7369.

270. Xu S, Tang J, Wang C, Liu J, Fu Y, Luo Y. CXCR7 promotes melanoma tumorigenesis via Src kinase signaling. Cell Death Dis. 2019 Feb 25;10(3):191.

271. Nguyen HT, Reyes-Alcaraz A, Yong HJ, Nguyen LP, Park HK, Inoue A, Lee CS, Seong JY, Hwang JI. CXCR7: a β-arrestin-biased receptor that potentiates cell migration and recruits β-arrestin2 exclusively through Gβγ subunits and GRK2. Cell Biosci. 2020 Dec;10(1):134.

272. Sokkar P, Harms M, Stürzel C, Gilg A, Kizilsavas G, Raasholm M, Preising N, Wagner M, Kirchhoff F, Ständker L, Weidinger G, Mayer B, Münch J, Sanchez-Garcia E. Computational modeling and experimental validation of the EPI-X4/CXCR4 complex allows rational design of small peptide antagonists. Commun Biol. 2021 Sep 22;4(1):1113.

273. Green NM. Avidin. In: Advances in Protein Chemistry [Internet]. Elsevier; 1975 [cited 2025 Dec 19]. p. 85–133. Available from: https://linkinghub.elsevier.com/retrieve/pii/S0065323308604118

274. Sut TN, Park H, Koo DJ, Yoon BK, Jackman JA. Distinct Binding Properties of Neutravidin and Streptavidin Proteins to Biotinylated Supported Lipid Bilayers: Implications for Sensor Functionalization. Sensors. 2022 Jul 11;22(14):5185.

275. Balzer AHA, Whitehurst CB. An Analysis of the Biotin–(Strept)avidin System in Immunoassays: Interference and Mitigation Strategies. CIMB. 2023 Oct 31;45(11):8733–54.

276. Gačanin J, Kovtun A, Fischer S, Schwager V, Quambusch J, Kuan SL, Liu W, Boldt F, Li C, Yang Z, Liu D, Wu Y, Weil T, Barth H, Ignatius A. Spatiotemporally Controlled Release of Rho-Inhibiting C3 Toxin from a Protein–DNA Hybrid Hydrogel for Targeted Inhibition of Osteoclast Formation and Activity. Adv Healthcare Materials. 2017 Nov;6(21):1700392.

277. Skjødt MK, Frost M, Abrahamsen B. Side effects of drugs for osteoporosis and metastatic bone disease. Brit J Clinical Pharma. 2019 Jun;85(6):1063–71.

278. Komori T. Cbfa1/Runx2, an essential transcription factor for the regulation of osteoblast differentiation. Nihon Rinsho. 2002 Mar;60 Suppl 3:91–7.

279. Zainal Ariffin SH, Lim KW, Megat Abdul Wahab R, Zainal Ariffin Z, Rus Din RD, Shahidan MA, Johari AN, Zainol Abidin IZ. Gene expression profiles for in vitro human stem cell differentiation into osteoblasts and osteoclasts: a systematic review. PeerJ. 2022;10:e14174.

280. Huang W, Yang S, Shao J, Li YP. Signaling and transcriptional regulation in osteoblast commitment and differentiation. Front Biosci. 2007 May 1;12:3068–92.

281. Franceschi RT, Iyer BS. Relationship between collagen synthesis and expression of the osteoblast phenotype in MC3T3-E1 cells. Journal of Bone and Mineral Research. 1992 Feb 1;7(2):235–46.

282. Scholzen T, Gerdes J. The Ki-67 protein: From the known and the unknown. J Cell Phys. 2000 Mar;182(3):311–22.

283. Augat P, Schorlemmer S. The role of cortical bone and its microstructure in bone strength. Age and Ageing. 2006 Sep 1;35(suppl_2):ii27–31.

284. Öhman-Mägi C, Holub O, Wu D, Hall RM, Persson C. Density and mechanical properties of vertebral trabecular bone—A review. JOR Spine. 2021 Dec;4(4):e1176.

285. Mercatali L, La Manna F, Miserocchi G, Liverani C, De Vita A, Spadazzi C, Bongiovanni A, Recine F, Amadori D, Ghetti M, Ibrahim T. Tumor-Stroma Crosstalk in Bone Tissue: The Osteoclastogenic Potential of a Breast Cancer Cell Line in a Co-Culture System and the Role of EGFR Inhibition. Int J Mol Sci. 2017 Jul 29;18(8):1655.

286. Liu K, Newbury PA, Glicksberg BS, Zeng WZD, Paithankar S, Andrechek ER, Chen B. Evaluating cell lines as models for metastatic breast cancer through integrative analysis of genomic data. Nat Commun. 2019 May 15;10(1):2138.

287. Glaser DE, Curtis MB, Sariano PA, Rollins ZA, Shergill BS, Anand A, Deely AM, Shirure VS, Anderson L, Lowen JM, Ng NR, Weilbaecher K, Link DC, George SC. Organ-on-a-chip model of vascularized human bone marrow niches. Biomaterials. 2022 Jan;280:121245.

288. Crippa M, Talò G, Lamouline A, Bolis S, Arrigoni C, Bersini S, Moretti M. A microfluidic model of human vascularized breast cancer metastasis to bone for the study of neutrophil-cancer cell interactions. Materials Today Bio. 2022 Dec;17:100460.

289. Bogusiewicz A, Mock NI, Mock DM. Instability of the biotin–protein bond in human plasma. Analytical Biochemistry. 2004 Apr;327(2):156–61.

290. Harms M, Haase A, Rodríguez-Alfonso A, Löffler J, Almeida-Hernández Y, Ruiz-Blanco YB, Albers D, Gilg A, Von Bank F, Zech F, Groß R, Datta M, Jaikishan J, Draphoen B, Habib M, Ständker L, Wiese S, Lindén M, Winter G, Rasche V, Beer AJ, Jumaa H, Abadi AH, Kirchhoff F, Busch M, Dünker N, Sanchez-Garcia E, Münch J. Fatty acid conjugated EPI-X4 derivatives with increased activity and in vivo stability. Journal of Controlled Release. 2024 Sep;373:583–98.

291. Chen LN, Fan XY, Liu YT, Chen SQ, Xie FY, Zeng L, Wen J, Li J, Ma JY, Ou XH, Luo SM, Guo L. High-Survival Rate After Microinjection of Mouse Oocytes and Early Embryos With mRNA by Combining a Tip Pipette and Piezoelectric-Assisted Micromanipulator. Front Cell Dev Biol. 2021 Sep 3;9:735971.

292. Hashimoto M, Takemoto T. Erratum: Electroporation enables the efficient mRNA delivery into the mouse zygotes and facilitates CRISPR/Cas9-based genome editing. Sci Rep. 2015 Aug 5;5(1):12658.

293. Fry WJ, Wulff VJ, Tucker D, Fry FJ. Physical Factors Involved in Ultrasonically Induced Changes in Living Systems: I. Identification of Non-Temperature Effects. The Journal of the Acoustical Society of America. 1950 Nov 1;22(6):867–76.

294. Coroadinha AS. Host Cell Restriction Factors Blocking Efficient Vector Transduction: Challenges in Lentiviral and Adeno-Associated Vector Based Gene Therapies. Cells. 2023 Feb 24;12(5):732.

295. Milne JC, Blanket SR, Hanna PC, Collier RJ. Protective antigen-binding domain of anthrax lethal factor mediates translocation of a heterologous protein fused to its amino- or carboxy-terminus. Molecular Microbiology. 1995 Feb;15(4):661–6.

296. Beitzinger C, Stefani C, Kronhardt A, Rolando M, Flatau G, Lemichez E, Benz R. Role of N-Terminal His6-Tags in Binding and Efficient Translocation of Polypeptides into Cells Using Anthrax Protective Antigen (PA). Bravo A, editor. PLoS ONE. 2012 Oct 8;7(10):e46964.

297. Heber S, Borho J, Stadler N, Wondany F, König I, Michaelis J, Papatheodorou P, Barth H, Fellermann M. The Clostridium botulinum C2 Toxin Subunit C2IIa Delivers Enzymes with Positively Charged N-Termini into the Cytosol of Target Cells. Toxins. 2023 Jun 9;15(6):390.

298. Barth H, Blöcker D, Behlke J, Bergsma-Schutter W, Brisson A, Benz R, Aktories K. Cellular Uptake of Clostridium botulinum C2 Toxin Requires Oligomerization and Acidification. Journal of Biological Chemistry. 2000 Jun;275(25):18704–11.

299. Jiang J, Pentelute BL, Collier RJ, Zhou ZH. Atomic structure of anthrax protective antigen pore elucidates toxin translocation. Nature. 2015 May 28;521(7553):545–9.

300. Zornetta I, Brandi L, Janowiak B, Dal Molin F, Tonello F, Collier RJ, Montecucco C. Imaging the cell entry of the anthrax oedema and lethal toxins with fluorescent

protein chimeras: Imaging of anthrax toxins with fluorescent chimeras. Cellular Microbiology. 2010 Oct;12(10):1435–45.

301. Hirschenberger M, Stadler N, Fellermann M, Sparrer KMJ, Kirchhoff F, Barth H, Papatheodorou P. CRISPA: A Non-viral, Transient Cas9 Delivery System Based on Reengineered Anthrax Toxin. Front Pharmacol. 2021 Oct 18;12:770283.

302. Zuris JA, Thompson DB, Shu Y, Guilinger JP, Bessen JL, Hu JH, Maeder ML, Joung JK, Chen ZY, Liu DR. Cationic lipid-mediated delivery of proteins enables efficient protein-based genome editing in vitro and in vivo. Nat Biotechnol. 2015 Jan;33(1):73–80.

303. Pramanik S, Steinkühler J, Dimova R, Spatz J, Lipowsky R. Binding of His-tagged fluorophores to lipid bilayers of giant vesicles. Soft Matter. 2022;18(34):6372–83.

304. Crocker PR, Paulson JC, Varki A. Siglecs and their roles in the immune system. Nat Rev Immunol. 2007 Apr;7(4):255–66.

305. Wißfeld J, Nozaki I, Mathews M, Raschka T, Ebeling C, Hornung V, Brüstle O, Neumann H. Deletion of Alzheimer's disease-associated CD33 results in an inflammatory human microglia phenotype. Glia. 2021 Jun;69(6):1393–412.

306. Huang H, Fletcher A, Niu Y, Wang TTY, Yu L. Characterization of lipopolysaccharide-stimulated cytokine expression in macrophages and monocytes. Inflamm Res. 2012 Dec;61(12):1329–38.

307. Fellermann M. Characterization of clostridial C3 toxin and diphtheria toxin mutant proteins, their cellular internalization and application as delivery tools for foreign cargo molecules (Dissertation of M. Fellermann, submitted 2021). 2022.

308. Mamat U, Wilke K, Bramhill D, Schromm AB, Lindner B, Kohl TA, Corchero JL, Villaverde A, Schaffer L, Head SR, Souvignier C, Meredith TC, Woodard RW. Detoxifying Escherichia coli for endotoxin-free production of recombinant proteins. Microb Cell Fact. 2015 Dec;14(1):57.

309. Baranov MV, Kumar M, Sacanna S, Thutupalli S, Van Den Bogaart G. Modulation of Immune Responses by Particle Size and Shape. Front Immunol. 2021 Feb 12;11:607945.

310. Manzano I, Taylor N, Csordas M, Vezeau GE, Salis HM, Zydney AL. Purification of Cas9— RNA complexes by ultrafiltration. Biotechnology Progress. 2021 Mar;37(2):e3104.

311. Chen K, Han H, Zhao S, Xu B, Yin B, Lawanprasert A, Trinidad M, Burgstone BW, Murthy N, Doudna JA. Lung and liver editing by lipid nanoparticle delivery of a stable CRISPR–Cas9 ribonucleoprotein. Nat Biotechnol. 2025 Sep;43(9):1445–57.

312. Karp H, Zoltek M, Wasko K, Vazquez AL, Brim J, Ngo W, Schepartz A, Doudna JA. Packaged delivery of CRISPR–Cas9 ribonucleoproteins accelerates genome editing. Nucleic Acids Research. 2025 Feb 27;53(5):gkaf105.

313. Frangoul H, Altshuler D, Cappellini MD, Chen YS, Domm J, Eustace BK, Foell J, De La Fuente J, Grupp S, Handgretinger R, Ho TW, Kattamis A, Kernytsky A, Lekstrom-Himes J, Li AM, Locatelli F, Mapara MY, De Montalembert M, Rondelli D, Sharma A, Sheth S, Soni S, Steinberg MH, Wall D, Yen A, Corbacioglu S. CRISPR-Cas9 Gene Editing for Sickle Cell Disease and β-Thalassemia. N Engl J Med. 2021 Jan 21;384(3):252–60.

314. Liu BY, He XY, Zhuo RX, Cheng SX. Tumor targeted genome editing mediated by a multi-functional gene vector for regulating cell behaviors. Journal of Controlled Release. 2018 Dec;291:90–8.

315. Lou H, Feng M, Hageman MJ. Advanced Formulations/Drug Delivery Systems for Subcutaneous Delivery of Protein-Based Biotherapeutics. Journal of Pharmaceutical Sciences. 2022 Nov;111(11):2968–82.

316. Dilioglou S, Cruse JM, Lewis RE. Function of CD80 and CD86 on monocyte- and stem cell-derived dendritic cells. Experimental and Molecular Pathology. 2003 Dec;75(3):217–27.

317. Orekhov AN, Orekhova VA, Nikiforov NG, Myasoedova VA, Grechko AV, Romanenko EB, Zhang D, Chistiakov DA. Monocyte differentiation and macrophage polarization. VP [Internet]. 2019 Mar 21 [cited 2026 Jan 18];2019. Available from: https://www.oaepublish.com/articles/2574-1209.2019.04

318. Chen X, Zaro JL, Shen WC. Fusion protein linkers: Property, design and functionality. Advanced Drug Delivery Reviews. 2013 Oct;65(10):1357–69.

319. Ishidoh K, Kominami E. Processing and Activation of Lysosomal Proteinases. Biological Chemistry. 2002 Dec 9;383(12):1827–31.

320. Tsuchikama K, An Z. Antibody-drug conjugates: recent advances in conjugation and linker chemistries. Protein Cell. 2018 Jan;9(1):33–46.

321. Zhang Z, Rong X, Xie T, Li Z, Song H, Zhen S, Wang H, Wu J, Jaffrey SR, Li X. Fluorogenic CRISPR for genomic DNA imaging. Nat Commun. 2024 Jan 31;15(1):934.

322. Ran FA, Hsu PD, Lin CY, Gootenberg JS, Konermann S, Trevino AE, Scott DA, Inoue A, Matoba S, Zhang Y, Zhang F. Double Nicking by RNA-Guided CRISPR Cas9 for Enhanced Genome Editing Specificity. Cell. 2013 Sep;154(6):1380–9.

7 Appendix

7.1 Sequence of $C3_{E174Q}$_$Cas9^{NLS\text{-}His}$

AYSNTYQEFTNIDQAKAWGNAQYKKYGLSKSEKEAIVSYTKSASEINGKLRQNKGVINGFPSNLIKQVELLDKSFNKMKTPENIMLFRGDDPAYL
GTEFQNTLLNSNGTINKTAFEKAKAKFLNKDRLEYGYISTSLMNVSQFAGRPIITKFKVAKGSKAGYIDPISAFAGQLQMLLPRHSTYHIDDMRLS
SDGKQIIITATMMGTAINPKGSGSGMDKKYSIGLDIGTNSVGWAVITDEYKVPSKKFKVLGNTDRHSIKKNLIGALLFDSGETAEATRLKRTARRR
YTRRKNRICYLQEIFSNEMAKVDDSFFHRLEESFLVEEDKKHERHPIFGNIVDEVAYHEKYPTIYHLRKKLVDSTDKADLRLIYLALAHMIKFRGHFL
IEGDLNPDNSDVDKLFIQLVQTYNQLFEENPINASGVDAKAILSARLSKSRRLENLIAQLPGEKKNGLFGNLIALSLGLTPNFKSNFDLAEDAKLQL
SKDTYDDDLDNLLAQIGDQYADLFLAAKNLSDAILLSDILRVNTEITKAPLSASMIKRYDEHHQDLTLLKALVRQQLPEKYKEIFFDQSKNGYAGYI
DGGASQEEFYKFIKPILEKMDGTEELLVKLNREDLLRKQRTFDNGSIPHQIHLGELHAILRRQEDFYPFLKDNREKIEKILTFRIPYYVGPLARGNSR
FAWMTRKSEETITPWNFEEVVDKGASAQSFIERMTNFDKNLPNEKVLPKHSLLYEYFTVYNELTKVKYVTEGMRKPAFLSGEQKKAIVDLLFKTN
RKVTVKQLKEDYFKKIECFDSVEISGVEDRFNASLGTYHDLLKIIKDKDFLDNEENEDILEDIVLTLTLFEDREMIEERLKTYAHLFDDKVMKQLKRR
RYTGWGRLSRKLINGIRDKQSGKTILDFLKSDGFANRNFMQLIHDDSLTFKEDIQKAQVSGQGDSLHEHIANLAGSPAIKKGILQTVKVVDELVKV
MGRHKPENIVIEMARENQTTQKGQKNSRERMKRIEEGIKELGSQILKEHPVENTQLQNEKLYLYYLQNGRDMYVDQELDINRLSDYDVDHIVP
QSFLKDDSIDNKVLTRSDKNRGKSDNVPSEEVVKKMKNYWRQLLNAKLITQRKFDNLTKAERGGLSELDKAGFIKRQLVETRQITKHVAQILDSR
MNTKYDENDKLIREVKVITLKSKLVSDFRKDFQFYKVREINNYHHAHDAYLNAVVGTALIKKYPKLESEFVYGDYKVYDVRKMIAKSEQEIGKATA
KYFFYSNIMNFFKTEITLANGEIRKRPLIETNGETGEIVWDKGRDFATVRKVLSMPQVNIVKKTEVQTGGFSKESILPKRNSDKLIARKKDWDPKK
YGGFDSPTVAYSVLVVAKVEKGKSKKLKSVKELLGITIMERSSFEKNPIDFLEAKGYKEVKKDLIIKLPKYSLFELENGRKRMLASAGELQKGNELALP
SKYVNFLYLASHYEKLKGSPEDNEQKQLFVEQHKHYLDEIIEQISEFSKRVILADANLDKVLSAYNKHRDKPIREQAENIIHLFTLTNLGAPAAFKYFD
TTIDRKRYTSTKEVLDATLIHQSITGLYETRIDLSQLGGDGGSGPPKKKRKVGSGHHHHHH

$C3_{E174Q}$ Cas9 NLS 6xHis-tag linker sequences

Figure 23: Amino acid sequence of $C3_{E174Q}$_$Cas9^{NLS\text{-}His}$ in single letter code. $C3_{E174Q}$ is indicated in purple and Cas9 in blue. The nuclear localization sequence (NLS) is depicted in green and the hexahistidine tag (6xHis-tag) is dyed in orange. Linker sequences are indicated in grey.

7.2 Labelling of Proteins with DyLight^{488} NHS Ester

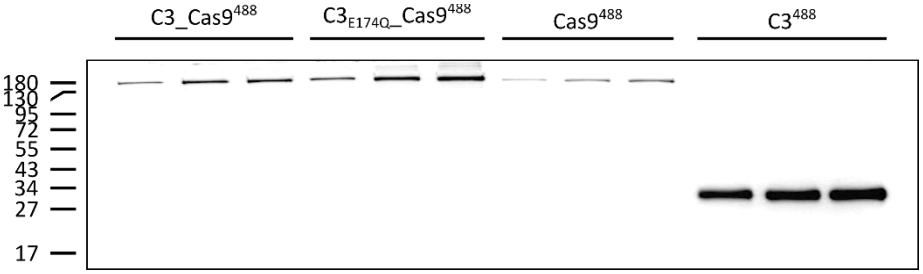


Figure 24: SDS-PAGE gel of DyLight^{488} labelled proteins detected at 480 nm. The gel was loaded with 240 ng to 470 ng of C3_Cas9^{488}, with 330 ng to 660 ng of $C3_{E174Q}$_Cas9^{488}, with 120 ng to 360 ng of Cas9^{488} or with 1180 ng to 3550 ng of C3^{488}.

7.3 Gene Fragments Amplified for Cleavage Assays

a) eGFP gene fragment

TGCTTCAGCCGCTACCCCGACCACATGAAGCAGCACGACTTCTTCAAGTCCGCCATGCCCGAAGGCTACGTCCAGGAGCGCACCATCTTCT
TCAAGGACGACGGCAACTACAAGACCCGCGCCGAGGTGAAGTTCGAGGGCGACACCCTGGTGAACCGCATCGAGCTGAAGGGCATCG
ACTTCAAGGAGGACGGCAACATCCTGGGGCACAAGCTGGAGTACAACTACAACAGCCACAACGTCTATATCATGGCCGACAAGCAGAAG
AACGGCATCAAGGTGAACTTCAAGATCCGCCACAACATCGAGGACGGCAGCGTGCAGCTCGCCGACCACTACCAGCAGAACACCCCCAT
CGGCGACGGCCCCGTGCTGCTGCCCGACAACCACTACCTGAGCACCCAGTCCGCCCTGAGCAAAGACCCCAACGAGAAGCGCGATCACA
TGGTCCTGCTGGAGTTCGTGACCGCCGCCGGGATCACTCTCGGCATGGACGAGCTGT

Binding site FP_eGFP | Binding site RP_eGFP | sgRNA^{eGFP} binding site | PAM

b) LSR gene fragment

ACAGGTGGCGTTCCTGTTGAAGCACCTCCCTGAGCTCACAGCAACCCTTGCTGTCTCTCCTCTTGCCCTCAGCTCCTGCCAGGGCCATCCAG
GTGACCGTGTCCAACCCCTACCACGTGGTGATCCTCTTCCAGCCTGTGACCCTGCCCTGTACCTACCAGATGACCTCGACCCCCACGCAACC
CATCGTCATCTGGAAGTACAAGTCTTTCTGCCGGGACCGCATCGCCGATGCCTTCTCCCCGGCCAGCGTCGACAACCAGCTCAATGCCCAGC
TGGCAGCCGGGAACCCAGGCTACAACCCCTACGTTGAGTGCCAGGACAGCGTGCGCACCGTCAGGGTCGTGGCCACCAAGCAGGGCAAC
GCTGTGACCCTGGGAGATTACTACCAGGGCCGGAGGATTACCATCACCGGAAGTATGTTGGGCAGGGCAGGGGGATGAGGCTGGGCTTG
CCCGGGTGGTGGGACTGGCGTCCTTGTGCGGGACCTGGAGTCCCCATCTGAAAGCTCTTGAGTGCCAGTGTCTGAAAGGACCATTGAAGG
GAGCAATTCTTTTTTTTTTTTTTTTTGAAGATGGAGTCTTGCTCTGGACTCCAGGCTGGAGTGCAGTGGTGCGATCTCAGCTCACTGCAACC
TCCACCTCCCAGGTTCAAGCAATTCTCTTGCCTCAGCCTCCCGAGTAGCTGGGACTCCAGGTGCGTGCCACCACGCCCAGTTAATTTTTGTA
TTTTTAGTAGAGATGGGGTTTCACCATGTTGGCCAGGCTGGTCTCAAACTCCTGACCTCAAATGATCTGCCCGCCTTGGCCTCGCAAAGTGC
TGAGAGACACCATACCCAGCCTAAAGGGAGCGATTCTATTCTACTATTCTTCCTTCTGCTAATCCTTCCATTCTTTAATTTAATAACGAAGATTT
TTTGAGTACCTGTCATATACCAGGTGCTGTTCTGGGCCCTGGGAATACAGCTGTTAACAAAATCATCAAACCACTTCCCTCGTGGAGCCCACA
TTGCAGTGAGAGAGACAAACACGACACACACTCTCAAGTCCTTGAAGATAAAGAAAACTGGGTAACGGAGAGAAGAGGCCAGGGTTTGT
TCTATAATCATTAATAACACGAGCAGTAAGAAGTAAAATTTATCTAAGTAACAACTTATAAAGGGTCTACTGTGTGCTAAGCTCTCATCCAGGT
TCCCAAGGATTAACTCAGACCACACAGTAATTGAATAGATTCTATCATTGTCATCTTACAGAGGCCCAGAGAGAGAAAGTGACTTGCCTAGT
GTCATAGCTGGTAACGGGGCTGGGATTCTAACTCAGCCACTTTGGGTCTAGTGGCCAAGCTCCTAATCCCTTTGCTTGCCTAGGGTGGTCC

Binding site FP_LSR | Binding site RP_LSR | sgRNA^{LSR} binding site | PAM

c) CD33 gene fragment

GGATGGGCAAGGGGGAAGTTGCTAGTCATCCCCAAATATCCTTTTCCAAGGTGCCTGATGTCTACCCGTGTCTAACTGCAGGCCTTGCCTCT
GAACATTTGACTCTGAAAGTCCAGATCTGACCAAACCTGACACAGACTCAATGTCAGTAACAGCCCCAGGCGGGGAGGCTCCTTCCTACCT
GAGCCATCTCCTGGAAAGATACCAGTTGTTGGGTTCTGTGGAACATCTAGGAGAGGAAGAGAGGATTTCCTTCAGTTGGGGGTAGAGATG
AGATAAGGGTAGGCATTTCCCCTTACTCCTGCCAGAAACCACAGAAATGCAGAAGGGACAGGGCTCATGTCCTTCTGGCTCCCGAACTCAG
CCAGGCCTCCAGGACACTAAATGTCCCCAGCACCAGCCCATCCTGTCTCCCCTACACCCTCAGGGACCCCAGCATCCTGGCCCAGCACTTAC
AGGTGACGTTGAGCTGGATGGTTCTCTCCGTAGTCACACCAGCTCCAGCGAACTTCACCTGACAGGTCAGGTTGGTGCCGTGGTCCTGGGG
CCGTGGGGTGATTATGAGCACCGAGGAGTGAGTAGTCCTGGGGCCCAGGGAGGTGGGGGCAGCTGACAACCAGGAGAAGATCGGGGGT
GTTCCCTGCTCACAGGCCCAGGACACAGAGCAGGTCAGGTTTTTGGAGTGGCCGGGTTCTAGAGTGCCAGGGATGAGGATTTTGGGCCTG
TGGGTCAAGTCTAGTGAGGAGAAAGAGGGGATGCAGAATCAGGAGGGAGGGTCCAGGTGAGGGCCTGAGAGAAGATCAACCTCTGGTC
AAGCTCCCCCGCTAAGCACGACAGGCTTTACCCCTAAACCCCTCCCAGTACCAGGGTCCCATCCCAGCCCTGCCCTGCAGTACCCATGAACT

Binding site FP_CD33 | Binding site RP_CD33 | sgRNA^{CD33} binding site | PAM

Figure 25: Gene fragments used in this thesis of the eGFP gene (a), the LSR gene (b) and the CD33 gene (c) amplified by PCR for in vitro cleavage assays. The respective binding sites for each forward primer (FP) are indicated in blue, the binding site for each reverse primer (RP) in green. The binding site of the sgRNA protospacer is marked in purple, respectively. The protospacer adjacent motif (PAM) is indicated in orange.

7.4 Endotoxin Measurement in C3_Cas9 and $C3_{E174Q}$_Cas9

Table 19: Raw data of the endotoxin measurements in C3_Cas9 and $C3_{E174Q}$_Cas9 samples using the ENDONEXT™ EndoLISA® kit (bioMérieux, Marcy-l'Étoile, FRA). The assay was performed as indicated by the manufacturer using the following parameters: excitation wavelength 380 nm, emission wavelength 440 nm, 46 flashes with 400 Hz, measuring times 0 min and 90 min, temperature 37.5 °C. The displayed fluorescence intensity (FI) values are measured after 90 minutes and corrected by initial values at 0 minutes. Lipopolysaccharid (LPS) standards were measured as duplicates, the amount of LPS in the samples C3_Cas9 and $C3_{E174Q}$_Cas9 was detected as singlets in a 1:10 dilution. LPS concentration (conc.) in the samples was calculated by generating a standard curve from the LSP standard.

LPS conc. standard [EU/ml]	FI standard n=1	FI standard n=2	Sample name	FI sample n=1 (1:10)	LPS conc. sample [EU/ml]
500	40109	41049	C3_Cas9	15929	1878
50	20495	23583	$C3_{E174Q}$_Cas9	8079	679
5	4507	3754			
0.5	827	534			
0.05	156	74			

8 Acknowledgements

Acknowledgements were removed for data privacy protection reasons.

9 Statutory Declaration

I hereby declare that I wrote the present dissertation with the topic:

"***Clostridium botulinum* C3 Toxin as Inhibitor of Breast Cancer-Induced Osteolysis and Cell Type-Selective Transporter for Targeted Gene Editing in Monocytic Cells**"

independently and used no other aids than those cited. In each individual case, I have clearly identified the source of the passages that are taken word for word or paraphrased from other works.

I also hereby declare that I have carried out my scientific work according to the principles of good scientific practice in accordance with the current „Satzung der Universität Ulm zur Sicherung guter wissenschaftlicher Praxis" [Rules of the University of Ulm for Assuring Good Scientific Practice].

Ulm, 19.05.2026

Nicole Stadler